Liquid Filled Waveguides and Fibres

Zipei Song

St Annes College
University of Oxford

A thesis submitted for the degree of
Doctor of Philosophy

Hilary 2024

Abstract

Ever since the initial development of fibre Bragg gratings (FBGs) in 1977, their inherent sensitivity to both temperature and strain has become a significant challenge. This thesis seeks to address this enduring issue by developing novel FBG devices that would potentially solve this 47-year-old problem.

Through the exploration of a novel approach using liquid-filled waveguides and fibres, detailed insights into its implementation across design, fabrication, and experimental demonstration are provided. A thorough examination and comparison of various analysis and simulation techniques are undertaken to provide detailed guidelines for device designs. A distinctive technique of aberration correction was introduced to focus the laser beam into the optical fibres during fabrication. This enables the fabrication of micro-engineered FBG devices with fluid-filled microchannels within the evanescent fields. These devices provide extraordinary thermal sensitivities and the significant achievements in these devices effectively meet the requirements of various optical devices and optical fibre sensing applications. This research contributes to the field by offering a comprehensive solution to a longstanding problem in FBG sensor technology. Through a series of experiments and simulations, the feasibility and effectiveness of this approach are demonstrated. Furthermore, the thesis explores methods for reinforcing FBG devices for strain sensing, including recoating with polymers and custom fibre designs. These methods enhance the mechanical strength of FBG devices, improving their durability and reliability in sensing applications.

Overall, this thesis presents a significant advancement in FBG sensor technology, offering a comprehensive solution to the longstanding challenge of strain and temperature discrimination. The research conducted contributes to the understanding of FBG sensor technology and provides practical solutions that have the potential to impact a wide range of optical sensing applications.

Liquid Filled Waveguides and Fibres

Zipei Song
St Annes College
Department of Engineering Science
University of Oxford

A thesis submitted for the degree of
Doctor of Philosophy
Hilary 2024

Acknowledgements

I would like to express my sincere gratitude to my supervisors for their invaluable guidance, mentorship, and unwavering support throughout this research project. I would like to thank Dr. Julian Fells for the solid foundation he established for me and the continuous support during my entire project. As he said D.Phil is never a smooth path since there are always hills and valleys. Now I believe I am fully prepared to continue our journey. I would like to thank Prof.Stephen Morris for his patience and professionalism. My sincere thanks also goes to Prof. Steve Elston for all the invaluable advice and so many insightful conversations. I would also like to thank Martin, for his perceptive insights and meticulous organization. Because of them, I am genuinely proud to be a member of the SMP group and the DOP. Their expertise, encouragement, and constructive feedback have been instrumental in shaping the direction and quality of this thesis.

I am also deeply thankful to Prof.Steve Collins and Prof.Dominic O'Brien for their valuable input and constructive criticism during my transfer and confirmation of status.

I am thankfully acknowledge the support and inspiration to Dr.Mohan Wang who has been extremely supportive during my entire D.Phil study. I would also like to express my appreciation to Dr.Patrick Salter for his kindly sharing of the experimental resources. I extend my gratitude to the fibre team, particularly Dr. Frank Payne, for sharing invaluable knowledge, and to Tongyu and Eleanor for their diligent efforts and insightful contributions.

I would like to acknowledge the assistance and support from the SMP group. I would like to thank Yihan for invaluable support as the clean room champion. Your academic prowess is only one aspect of your remarkable character. You are undoubtedly the most esteemed member among the group's students! Thank you Bohan for all the random but interesting conversations during the commuting time and for all the support in daily life. You are the best neighbour ever!

Many thanks to Bangshan, Andong, Peng, Jingyu, Jiahe, Guanxiong, Mengmeng, Linpei, Zhikai, Jingyu, Waqas, Adi and all the lovely colleagues I have been working with. Apologies if I'm unable to express my appreciation to each of you individually. It's truly fortunate for me to have met everyone.

I want to express my heartfelt gratitude to my parents, who have been the primary supporters of my D.Phil research. We have been living in three different time zones over these years, finding time to join together has not been easy. I understand it has been a challenging time for all of us. I am also fully aware that during my peaceful moments, someone must be shouldering the burden for me. I hope that it is the moment now I am able to make you proud. Thank you so much!

Much appreciation to my cherished young companions Nana, Tuotuo, Qiuqiu, and Mosaic, as well as their fantastic caregivers. Their unwavering support has been invaluable to me since my undergraduate years. Their presence and encouragement have made a significant impact on my journey, providing me with strength and motivation during challenging times.

I would like to express my gratitude to my special little friend Mew, a cream colored British short hair cat. Mew has been staying with me throughout the pandemic period. It has been a year since he has been away and I hope him all the best at the cats' planet.

And finally, thank you Yueru. Your unwavering support and love have been the bedrock of my journey throughout this doctoral pursuit. I am forever grateful for your presence in my life and I dedicate this achievement to our shared dreams and future together.

Abstract

Ever since the initial development of fibre Bragg gratings (FBGs) in 1977, their inherent sensitivity to both temperature and strain has become a significant challenge. This thesis seeks to address this enduring issue by developing novel FBG devices that would potentially solve this 47-year-old problem.

Through the exploration of a novel approach using liquid-filled waveguides and fibres, detailed insights into its implementation across design, fabrication, and experimental demonstration are provided. A thorough examination and comparison of various analysis and simulation techniques are undertaken to provide detailed guidelines for device designs. A distinctive technique of aberration correction was introduced to focus the laser beam into the optical fibres during fabrication. This enables the fabrication of micro-engineered FBG devices with fluid-filled microchannels within the evanescent fields. These devices provide extraordinary thermal sensitivities and the significant achievements in these devices effectively meet the requirements of various optical devices and optical fibre sensing applications. This research contributes to the field by offering a comprehensive solution to a longstanding problem in FBG sensor technology. Through a series of experiments and simulations, the feasibility and effectiveness of this approach are demonstrated. Furthermore, the thesis explores methods for reinforcing FBG devices for strain sensing, including recoating with polymers and custom fibre designs. These methods enhance the mechanical strength of FBG devices, improving their durability and reliability in sensing applications.

Overall, this thesis presents a significant advancement in FBG sensor technology, offering a comprehensive solution to the longstanding challenge of strain and temperature discrimination. The research conducted contributes to the understanding of FBG sensor technology and provides practical solutions that have the potential to impact a wide range of optical sensing applications.

Contents

List of Figures

List of Publications

1. **Song, Z.**, Wang, M., Payne, F., Salter, P., Liu, T., Elston, S., Booth, M., Morris, S. and Fells, J., 2024. Fiber Bragg gratings with micro-engineered temperature coefficients. Advanced Optical Materials.

2. **Song, Z.**, Wang, M., Salter, P.S., Liu, T., Elston, S.J., Booth, M.J., Morris, S.M. and Fells, J.A., 2023, November. Fiber Bragg grating sensors with ultrahigh or ultralow temperature sensitivity. In Optical Fiber Sensors (pp. W2-2). Optica Publishing Group.

3. **Song, Z.**, Salter, P. S., Charman A., Liu, T., Wang, M., Morris, S.M. Booth, M.J. and Fells, J.A. (in Preparation). Aberration-corrected femtosecond laser direct writing for arbitrary 3D structuring inside optical fibers.

4. Payne, F., **Song, Z.**, Wang, M. and Fells, J.A., 2025. An exact analysis of the temperature control of optical waveguides. Optical and Quantum Electronics, 57(3), p.188.

5. Liu, T., **Song, Z.**, Reeves, R., Wang, M., Doyle, C.T., Booth, M.J. and Fells, J.A., 2024. 3D Structured Optical Fiber Pressure Sensors. Journal of Lightwave Technology.

6. Liu, T., **Song, Z.**, Wang, M., Doyle, C.T., Booth, M.J. and Fells, J.A., 2023, November. 3D Structured Optical Fiber Pressure Sensors Based on Femtosecond Laser Fabrication. In Optical Fiber Sensors (pp. W4-61). Optica Publishing Group.

7. Wang, M., Salter, P.S., Payne, F.P., Liu, T., Shipley, A., **Song, Z.**, Morris, S.M., Booth, M.J. and Fells, J.A., 2024. Optimization of Single-mode Sapphire Waveguide Bragg Gratings. Journal of Lightwave Technology.

1

Introduction

Contents

This thesis begins with a brief introduction including the motivations of the project and the thesis outline.

1.1 Motivations

Optical fibre sensors are highly effective tools for monitoring a wide range of physical, chemical, and environmental parameters. These sensors offer several advantages over traditional sensing technologies, making them ideal for use in challenging environments [1]. Their small size allows easy integration into various systems, such as structural health monitoring in bridges [2], temperature detection in biological tissues [3], and pressure monitoring in aircraft wings [4], without adding significant bulk. With relative high melting point and thermal stability, they are inherently safe for use in explosive or flammable environments, such as in the oil and gas industry [5]. In addition, optical fibre sensors are immune to electromagnetic interference, ensuring accurate and reliable data transmission even in electrically noisy settings. Their resistance to corrosion further enhances their durability, making them suitable for long-term deployment in harsh conditions, including marine or chemical processing environments [6].

Optical fibre sensors encompass a wide range of types, each tailored to specific applications and measurement techniques. Fabry–Perot sensors, which utilize interference between two reflecting surfaces to measure parameters like pressure and temperature, are frequently used in aerospace and medical devices due to their high sensitivity [7]. Interferometric fibre sensors leverage the interference of light waves to detect minute changes in environmental conditions, making them ideal for precision measurements in industrial and structural monitoring [8]. Raman scattering-based sensors are used for distributed temperature sensing over long distances, commonly applied in fire detection and environmental monitoring [9]. Brillouin scattering-based sensors, which detect strain and temperature changes along the fibre, are valuable for structural health monitoring in large infrastructures such as bridges and pipelines [10]. Optical time-domain reflectometry (OTDR) is a powerful technique to locate faults and measure attenuation in long fibre networks, widely used in telecommunications and network maintenance [11]. Polarimetric sensors, which measure changes in the polarization state of light, are used to monitor electric currents and magnetic fields [12]. Evanescent wave sensors, which detect changes in the light wave propagating along the fibre surface, are utilized in chemical and biological sensing, particularly for detecting contaminants or pathogens [13].Optical frequency domain reflectometry (OFDR) offers high-resolution distributed sensing, used in applications like strain mapping in composite materials [14].

Finally, Fibre Bragg Grating (FBG) sensors, which reflect specific wavelengths of light depending on strain or temperature changes, are highly versatile and used across various fields, including civil engineering, aerospace, and energy [15]. While distributed sensors, such as Raman and Brillouin-based sensors, are designed to monitor changes continuously along the entire fibre length, making them suitable for large-scale structures, point sensors like FBGs and Fabry–Perot sensors focus on specific locations, providing precise measurements in targeted areas. Among them, FBGs are often preferred because they offer high sensitivity, multiplexing capability, and ease of integration into various structures, allowing multiple sensing points along a single fibre, making them particularly suitable for distributed sensing applications in complex environments [16]. Specifically, in real world FBGs are used in structural health monitoring of bridges, dams and buildings [17], in nuclear reactors [18], in hydraulic systems [19], in wind turbine blades [20], inside the human body during surgery [21], and in automotive structures [22].

Fibre Bragg gratings(FBGs) are periodic structures written in optical fibres that allow wavelength-specific reflection of light. By measuring the reflection peak, FBGs can be used as highly sensitive and accurate sensors for many physical properties such as temperature, strain, pressure, humidity, refractive indices and many other physical properties in remote and extreme environments [1]. As well as sensing, FBGs are used for many other applications. For example, FBGs serve as highly effective optical filters due to their ability to reflect specific wavelengths while transmitting others, making them ideal for wavelength division multiplexing (WDM) systems [23]. This selective filtering capability is crucial for managing and routing different data channels within optical networks. Furthermore, FBGs are employed in pulse compression techniques [24], where they help to shorten the duration of optical pulses, enhancing the resolution in OTDR and improving performance in ultrafast optical systems. Their precise control over light propagation also makes FBGs valuable in laser stabilization and the development of narrow-linewidth lasers, where they help maintain consistent output by filtering out unwanted wavelengths [25].

Despite these considerable advantages, there has been a problem that has existed for more than 40 years ever since the discovery of FBGs [26], which is their intrinsic temperature dependence when measuring other parameters. For example, the strain response due to an applied strain on FBGs arises from both the change in grating period from physical extension and the refractive indices due to photoelastic effects, while the temperature response is also determined by both the thermal expansion of the grating period and refractive index variation because of thermo-optic effects[16]. This explains the problem as with a single measurement of the

Bragg wavelength, one is not able to tell whether there has been a temperature variation or an applied strain on the FBGs.

Discrimination between temperature and strain has attracted attention for more than four decades. The temperature dependence could be compensated by adding athermal packages [27] but the additional mechanical components will prevent the use of FBGs as sensors. Approaches such as using two wavelengths to give two measurements with differing sensitivities to temperature could be employed [28]. Others take advantages of FBG properties with different polarisation modes in specific fibre devices such as high birefringence “quasi-rectangle” fibres [29], fibre devices with composite laminate [30], or with a micro-structured fibres [31]. However, all these wavelength or polarisation dependent methods only give small changes in sensitivity.

A number of indirect approaches are known to combine an FBG with different types of optical fibre sensors to provide on extra measurement for the two physical properties. Devices with multi-mode fibres acts as a Mach–Zehnder interferometer (MZI) [32]. Devices utilizing the four-wave mixing effect allow the temperature of one FBG to be compensated by the other FBG [33]. A Fabry-Pérot cavity could also provide a temperature and stain dependent measurement just as an MZI [34]. Long period gratings have different sensitivities and could be fabricated with exactly the same technique as FBGs [35]. A few-mode fibre considering different effective index and sensitivities of different propagration modes [36]. In a no-core fibre (NCF), Multimode inter- ference (MMI) will occur along the NCF due to the different longitudinal propagation constants [37]. The the amplified spontaneous emission (ASE) power of erbium-doped fibre is dependent on temperature thus could be used as a strain independent indicator[38]. Rocking filter interferometer could be produced by manipulating the pitch of FBGs and intrinsicly has different temperature and strain dependence[39]. There are many more approaches to provide another measurement not listed here.

There are also approaches that rely on intensity-based measurements including analysis of side lobe power [40] and overall spectral analysis by machine learning

[41]. However, those measurements are vulnerable to noise and bending losses. Alternative approaches include modification of the thermal or strain response of FBG sensors, which can then be compared with a conventional FBG sensor. Such modifications include strain compensation with a glass tube [20], and altering the strain response with fibres of different diameters so that the strain response is different due to the same stress applied [42] [43]. Fibre Bragg gratings have been written in tapered optical fibre to give a strain-induced bandwidth change [44], but tapering the fibre compromises its mechanical strength. However, the additional materials can make the fibre incompatible for embedding within the infrastructure to be instrumented. Alternatively, previous research has shown that the thermal sensitivity is enhanced to 50.8 pm/°C by coating the FBG with higher thermal expansion materials [45]. But since the expansion of the coating causes a strain on the grating, the devices could not be used to measure a strain of something else.

There have been a number of reports of microstructured fibre with an array of holes in the cross-section that have been filled with liquid. Liquid, compared with fused silica that standard fibres are made of, presents a significant and negative thermo-optic coefficient dn/dT. For example, Naeem *et al.* were able to achieve a modest change in temperature sensitivity using methanol-filled holes [46]. Alternatively, Huy *et al.* showed plots with flattened temperature response over a limited temperature range but did not show spectra for the filled fibres [47]. It is likely that such a configuration would be multi-moded and there is no information on loss. Very recently a fibre with a filled 2 μm hollow core showed high temperature sensitivity, but with very high loss and poor spectra[48]. There have been theoretical papers proposing filled microstructured fibres for low temperature sensitivity [49][50] and high temperature sensitivity[51], but these designs were not realized experimentally.

The cross-sensitivity between strain and temperature is a longstanding issue that significantly impacts many applications. This problem often acts as a limiting factor, and addressing it could provide substantial benefits. Current solutions have not been highly effective, and this work aims to develop a practical and robust method to resolve the issue.

1.2 Thesis outline

Chapter 2 will be background and theories of optical waveguides, optical fibres, optical FBGs, FBG fabrication methods and FBG applications, especially FBG sensors.

In Chapter 3 there will be discussion on different simulation techniques about optical waveguides. Firstly, there will be introduction on the well-known analytical waveguide theories and the analytical FBG coupled wave theories. There will also be introduction on some useful numerical simulation methods for waveguide solving including Film mode matching (FMM) method, Finite-difference mode (FDM) method and Finite element mode (FEM) method. And finally there will be comparison of some test structures to find the convergence between the numerical and analytical methods.

Chapter 4 introduces the actual design of the liquid-filled FBG temperature devices employing the theories and simulation techniques discussed in the above chapters. Different liquids to be filled are compared and a conclusion is drawn. There will be discussion on figures of merit according to what the potential costumers need. The chapter will also include several analytical and numerical simulation methods to compare the performance of the designs and give a set of optimised solutions.

Then in Chapter 5 and Chapter 6 there will be illustration on how such liquid-filled devices were fabricated. The two main composition of the device, the FBG and the microchannels will both be fabricated by the direct laser writing (DLW) system. Also the ability of laser alignment of liquid crystals is also demonstrated by fabrication of micro-cells, which might be an interesting foundation for future development. Additionally, there will be introduction on other essential techniques for fabrication including fibre splicing, fibre cleaving and fibre re-coating.

In Chapter 7 the experimental apparatus and results are presented. The apparatus includes waveguide testing rig, the reflectivity and transmission measurement, the temperature control system and the strain measurement rig. Then there will be results on the high thermal sensitivity devices and low thermal sensitivity devices, where both glycerol filled and refractive index liquid filled devices will be presented. The discussion section will follow.

In Chapter 8 a further development of such devices will be reinforcement for strain sensing purposes. There will be discussions on improvement of the robustness for strain sensing in several aspects, which are cross-sectional design optimisation, custom fibre instead of microchannel fabrication, polymerisable liquid, and poly-acrylate for coating.

Eventually in Chapter 9 there will be a brief conclusion and future work including further development on device reinforcement, liquid crystal devices development and compensation for coated materials.

2
Background

Contents

2.1 Introduction

In this background chapter, there will be a brief introduction, followed by an introduction to the theoretical aspects of optical waveguides, optical fibres, and Bragg gratings. In each case, a review of the literature will be provided.

2.2 Optical waveguides explained by total internal reflection

A waveguide is defined as a structure that guides electromagnetic waves such as visible light, where energy can be transferred from one end of the waveguide to the other. Optical waveguides represent a crucial component in the realm of modern photonics, playing a pivotal role in guiding and manipulating light for various applications. These sophisticated structures serve as pathways for optical signals, confining and directing light waves with precision. By exploiting the principles of total internal reflection, optical waveguides enable the efficient transmission of optical signals over considerable distances, fostering advancements in telecommunications, sensors, imaging systems, and beyond.

The condition for total internal reflection (TIR) can be derived from Snell's law. Considering a boundary between two different media with different refractive indices, the relationship between the incident angle θ_1, refraction angle θ_2 and refractive indices n_1 and n_2 is given by [52]:

$$n_1 \mathrm{sin}\theta_1 = n_2 \mathrm{sin}\theta_2 \tag{2.1}$$

When $n_1 > n_2$, there exists a set of incident angles $\theta_1 > \theta_C$ at which no light is refracted. The angle θ_C is called the critical angle given by:

$$\theta_C = \mathrm{arcsin}(n_2/n_1) \tag{2.2}$$

$\theta_1 > \theta_C$ is called the TIR condition. When light is incident on a boundary between two media, both refraction and reflection occur while the refracted rays escape from the waveguide and the reflected ones bounce between the boundaries and propagate within the media. A planar waveguide is formed when a sheet of higher index core is placed in between lower index cladding and the TIR condition is met on both interfaces.

A significant feature of a waveguide under TIR condition is the evanescent field, which indicates that the guided wave penetrates the cladding. The penetration depth d_p is given by [53]:

$$d_p = \frac{\lambda}{2\pi\sqrt{n_1^2 \mathrm{sin}^2\theta_1 - n_1^2}} \tag{2.3}$$

Under TIR, the penetration depth is approximately 5 times the wavelength of the light λ. Furthermore, the equation also indicates that modifications to the cladding could affect the TIR condition of the waveguide. The concept of evanescent field penetration establishes the foundation of putting micro-channels in the cladding.

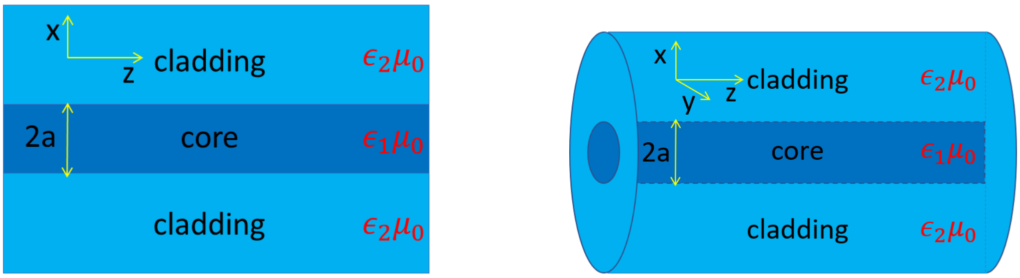

(a) Slab Waveguide **(b)** Cylindrical Waveguide

Figure 2.1: Sketch of planar and cylindrical Waveguides. Incident light is propagating along the z-axis and bouncing between the core-cladding interfaces.

Step-index planar waveguide

In this subsection the ray approach is used to provide basic understanding of a planar waveguide and a circular waveguide. A planar waveguide is a 2-D rectangular waveguide that does not exist in reality. As shown in Fig. 2.1a, a step-index planar waveguide is composed of a higher refractive index core of thickness $2a$ in between lower index cladding. Incident light propagates along the z-axis which is placed in the centre of the core. The refractive index has the profile:

$$n(x) = \begin{cases} n_1, & -a < x < a \\ n_2, & |x| > a \end{cases} \tag{2.4}$$

where n_1 and n_2 are the refractive indices for the core and cladding, respectively. For light with freespace wavelength, λ, a nomalised frequency, V, that indicates the number of modes is defined:

$$V = \frac{2\pi a}{\lambda}\sqrt{n_1^2 - n_2^2} = \frac{2\pi a}{\lambda} NA \tag{2.5}$$

where NA is the numerical aperture given by $NA = \sqrt{n_1^2 - n_2^2}$.

In a 2-D planar waveguide only two circumstances occur for incident light, the rays are either bound between the interfaces or refracted and escape from the waveguide. The condition for each circumstance to happen is determined by the relationship between the incident angle and the critical angle defined in Eq. (2.2):

$$\begin{cases} \text{Bound rays} & \theta_c \leq \theta_1 \leq \frac{\pi}{2} \\ \text{Refracting rays} & 0 \leq \theta_1 < \theta_c \end{cases} \tag{2.6}$$

In order to characterise the rays, an invariant $\bar{\beta}$ is introduced and defined from Eq. (2.1):

$$\bar{\beta} = n_1 \text{sin}\theta_1 = n_2 \text{sin}\theta_2 \tag{2.7}$$

Noting that rays bounce between the interfaces periodically, $\bar{\beta}$ must be a constant at any position. By substituting Eq. (2.7) into Eq. (2.6):

$$\begin{cases} \text{Bound rays} & n_2 < \bar{\beta} < n_1 \\ \text{Refracting rays} & 0 \leq \bar{\beta} < n_2 \end{cases} \tag{2.8}$$

The propagation of rays is now fully characterized once $\bar{\beta}$ is defined. Because the reflection of rays is periodic, it is useful to characterise parameters within one period. The path length L_p, defined by the distance light travels between the successive reflections can be determined geometrically.

$$L_p = \frac{2a}{\text{cos}\theta_1} = \frac{2an_1}{\sqrt{n_1^2 - \bar{\beta}^2}} \tag{2.9}$$

The optical path length L_o is therefore given by the product of the path length and refractive index:

$$L_o = n_1 L_p = \frac{2an_1^2}{\sqrt{n_1^2 - \bar{\beta}^2}} \tag{2.10}$$

It is also useful to define the ray half-period z_p as the component of L_p in the direction of the z-axis:

$$z_p = L_p \text{cos}\theta_1 = \frac{2a\bar{\beta}}{\sqrt{n_1^2 - \bar{\beta}^2}} \tag{2.11}$$

The group velocity v_g of light inside the waveguide is given by:

$$v_g = \frac{c}{n_1} \tag{2.12}$$

where c is the speed of light. Therefore, one can work out the transit time as:

$$t = \frac{z}{z_p}\frac{L_p}{v_g} = \frac{z}{c}\frac{n_1}{\text{cos}\theta_1} \tag{2.13}$$

Step-index cylindrical waveguide

For a cylindrical waveguide such as an optical fibre, the parameters in Fig. 2.1b can still be combined with the normalised frequency V with exactly the same equation as Eq. (2.5) that was used to describe planar waveguides. However, in fibre waveguides instead of only meridional rays that always cross the axis, there exist skew rays that never cross the fibre axis. In order to indicate the skewness of the rays of incidence, θ_ϕ is introduced as the angle between the normal of the interface and the projection of the rays onto the cross-section. For meridional rays $\theta_\phi = 0$.

For a skewed ray incident and reflected by the interfaces, the angles of incidence α can be described by the above two-direction angles by:

$$\mathrm{cos}\alpha = \mathrm{cos}\theta_1 \mathrm{cos}\theta_\phi \tag{2.14}$$

In a planar waveguide the TIR condition for a ray to be bound is independent of θ_ϕ given by $\theta_c \leq \theta_1 \leq \frac{\pi}{2}$ in Eq. (2.6). In a cylindrical waveguide one could assume α_c as a critical angle of TIR given by:

$$\alpha_C = \mathrm{arcsin}(n_2/n_1) \tag{2.15}$$

However, the condition was derived for a planar interface. For a fibre, the curved surface causes leakage although the TIR condition is met.

Another class of rays referred to as tunneling rays [54] exist and the condition for the three classes are given by:

$$\begin{cases} \text{Bound rays} & \theta_c \leq \theta_1 \leq \frac{\pi}{2} \\ \text{Refracting rays} & 0 \leq \alpha < \alpha_c \\ \text{Tunneling rays} & 0 \leq \theta_1 < \theta_c \text{ and } \alpha_c \leq \alpha_1 \leq \frac{\pi}{2} \end{cases} \tag{2.16}$$

Both refracting rays and tunnelling rays cause energy loss thus are considered to be leaky. Again, the identical $\bar{\beta}$ invariant as in a planar waveguide is introduced. However, another invariant to characterise the skewness angle θ_ϕ is required. Again θ_ϕ is unchanged at any position. The second invariant $\bar{l}$ is defined as:

$$\bar{l} = n_1 \mathrm{sin}\theta_1 \mathrm{cos}\theta_\phi \tag{2.17}$$

where $\bar{l} = 0$ indicates meridional rays and $\bar{l} > 0$ indicates skew rays. So that

$$\bar{\beta}^2 + \bar{l}^2 = n_1^2 \mathrm{sin}\alpha \tag{2.18}$$

Whether or not the waveguide is leaky only depends on $\bar{\beta}$ while $\bar{l}$ determines the subdivision of tunnelling and refracting rays. The conditions are then given by:

$$\begin{cases} \text{Bound rays} & n_2 < \bar{\beta} < n_1 \\ \text{Refracting rays} & 0 \leq \sqrt{\bar{\beta}^2 + \bar{l}^2} < n_2 \\ \text{Tunneling rays} & n_2 < \sqrt{\bar{\beta}^2 + \bar{l}^2} \leq n_1 \text{ and } 0 \leq \bar{\beta} < n_2 \end{cases} \tag{2.19}$$

Again, the ray model can be fully characterised by the invariants $\bar{\beta}$ and $\bar{l}$. Similarly, one can define the path length L_p, optical path length L_o, and ray half-period z_p by:

$$L_p = 2a\frac{\mathrm{sin}\theta_\phi}{\mathrm{sin}\theta_z} = 2an_1\frac{\sqrt{n_1^2 - \bar{\beta}^2 - \bar{l}^2}}{n_1^2 - \bar{\beta}^2} \tag{2.20}$$

$$L_o = n_1 L_p = 2an_1\frac{\mathrm{sin}\theta_\phi}{\mathrm{sin}\theta_z} = 2an_1^2\frac{\sqrt{n_1^2 - \bar{\beta}^2 - \bar{l}^2}}{n_1^2 - \bar{\beta}^2} \tag{2.21}$$

$$z_p = L_p \mathrm{cos}\theta_z = 2a\frac{\mathrm{sin}\theta_\phi}{\mathrm{tan}\theta_z} = 2a\bar{\beta}\frac{\sqrt{n_1^2 - \bar{\beta}^2 - \bar{l}^2}}{n_1^2 - \bar{\beta}^2} \tag{2.22}$$

Applying the same method when calculating the ray transit time in Eq. (2.13) obtains the same expression because the ray transit time is independent of ray skewness.

2.3 Optical fibres

Optical fibres make use of cylindrical waveguides and behave like the backbone of modern optical communications. The inception of optical fibres can be traced back to the pioneering work of Charles Kao and George Hockham[55], the former of whom received the Nobel Prize in Physics in 2009 for his groundbreaking contributions to the understanding and development of optical fibre communication. A common optical fibre has a step-index refractive index profile as shown in Fig. 2.2. The very centre of the optical fibre is called the fibre core made of doped glass with a higher refractive index. The core is covered by the cladding, which together form the basic waveguide for optical fibre that allows light transmission. The cladding is often covered by different layers of coatings made of plastic such as polyacrylate

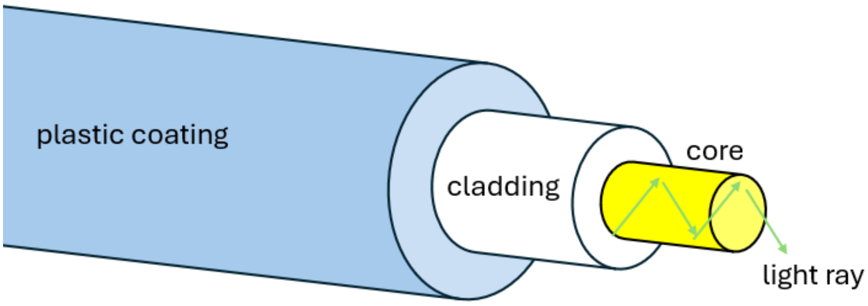

Figure 2.2: Structure of optical fibres.

or polymide to enhance the mechanical strength to overcome issues like bending. There are many types of optical fibres and the following is a brief introduction on some of typical ones categorised by some key features.

Refractive index profile

Firstly, there is an introduction on conventional fibres where light is combined within the core region. Depending on the doping method the refractive index profile near the core region can be either stepped or graded [56]. A step index fibre has a step-change in refractive index between the cladding and the core, where as a graded index has a gradual change in refractive index. Generally the design of graded-index fibres helps mitigate the limitations associated with modal dispersion, by equalising the optical path length between modes. This reduces pulse spreading, enabling for high-bandwidth and long-distance applications.

Number of modes

Commercial optical fibres can often be categorised by the number of modes. Those with smaller V number $V \lesssim 2.4$ are called single mode fibres (SMF) that only allow one propagation mode in their cores. While those with larger V number supporting more than one modes are called multi-mode fibres (MMF). In terms of sensing purposes it is often favourable to use SMF as there is only one refractive index of the propagation mode known as the effective refractive index.

Photonic crystal fibres

Photonic Crystal Fibres (PCFs) have a periodic array of airholes or voids. This design creates a photonic bandgap, enabling precise control over light propagation and offering tailored optical properties. Pioneering work in this field includes the foundational research on photonic crystal structures by Yablonovitch and John, laying the groundwork for the development of PCFs [57][58]. Photonic Crystal Fibres exhibit advantages such as customisable dispersion, broadband transmission, and enhanced nonlinear effects, making them versatile for applications in telecommunications, sensing, and nonlinear optics [59]. The ability to engineer specialty fibres with specific characteristics further expands their utility [59]. PCFs continue to drive innovation in photonics, contributing to the evolution of high-performance optical communication and sensing systems.

2.4 Fibre Bragg gratings

Fibre Bragg gratings (FBGs) are periodic or quasi-periodic structures written along an optical fibre that reflect light at wavelengths determined by their periodicity. They have been universally adopted as sensors for providing measurements of strain, temperature, pressure, and many other physical parameters in remote and inhospitable environments [1]. They are key components in telecommunication systems for dispersion compensation, filtering and multiplexing. They are also used as reflectors for semiconductor and fibre lasers as well as for pulse compression and stretching, along with many other applications.

The theory of coupling oppositely propagating modes by periodic exposure of the fibre core in an optical fibre was first reported in 1978 [26]. This periodic structure will reflect a certain wavelength of light satisfying: [60]

$$\lambda_B = 2n_{eff}\Lambda \tag{2.23}$$

which correlates the reflected Bragg wavelength λ_B with the effective refractive index of the fibre n_{eff} and period of the grating Λ. Fibre Bragg gratings are typically formed in an optical fibre, such that the refractive index of the core varies periodically along the fibre length Fig. 2.3. The reflected wavelength depends on the pitch and effective refractive index of the waveguide and the effect is accumulated as the number of periods increases.

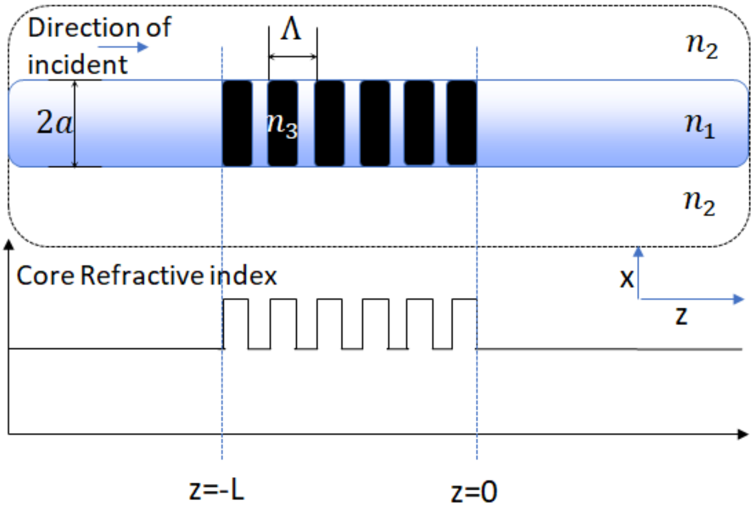

Figure 2.3: Illustration and refractive index profile of a Fibre Bragg Grating. n_1 is the core index, n_2 is the cladding index and n_3 is the modified core index. L is the length of the grating and a is the radius of the core. For a square-wave modulation in refractive index, there are Fourier harmonics, which allows higher order FBGs.

Special types of grating

If there is an abrupt change between the periodic modulation of the refractive index of the grating and the unmodulated regions at either end, then there will be side-lobes in the reflection spectrum. The process known as apodisation is used to solve this problem [61]. The amplitude of the modulated refractive index has a smooth transition from zero up to a maximum value and back down. This avoids the step-discontinuity which gives rise to the side-lobes. Various window functions can be used, for example raised cosine, Hamming, Hanning and many other. For a variety of applications including FBG sensors and optical filters, apodisation is necessary to remove the side lobes. A drawback is that apodised FBGs have lower effective FBG length and thus require extra physical length of FBG to retrieve an identical reflectance.

A chirped Fibre Bragg Grating (CFBG) has a grating period which instead of being constant, varies along the grating length. Typically, there would be a linear change in pitch with distance along the grating, but other chirp functions are possible. For instance, a flattened reflection band with controlled bandwidth can be formed by chirping [62]. The chirped FBGs can further be used to compensate for dispersion, which is an intrinsic property of a fibre especially in long distance optical communication systems due to different delay for light with different wavelengths [63].

Tilted Fibre Bragg Gratings (TFBGs) , unlike conventional FBGs, are specialized structures within optical fibres where the grating planes are angled. This tilt gives TFBGs unique spectral and polarisation properties, making them valuable for sensing and telecommunications [64]. They offer advantages such as enhanced sensitivity [65][66] and tunable spectral response [67], leading to their widespread use in various applications.

Long Period Gratings (LPGs) are another type of Fibre Bragg Gratings. While reflective FBGs have a short period (e.g.around 500 nm), LPGs operate in transmission by coupling light from the forward-propagating mode into cladding modes, resulting in the transmission spectrum exhibiting attenuation bands. LPGs are widely used in telecommunications [68], sensing [69], and optical filtering applications [70].

A comparison between different types of gratings are summarised in Table 2.1

Aspect	**FBG**	**CFBG**	**TFBG**	**LPG**
Functionality	Reflects single wavelength	A range of wavelengths	Multiple peaks by tilt angle	Cladding mode coupling
Bandwidth	0.1-1 nm	5-20 nm	5-20 nm	10-50 nm
Sensing Capability	High precision (~ 1 pm/$\mu\varepsilon$)	Distributed sensing (~ 10 pm/$\mu\varepsilon$)	Polarisation sensitive (~ 2 pm/$\mu\varepsilon$)	Broad spectral response (~ 10 pm/$\mu\varepsilon$)

Table 2.1: A comparison of FBG, CFBG, TFBG, and LPG

Fabrication methods

FBGs are crafted through diverse methods, each offering distinct advantages for specific applications. Historically, FBGs were fabricated using an ultraviolet (UV) laser to modify the fibre refractive index [15]. This required the fibre to be made photosensitive, either by loading it with hydrogen or by using a specially doped fibre (such as geranium-boron co-doped). The periodic modulation can be achieved by splitting the UV beam into two and combining them to form an interference pattern. Alternatively a phase mask can be used. More recently, femtosecond pulsed lasers in the infra-red and visible regions have beend used. These can also used with a phase masek. However, they can also be used to generate each period of the modulation individually on a point-by-point basis. Common techniques include the "point-by-point" method, utilizing a focused UV laser beam for creating periodic refractive index variations [71]. The phase mask technique involves using a patterned optical element to induce interference patterns and refractive index changes [72]. The Talbot interferometer technique combines the phase mask with the Talbot effect, ensuring a stable interference pattern for precise FBG inscription [73]. Additionally, femtosecond laser inscription provides ultrafast and controlled refractive index modifications [71] [74]. In this thesis, the focus will be mainly on the femtosecond laser fabrication method.

2.5 Fibre Bragg grating sensors

Fibre Bragg grating sensor for temperature and strain

The shift in Bragg wavelength $\Delta\lambda_B$ due to a change in temperature ΔT is given by: [16]

$$\frac{\Delta\lambda_B}{\lambda_B} = (\alpha + \xi)\Delta T = K_T \Delta T \tag{2.24}$$

where α is the thermal expansion coefficient and ξ is the thermo-optic coefficient of the fibre depending on the material used for fabrication. K_T is defined as the normalised thermal response for a FBG temperature sensor. Although α is a constant once the system is built, ξ is dependent on the effective refractive index given by:

$$\xi = \frac{\frac{dn_{eff}}{dT}}{n_{eff}} \tag{2.25}$$

When the fibre has homogeneous $\frac{dn_{eff}}{dT}$, ξ is a constant. However, if the cladding and core have different thermo-optic dependence, ξ will be a function of temperature and a non-linear response is expected.

Similar to temperature, an FBG sensor will also respond to strain that has been applied in the z direction $\Delta\epsilon$, given by: [16]

$$\frac{\Delta\lambda_B}{\lambda_B} = (1 - (\frac{n_{eff}^2}{2})[P_{12} - \mu(P_{11} + P_{12})]\Delta\epsilon = K_\epsilon \Delta\epsilon \tag{2.26}$$

where P_{ij} are the Pockel's coefficients of the stress-optic tensor, μ is the Poisson's ratio measuring variation in width against variation in length. Eq. (2.24) and Eq. (2.26) Eq. (2.26) presents how the relative shift of the Bragg wavelength depends on a change in temperature or strain. Thus, this relationship is important in designing FBG sensors.

Temperature and strain discrimination

An important issue that has concerned the sensing community is the cross-sensitivity between strain and temperature [26]. The thermal response of the change in wavelength of reflected light is due to both thermal expansion and the dependence of the refractive index on temperature, while the strain response arises from both the physical extension and the photoelastic effect[16]. For a typical silica FBG sensor at 1550 nm, the thermal response is approximately 11.3 pm/°C[75] and the strain response is approximately 1.2 pm/$\mu\epsilon$ [76]. As a result, it is not possible to monitor either temperature or strain with a single measurement of an FBG. Discrimination between temperature and strain has attracted widespread attention and continuous attempts have been made over the last four and a half decades [26].

There have been a number of reports of microstructured fibre with an array of holes in the cross-section that have been filled with liquid. Liquid, compared with fused silica that standard fibres are made of, presents a significant and negative thermo-optic coefficient dn/dT. For example, Naeem *et al.* were able to achieve a modest change in temperature sensitivity using methanol-filled holes [46]. Alternatively, Huy *et al.* showed plots with flattened temperature response over a limited temperature range but did not show spectra for the filled fibres [47]. It is likely that such a configuration would be multi-moded and there is no information on loss. Very recently a fibre with a filled 2 μm hollow core showed high temperature sensitivity, but with very high loss and poor spectra [48]. There have been theoretical papers proposing filled microstructured fibres for low temperature sensitivity [49][50] and high temperature sensitivity [51], but these designs were not realized experimentally. A design framework for microengineering the temperature coefficients of FBGs over specified temperature ranges will be introduced, which could help solve this historical problem.

The shift in Bragg wavelength $\Delta\lambda_B$ due to a change in temperature and strain is given by [16].

$$\frac{\Delta\lambda_B}{\lambda_B} = \left(1 - \left(\frac{n_{eff}^2}{2}\right)\left[P_{12} - \nu\left(P_{11} + P_{12}\right)\right]\right)\Delta\epsilon + (\alpha + \xi)\Delta T \tag{2.27}$$

$$= K_\epsilon \Delta\epsilon + K_T \Delta T \tag{2.28}$$

where and α is the thermal expansion coefficient of the fibre. $\Delta\epsilon$ and ΔT are the changes in strain and temperature, respectively. For an FBG sensor with known K_ϵ and K_T, a single measurement of $\Delta\lambda_B$ is not sufficient to calculate both $\Delta\epsilon$ and ΔT. One solution is to take two measurements of the Bragg wavelength with two distinctive systems placed in the same environment in terms of temperature and strain [77][46]. Then temperature and strain discrimination can be achieved by solving the matrix:

$$\begin{pmatrix} \Delta\lambda_1 \\ \Delta\lambda_2 \end{pmatrix} = \begin{pmatrix} K_{\epsilon 1} & K_{T1} \\ K_{\epsilon 2} & K_{T2} \end{pmatrix} \begin{pmatrix} \Delta\epsilon \\ \Delta T \end{pmatrix} \tag{2.29}$$

where subscripts 1 and 2 are for the different FBG sensors mentioned above. By observing Eq. (7.1) it is noticed that in order to solve for the matrix, the two systems should have either distinctive K_ϵ or K_T. In addition, since the thermal response and strain response are also indicators of sensitivity of the FBG sensors, the aim is to design FBG sensors with a value of K_ϵ or K_T which is significantly higher than conventional ones. As both of them are dependent on the effective refractive index, one could design waveguides that give a suitable value of n_{eff}.

2.6 Conclusion

In this chapter, a brief background of optical waveguide, optical fibres, FBGs, and FBG sensors has been provided. The literature was also reviewed in the relevant fields of research. The theories mentioned in this chapter will not only be used for simulation techniques but also be used to illustrate the idea of designing novel FBG devices, both of which will be introduced in the later chapters

3

Modelling techniques

Contents

3.1 Introduction

In this chapter, analytic methods and computer simulations are used to model the optical waveguide devices. Firstly, there are analytical simulation methods for

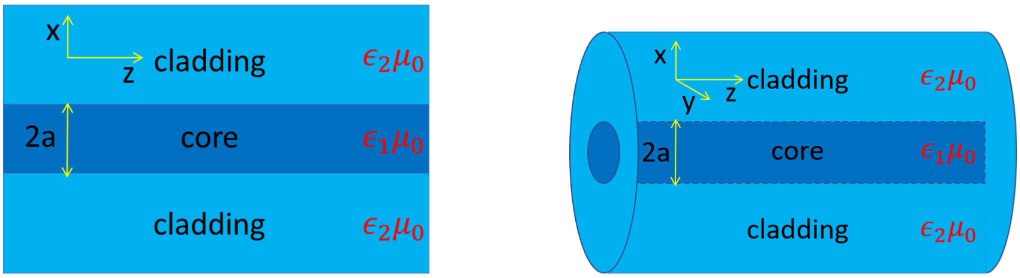

(a) Slab Waveguide **(b)** Cylindrical Waveguide

Figure 3.1: Sketch of planar and cylindrical Waveguides. Incident light is propagating along the z-axis and bouncing between the core-cladding interfaces.

some standard symmetrical waveguides such as a planar waveguide, a cylindrical waveguide and a double-cladding waveguide. This is followed by computer-based simulation techniques. There are also comparisons and comments on each method and the rationale for choosing a particular method.

3.2 Analytical waveguide theories

The analysis in this section is based on [78]. The cross-sections and the coordinates of a planar and a cylindrical waveguide are shown in Fig. 3.1 The light bound in the waveguide is expressed by the electric and magnetic field vectors **E**(x,y,z) and **H**(x,y,z), respectively, in terms of a finite sum of transverse resonances, known as modes. The field distribution of jth order for forward and backward propagating modes are denoted with $\mathbf{E}_j(x,y,z)$, $\mathbf{H}_j(x,y,z)$ and $\mathbf{E}_{-j}(x,y,z)$, $\mathbf{H}_{-j}(x,y,z)$, respectively. Assuming that only spatial variances exist, the modal fields can be expressed by:

$$\mathbf{E}_j(x,y,z) = \mathbf{e}_j(x,y)e^{i\beta_j z} \tag{3.1}$$

$$\mathbf{H}_j(x,y,z) = \mathbf{h}_j(x,y)e^{i\beta_j z} \tag{3.2}$$

where **e** and **h** are fields in the xy plane and β_j is the propagation constant of the jth order. Similar to the ray invariant $\bar{\beta}$ in the ray approach, the propagation constant β can be used to characterise the modes. Given the frequency ω of incident light the phase velocity is:

$$v_p = \frac{\omega}{\beta} \tag{3.3}$$

The phase velocity must be within the limit of minimum and a maximum speed of light that are c/n_1 and c/n_2, respectively. Therefore, without consideration of the refractive index profile of the waveguide it is obvious that the range of the propagation constant for any modes is:

$$n_2 k < \beta_j \leq n_1 k \tag{3.4}$$

where $k = 2\pi/\lambda$ is the free space wavenumber.

The fields can be separated by direction in terms of transverse and longitudinal with respect to the propagating direction denoted by $\perp$ and z, respectively.

$$\mathbf{E} = (\mathbf{e}_\perp + e_z \hat{\mathbf{z}})e^{i\beta z} \tag{3.5a}$$

$$\mathbf{H} = (\mathbf{h}_\perp + h_z \hat{\mathbf{z}})e^{i\beta z} \tag{3.5b}$$

where $\hat{z}$ is the unit vector in the z-direction.

The fields can be solved using Maxwell's equations. Assuming the time dependence is given by $e^{-i\omega t}$, permittivity $\epsilon(x, y, z)$ is a function of refractive index as $\epsilon = n^2\epsilon_0$ and the permeability μ is constant $\mu = \mu_0$, Maxwell's equations can then be written as [79]

$$\nabla \times \mathbf{E} = i\sqrt{\frac{\mu_0}{\epsilon_0}}k\mathbf{H} \tag{3.6a}$$

$$\nabla \times \mathbf{H} = \mathbf{J} - i\sqrt{\frac{\epsilon_0}{\mu_0}}kn^2\mathbf{E} \tag{3.6b}$$

$$\nabla \cdot (n^2\mathbf{E}) = \frac{\sigma}{\epsilon} \tag{3.6c}$$

$$\nabla \cdot \mathbf{H} = 0 \tag{3.6d}$$

where ϵ_0 and μ_0 are the permittivity and permeability of free space, respectively, λ is the wavelength of the incident light.

Substituting fields described in Eq. (3.5) into Maxwell's equations in Eq. (3.6) and assuming $\mathbf{J}$=0, σ=0. The field components in the transverse and longitudinal directions are:

$$\mathbf{e}_\perp = -\sqrt{\frac{\mu_0}{\epsilon_0}}\frac{1}{kn^2}\hat{\mathbf{z}} \times \{\beta \mathbf{h}_\perp + i\nabla_\perp h_z\} \tag{3.7a}$$

$$\mathbf{h}_\perp = \sqrt{\frac{\epsilon_0}{\mu_0}}\frac{1}{k}\hat{\mathbf{z}} \times \{\beta \mathbf{e}_\perp + i\nabla_\perp e_z\} \tag{3.7b}$$

$$e_z = i\sqrt{\frac{\mu_0}{\epsilon_0}}\frac{1}{kn^2}\hat{\mathbf{z}} \cdot \nabla_\perp \times \mathbf{h} = \frac{i}{\beta}\{\nabla_\perp \cdot \mathbf{e}_\perp + (\mathbf{e}_\perp \cdot \nabla_\perp)\mathrm{ln} n^2 \tag{3.7c}$$

$$h_z = -i\sqrt{\frac{\epsilon_0}{\mu_0}}\frac{1}{k}\hat{\mathbf{z}} \cdot \nabla_\perp \times \mathbf{e}_\perp = \frac{i}{\beta}\nabla_\perp \cdot \mathbf{h}_\perp \tag{3.7d}$$

where the core refractive indices follows a spatial function $n = n(x, y)$. $\nabla_\perp$ is the vector differential operator of the transverse directions x and y only. From Eq. (3.7d) transverse fields can be written in terms of the longitudinal fields [80]

$$\mathbf{e}_\perp = \frac{i}{k^2n^2 - \beta^2}\{\beta\nabla_\perp e_z - \sqrt{\frac{\mu_0}{\epsilon_0}}k\hat{\mathbf{z}} \times \nabla_\perp h_z\} \tag{3.8a}$$

$$\mathbf{h}_\perp = \frac{i}{k^2n^2 - \beta^2}\{\beta\nabla_\perp h_z - \sqrt{\frac{\epsilon_0}{\mu_0}}kn^2\hat{\mathbf{z}} \times \nabla_\perp e_z\} \tag{3.8b}$$

If either the **E** or **H** fields from Eq. (3.6) are eliminated, the inhomogeneous vector wave equations are obtained

$$\{\nabla^2 + n^2k^2\}\mathbf{E} = -\nabla(\mathbf{E} \cdot \nabla\mathrm{ln}\ n^2) - i\sqrt{\frac{\mu_0}{\epsilon_0}}k\mathbf{J} + \frac{1}{k}\nabla(\frac{\nabla \cdot \mathbf{J}}{n^2}) \tag{3.9a}$$

$$\{\nabla^2 + n^2k^2\}\mathbf{H} = (\nabla \times \mathbf{H}) \times \nabla_\perp\mathrm{ln}\ n^2 - \nabla \times \mathbf{J} - \mathbf{J} \times \nabla_\perp\mathrm{ln}\ n^2 \tag{3.9b}$$

where, by simplification, it is assumed that all the operators are scalar. When there is no external source, the homogenerous vector wave equations become:

$$\{\nabla_\perp^2 + n^2k^2 - \beta^2\}\mathbf{e} = -(\nabla_\perp + i\beta\hat{\mathbf{z}})\mathbf{e}_\perp \cdot \nabla_\perp\mathrm{ln}\ n^2) \tag{3.10a}$$

$$\{\nabla_\perp^2 + n^2k^2 - \beta^2\}\mathbf{h} = \{(\nabla_\perp + i\beta\hat{\mathbf{z}}) \times \mathbf{h}\} \times \nabla_\perp\mathrm{ln}\ n^2) \tag{3.10b}$$

For a step-index planar waveguide all terms in the vector wave equation in Eq. (3.10) involving $\nabla_\perp\mathrm{ln}\ n^2$ vanish because of the homogeneous refractive index within the core and cladding. Therefore, the vector wave equation is reduced to:

$$\{\nabla_\perp^2 + n^2k^2 - \beta_j^2\}\Psi = 0 \tag{3.11}$$

where Ψ denotes either e_z or h_z

In order to describe the modal fields, two dimensionless parameters U_j and W_j are introduced for the core and cladding, respectively, given by:

$$U_j = a\sqrt{k^2 n_1^2 - \beta_j^2} \tag{3.12}$$

$$W_j = a\sqrt{\beta_j^2 - k^2 n_2^2} \tag{3.13}$$

so that by definition of the normalised frequency V, the parameters satisfy:

$$U_j^2 + W_j^2 = V^2 \tag{3.14}$$

3.2.1 Step-index planar waveguide

The cross-section of a step-index planar waveguide is shown in Fig. 3.1a. The boundary conditions for Maxwell's equation apply only when $\mathbf{h}$ and $\mathbf{e}_\perp$ are continuous at the interface between the core and cladding. Substituting the refractive index profile of Eq. (2.4) into the scalar wave equation, Eq. (3.11), yields:

$$\begin{cases} \{a^2 \frac{d^2}{dx^2} + U^2\}\Psi = 0 & 0 \leq |x| < a \\ \{a^2 \frac{d^2}{dx^2} - W^2\}\Psi = 0 & a \leq |x| < \infty \end{cases} \tag{3.15}$$

Solving the equations with the boundary condition $|x| = a$ yields the eigenvalue equations as:

$$\begin{cases} \text{Even TE modes} & W = U\tan U \\ \text{Odd TE modes} & W = -U\cot U \\ \text{Even TM modes} & n_1^2 W = n_2^2 U\tan U \\ \text{Odd TM modes} & n_1^2 W = -n_2^2 U\cot U \end{cases} \tag{3.16}$$

The transcendental equation can be solved numerically. A graphic solution for the transverse electric (TE) modes of a slab waveguide is plotted in Fig. 3.2, where each intersection of the left hand side (LHS) and the right hand side (RHS) indicates a different mode. An even mode has symmetrical E_y about the $x = 0$ axis and an odd mode has asymmetrical E_y.

Solving for U and W gives the propagation constant β and thus the effective refractive index n_{eff} of this mode:

$$n_{eff} = \frac{\beta\lambda}{2\pi} \tag{3.17}$$

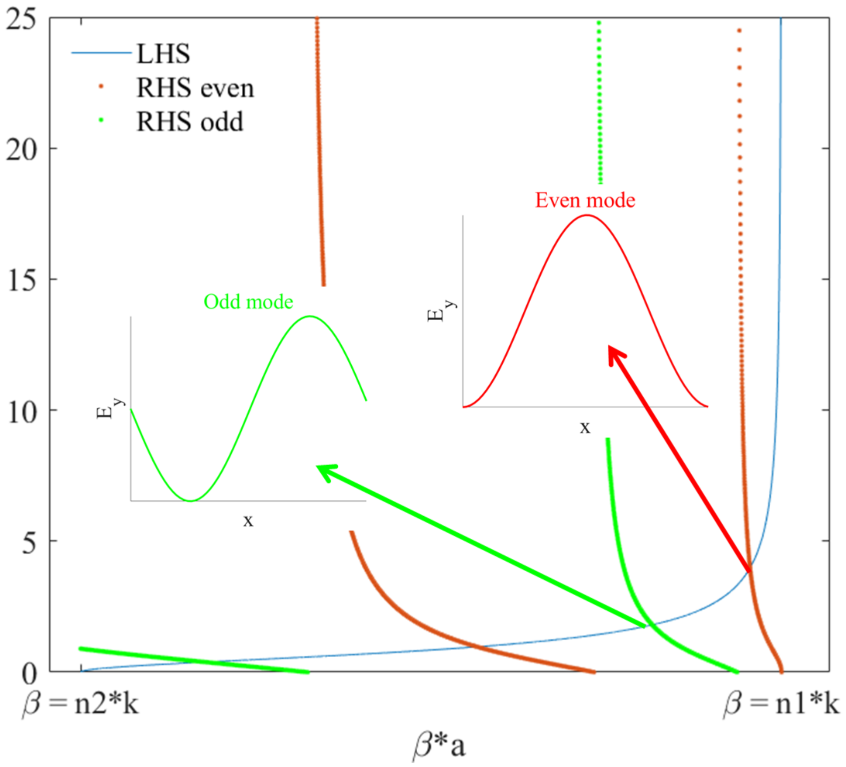

Figure 3.2: A graphic solution for the TE modes in Eq. (3.16) (slightly modified). LHS and RHS are plotted against the dimensionless product of the propagation constant β and radius of core a.

3.2.2 Step-index Cylindrical Waveguide

The cross-section of a step-index cylindrical waveguide is shown in Fig. 3.1b. Similarly for a cylindrical waveguide, the scalar wave equations are:

$$\begin{cases}\{\frac{\partial^2}{\partial R^2}+\frac{1}{R}\frac{\partial}{\partial R}+\frac{1}{R^2}\frac{\partial^2}{\partial \phi^2}+U^2\}\Psi=0 & 0\leq R<1\\ \{\frac{\partial^2}{\partial R^2}+\frac{1}{R}\frac{\partial}{\partial R}+\frac{1}{R^2}\frac{\partial^2}{\partial \phi^2}-W^2\}\Psi=0 & 1\leq R<\infty\end{cases} \tag{3.18}$$

where R is the normalised radius given by $R=\frac{r}{a}$

As before, these equations are solved by applying the boundary condition $R=1$. The fundamental modes have the eigenvalue equations given by:

$$\begin{cases}TE_{0m}\text{modes} & \frac{J_1(U)}{UJ_0(U)}+\frac{K_1(W)}{WK_0(W)}=0\\ TM_{0m}\text{modes} & \frac{n_1^2J_1(U)}{UJ_0(U)}+\frac{n_2^2K_1(W)}{WK_0(W)}=0\end{cases} \tag{3.19}$$

where J_i is a Bessel function and K_i is a modified Hankel function of i^{th} order.

3.2.3 Double-Cladding Waveguide

A double-cladding waveguide is a standard cylindrical waveguide with another layer of cladding around the core, forming an inner cladding with index, n_{inner}. One type of double-cladding waveguide is a depressed cladding waveguide in which the refractive index of the inner cladding is less than the outer cladding A solution for a depressed cladding waveguide has been derived [81][82] for dispersion compensation in telecommunications systems. Although this solution was for waveguides where the inner cladding has a lower refractive index than the outer material, it also holds true for cases where the inner cladding has a higher refractive index. The propagation constant β of a single-mode double-cladding waveguide can be found by the following equation[82]:

$$\begin{aligned}
&[\gamma J_0(\kappa a)I_1(\gamma a)+\kappa J_1(\kappa a)I_0(\gamma a)]\\
&\times[\delta K_0(\gamma b)K_1(\delta b)-\gamma K_1(\gamma b)K_0(\delta b)]\\
&+[\gamma J_0(\kappa a)K_1(\gamma a)-\kappa J_1(\kappa a)K_0(\gamma a)]\\
&\times[\delta I_0(\gamma b)K_1(\delta b)+\gamma I_1(\gamma b)K_0(\delta b)]=0
\end{aligned}\tag{3.20}$$

where K_ν, J_ν, and I_ν are the modified Hankel, Bessel, and modified Bessel functions of order ν, respectively. a is the radius of the core and b is the radius of the inner cladding. The outer cladding is assumed to have an infinite radius. The terms in Eq. (4.1) are defined as:

$$\begin{aligned}
\kappa &= \sqrt{n_{cl}^2(1+\Delta)^2k^2-\beta^2}\\
\gamma &= \sqrt{\beta^2-n_{cl}^2(1+\Delta')k^2}\\
\delta &= \sqrt{\beta^2-n_{cl}^2\kappa^2}\\
\Delta &= (n_{co}-n_{cl})/n_{cl}\\
\Delta' &= (n_{co}-n_{inner})/n_{cl}
\end{aligned}\tag{3.21}$$

where n_{co}, n_{inner} and n_{cl} are refractive indices of the fibre core, inner cladding, and outer cladding, respectively, β is the propagation constant and k is the wavenumber.

3.3 Analytical FBG simulation

3.3.1 Coupled Wave Equation

The analysis here is based on that in [83]. Analysis of an FBG can be simplified to a 1-D grating structure as shown in Fig. 3.3. The model consists of a sinusoidal dielectric variation in the z-direction with an incident plane wave polarised along the x axis. If the FBG is written point by point with a femtosecond laser, the resulting refractive index modulation would be more like a square-wave profile. However, there will be sinusoidal Fourier components.

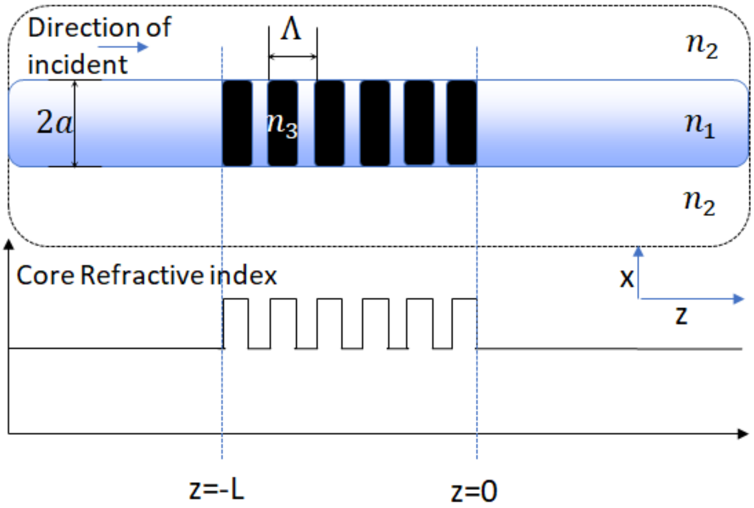

Figure 3.3: Illustration and refractive index profile of a Fibre Bragg Grating. n_1 is the core index, n_2 is the cladding index and n_3 is the modified core index. L is the length of the grating and a is the radius of the core. For a square-wave modulation in refractive index, there are Fourier harmonics, which allows higher order FBGs.

The Helmholtz equation for the E field is given by:

$$\nabla^2 E + n^2 (z) k_0^2 E = 0 \tag{3.22}$$

where $n(z)$ is the refractive index of the 1-D structure as a function of length z and k_0 is the free space wavenumber satisfying:

$$k_0^2 = \omega^2 \epsilon_0 \mu_0 = \frac{2\pi}{\lambda_0} \tag{3.23}$$

where λ_0 is the free-space wavelength of the incident light. The index variation along the z axis can be written as:

$$n^2(z) = [n_{eff} + \delta n \cos(Kz)]^2 \approx {n_{eff}}^2 + n_{eff}\delta n[e^{i(Kz)} + e^{-i(Kz)}] \tag{3.24}$$

where δn is the index modification of the grating assuming $\delta n << n$, and n_{eff} is the effective refractive index along the grating. $K = 2\pi/\Lambda$ with Λ representing the pitch of the grating. It is also assumed that although the incident wave is along the -z-direction, a wave is also generated along the +z direction due to the grating. The E fields along the x axis can be written as a superposition.

$$E_x = E_+ + E_- = A(z)\, e^{-i\beta z} + B(z)\, e^{i\beta z} \tag{3.25}$$

where $A(z)$ and $B(z)$ are amplitudes dependent on the longitudinal distance z. β is the propagation constant in a waveguide with homogeneous dielectric constant given by $\beta = n_{eff}k_0$. By substituting Eq. (3.25) and Eq. (3.24) into Eq. (3.22) the following is obtained:

$$2i\beta\left(\frac{dA}{dz}e^{-i\beta z} - \frac{dB}{dz}e^{i\beta z}\right) = k_0^2 n_{eff}\delta n\left[e^{i(Kz)} + e^{-i(Kz)}\right]\left(Ae^{-i\beta z} + Be^{i\beta z}\right) = 0 \tag{3.26}$$

where the Slowly Varying Envelope Approximation is applied[84] and it is assumed that the dependence of $A(z)$ and $B(z)$ on distance z is sufficiently small that $\frac{d^2A}{dz^2} \ll \frac{1}{\lambda_0}\frac{dA}{dz}$. Given a small detuning factor $\delta k = \beta - \frac{K}{2}$ thus $K \approx 2\beta$ the terms including $e^{i\beta z}$ and $e^{-i\beta z}$ are matched, while the others are withdrawn. This leads to:

$$\frac{dA}{dz} = -i\kappa B e^{i(2\delta k z)} \tag{3.27}$$

$$\frac{dB}{dz} = i\kappa A e^{i(-2\delta k z)} \tag{3.28}$$

The equations Eq. (3.27) and Eq. (3.28) are one form of coupled wave equation for Bragg gratings. κ is the coupling coefficient. For a fibre, κ is defined as [85]:

$$\kappa = \frac{\pi\delta n}{\lambda_B}\Gamma \tag{3.29}$$

where λ_B is the Bragg wavelength and Γ is the confinement factor of the fibre core given by :

$$\Gamma \approx 1 - V^{-2} \tag{3.30}$$

where V is the normalised frequency parameter of a fibre defined in Chapter 2 Section 2.2 and can be written as:

$$V = \frac{2\pi a}{\lambda}\sqrt{n_1^2 - n_2^2} = \frac{2\pi a}{\lambda} NA \tag{3.31}$$

where n_1 and n_2 are core and cladding refractive indices, respectively, λ is the wavelength of the wave in vacuum, a is the radius of the fibre core.

3.3.2 Reflection Coefficient of Bragg gratings

In order to solve the coupled wave equations, the following terms are defined as:

$$a(z) = e^{-i\delta k z} A(z) \tag{3.32}$$

$$b(z) = e^{i\delta k z} B(z) \tag{3.33}$$

Eq. (3.27) and Eq. (3.28) can be expressed by:

$$\frac{d}{dz}\begin{pmatrix} a \\ b \end{pmatrix} = i \begin{bmatrix} -\delta k & -\kappa \\ \kappa & \delta k \end{bmatrix} \begin{pmatrix} a \\ b \end{pmatrix} \tag{3.34}$$

So that by taking the derivatives of Eq. (3.34) the decoupled equations can be written:

$$\frac{d^2}{dz^2}\begin{pmatrix} a \\ b \end{pmatrix} = S^2 \begin{pmatrix} a \\ b \end{pmatrix} \tag{3.35}$$

where $S^2 = \kappa^2 - \delta k^2$. Therefore, a reasonable prediction of solutions to a and b is:

$$a = a_+ e^{-Sz} + a_- e^{Sz} \tag{3.36}$$

$$b = b_+ e^{-Sz} + b_- e^{Sz} \tag{3.37}$$

To verify the prediction, the derivatives of Eq. (3.36) and Eq. (3.37) are taken and substituted into Eq. (3.34), yielding:

$$\frac{da}{dz} = -Se^{-Sz}a_+ + Se^{Sz}a_- = -i\delta k a - i\kappa b \tag{3.38}$$

$$\frac{db}{dz} = -Se^{-Sz}b_{+} + Se^{Sz}b_{-} = i\kappa a + i\delta kb \tag{3.39}$$

Some manipulation gives the four equations:

$$b_{\pm} = \frac{\mp S + i\delta k}{-i\kappa}a_{\pm} \tag{3.40}$$

$$a_{\pm} = \frac{\mp S - i\delta k}{i\kappa}b_{\pm} \tag{3.41}$$

Solving for any pairs that are composed of identical variables gives:

$$S^{2} = \kappa^{2} - \delta k^{2} \tag{3.42}$$

Now it has been confirmed that Eq. (3.36) and Eq. (3.37) are the general solutions. Then the boundary conditions are applied. At the surface of reflection the field is reduced to zero. From Eq. (3.37), and applying b=0 at z=0, gives:

$$b_{+} = -b_{-} \tag{3.43}$$

Eq. (3.37) can therefore be written as:

$$b = b_{+}e^{-Sz} + b_{-}e^{Sz} = -\left(b_{+}e^{Sz} - b_{+}e^{-Sz}\right) = -2b_{+}\mathrm{sinh}(Sz) \tag{3.44}$$

By substituting Eq. (3.44) into Eq. (3.34) a can be solved as:

$$\frac{db}{dz} = -2b_{+}\left(S\mathrm{cosh}Sz\right) = i\left(\kappa a + \delta kb\right) \tag{3.45}$$

$$a = \frac{-2b_{+}S\mathrm{cosh}\left(Sz\right) + i2b_{+}\delta k\mathrm{sinh}(Sz)}{i\kappa} = -\frac{2b_{+}}{i\kappa}\left(S\mathrm{cosh}\left(Sz\right) - i\delta k\mathrm{sinh}\left(Sz\right)\right) \tag{3.46}$$

$$A = -\frac{2b_{+}}{i\kappa}\left(S\mathrm{cosh}\left(Sz\right) - i\delta k\mathrm{sinh}\left(Sz\right)\right)e^{-i\delta kz} \tag{3.47}$$

$$B = -2b_{+}\mathrm{sinh}(Sz)\,e^{i\delta kz} \tag{3.48}$$

Now after removing the phase terms the field amplitude reflection coefficient for the Bragg grating can be obtained:

$$r = \frac{B}{A} = \frac{\kappa \sinh(-Sl)}{S\cosh(Sl) + i\delta k \sinh(Sl)} \tag{3.49}$$

The field reflection amplitude coefficient can be written in a more consistent form as in[86]:

$$r = \frac{i\kappa \sinh(-SL_g)}{-\Delta\beta \sinh(SL_g) + iS\cosh(SL_g)} \tag{3.50}$$

where $S^2 = \kappa^2 - \delta k^2$, $L_g = l$ which represents the length of the grating and $\Delta\beta = \delta k$ is the detuning factor telling how far the propagation constant is from the wavenumber of the grating. The intensity reflection R is therefore the modulus squared of Eq. (3.50):

$$R = |\frac{i\kappa \sinh(-SL_g)}{-\Delta\beta \sinh(SL_g) + iS\cosh(SL_g)}|^2 \tag{3.51}$$

3.3.3 Bragg wavelength and Bandwidth

The Bragg wavelength is defined as the resonance wavelength where the peak reflection occurs. At resonance $\delta k = 0$ and by definition:

$$n_{eff}\frac{2\pi}{\lambda_0} = \frac{\pi}{\Lambda} \tag{3.52}$$

This leads to the Bragg condition:

$$\lambda_B = 2n_{eff}\Lambda \tag{3.53}$$

which gives a relation between the Bragg wavelength λ_B, effective refractive index n_{eff} and the period of grating Λ. At the Bragg wavelength, $\Delta\beta$ in Eq. (3.51) is zero. The equation becomes:

$$R_{max} = \tanh^2(\kappa L_g) \tag{3.54}$$

where R_{max} indicates the maximum reflection at the Bragg wavelength. The reflection spectrum is plotted against wavelength in Fig. 3.4 for different values of κ (by varying δn) and L_g according to Eq. (3.51). In Fig. 3.4, it is apparent both κ

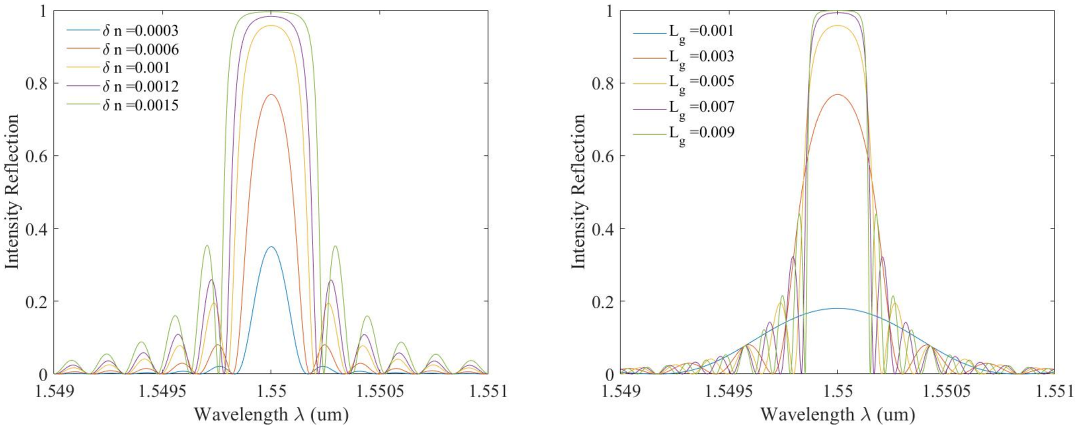

(a) Relative intensity spectrum for different values of δn

(b) Relative intensity spectrum for different values of L_g

Figure 3.4: Intensity Reflection as a function of wavelength λ for various (a) Coupling coefficient κ (or grating index modification δn) and (b) length of grating L_g.

and L_g contribute to a stronger reflection. The reflectivity eventually saturates at higher κL such that further increase in coupling coefficient or length results in only minimal increase in reflectivity. As the grating gets stronger, the bandwidth gets wider due to the reflection occurring predominantly from the front of the grating. As a result, the effective grating length reduces.

Another important figure of merit is the bandwidth measured by the wavelength between the two zeros nearest to the Bragg wavelength. Taking the numerator of Eq. (3.51) the reflected power (reflectance) is written as:

$$R \propto \sinh^2(-SL_g) \tag{3.55}$$

Since $\sinh(x)$ is not a periodic function, some manipulation is needed with the rule $i\sin(x) = \sinh(ix)$ and substituting for $S^+ = \sqrt{\kappa^2 - \Delta\beta^2}$. Assuming the detuning factor δk is small so that S^+ is real, Eq. (3.55) can be written as:

$$R \propto \sinh^2(-iS^+L_g) \tag{3.56}$$

$$\propto \sin^2(-S^+L_g) \tag{3.57}$$

Now it is obvious that the zeros occur at (and taking the symmetry of $\sin^2(x)$)

$$-S^+L_g = n\pi \tag{3.58}$$

where $n = 1, 2, 3, ...$ So at the first minimum the condition $-S^{+}L_g = \pi$ should be satisfied. By expressing this equation in terms of wavelength in order to find the bandwidth, the $\Delta\beta$ can be written as:

$$\Delta\beta = \beta - \frac{K}{2} \tag{3.59}$$

$$= 2\pi n_{eff}(\frac{1}{\lambda} - \frac{1}{\lambda_B}) \tag{3.60}$$

By defining $\Delta\lambda = \lambda - \lambda_B$ and assuming $\Delta\lambda << \lambda_B$ one obtains:

$$\Delta\beta = 2\pi n_{eff}\frac{\Delta\lambda}{\lambda_B^2} \tag{3.61}$$

By combining Eq. (3.58) and Eq. (3.61) the bandwidth can be written as [87]:

$$\Delta\lambda = \frac{\lambda_B^2}{L_g n_{eff}}\sqrt{(\frac{\kappa L_g}{\pi})^2 + 1} \tag{3.62}$$

From Fig. 3.5, the bandwidth increases for a shorter L_g and a larger δn. This indicates that in order to obtain a narrow peak, an FBG system with a lower κ and a longer grating length L_g is preferred.

3.4 Numerical simulation methods

There are a number of numerical simulation methods that can be employed in order to model waveguides. Various numerical techniques, including Finite-Difference method (FDM), Finite Element Method (FEM) and Film Mode-Matching (FMM) Method, offer effective tools to study waveguide characteristics, such as mode propagation, dispersion, coupling, and losses. Compared with the analytical waveguide theories, these methods provide fully vectorial calculation and they are easier to deal with complex structures of waveguides. Here there will be a brief introduction on different mode solving methods that are accessible from the numerical waveguide simulation software FIMMWAVE [88].

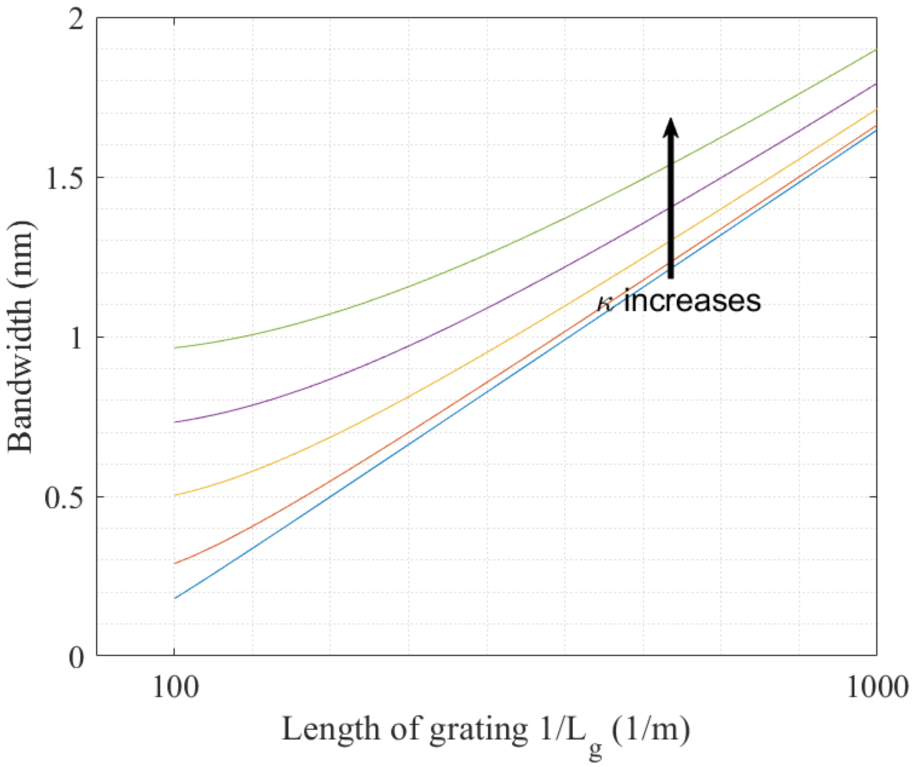

Figure 3.5: Bandwidth between two zeros nearest to Bragg wavelength as a function of the length of the grating L_g for different values of the coupling coefficient κ from 0.0001π to 0.0005π.

3.4.1 Film mode matching (FMM) method

The FMM method is a semi-analytical method suitable for waveguide structures with a rectangular geometry. The method operates by decomposing the waveguide structure into discrete layers and applying mode matching principles at each interface to solve for the propagation constants and modal profiles of guided modes. It is particularly efficient to calculate modes for structures with very thin layers such as quantum wells. Meanwhile, it works extremely well for bend modes. However, the FMM method is generally not accurate for cylindrical waveguides.

3.4.2 Finite-difference mode (FDM) method

Among the suite of numerical simulation methods for waveguides, the FDM solver stands out for its simplicity and effectiveness in characterizing guided modes within waveguide structures. FDM discretises both the transverse spatial domain and the longitudinal propagation direction, allowing for accurate determination of mode profiles, propagation constants, and dispersion characteristics. This makes it particularly well suited to model waveguides with high-step refractive index profiles, slanting/curved interfaces and gradient profiles. It is therefore a very good choice for applications in silicon photonics. However, FDM is less effective with complex mixed geometries due to its intrinsic rectangular meshing as shown in Fig. 3.6a.

3.4.3 Finite element mode (FEM) method

The FEM method discretises the domain of interest into smaller, interconnected elements, allowing for the approximation of complex geometries and material properties as shown in Fig. 3.6b. By formulating the governing equations within each element and enforcing continuity across element interfaces, FEM enables accurate solutions to waveguide problems, including mode propagation, scattering, and coupling phenomena. FEM's flexibility in handling arbitrary geometries, non-uniform material distributions, and boundary conditions makes it particularly well-suited for studying diverse waveguide structures.

3.4.4 Fibre solvers

There are two types of fibre solvers that are accessible from FIMMWAVE, the general fibre solver (GFS) and the Finite-Difference Fibre Solver (FDFS). These methods offer a faster alternative by employing circular coordinates and symmetry. There are also scalar versions of these two methods that use the same condition as the analytical solutions, making them suitable for initial investigations. Again, they can not be used to deal with arbitrary geometries.

3.4.5 EigenMode Expansion (EME)

The Eigenmode Expansion (EME) Method is a powerful computational technique employed in the analysis and design of waveguides and optical structures for three-dimensional analysis. It relies on decomposing the electromagnetic field distribution within the waveguide into a superposition of its constituent eigenmodes, each

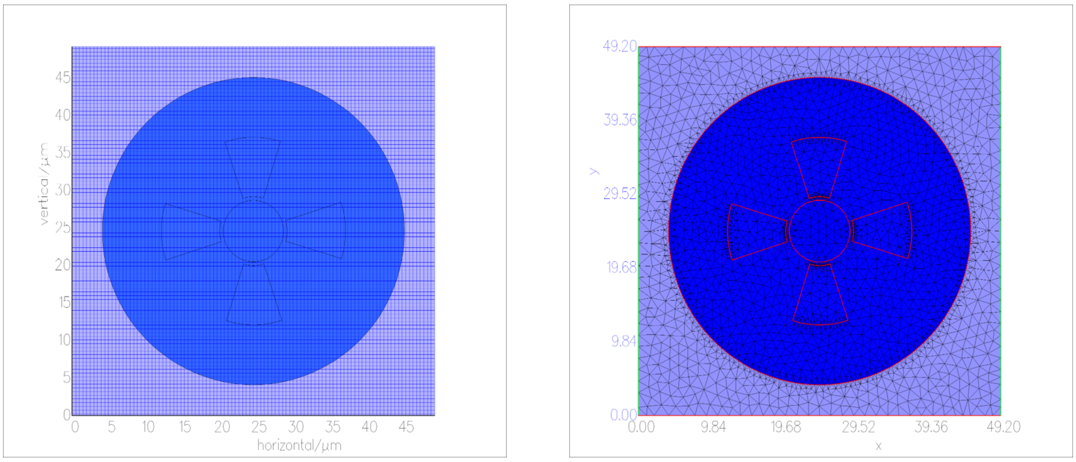

(a) **(b)**

Figure 3.6: Examples of (a) FDM and (b) FEM meshing on the same waveguide cross section. The FDM method is more suitable for rectangular shaped structures while the FEM method can deal with more complex structures with its triangular meshing. Figures plotted by FIMMWAVE.

characterised by a unique propagation constant and modal profile. By solving the eigenvalue problem associated with the waveguide structure, EME enables the determination of these modes and their corresponding coefficients, allowing for an accurate representation of the field distribution. The EME method has been employed for three-dimensional FBG simulation that will be illustrated in the later chapters.

3.5 Comparison between analytical and numerical methods

Now it is necessary to test the stability of simulation methods by comparing the analytical and numerical solutions. The performance test introduced in this section introduces how different methods are used for the two simplest waveguides, a slab waveguide and a cylindrical waveguide. The aim of the performance tests are to verify that the simulation tool is well-understood and reliable.

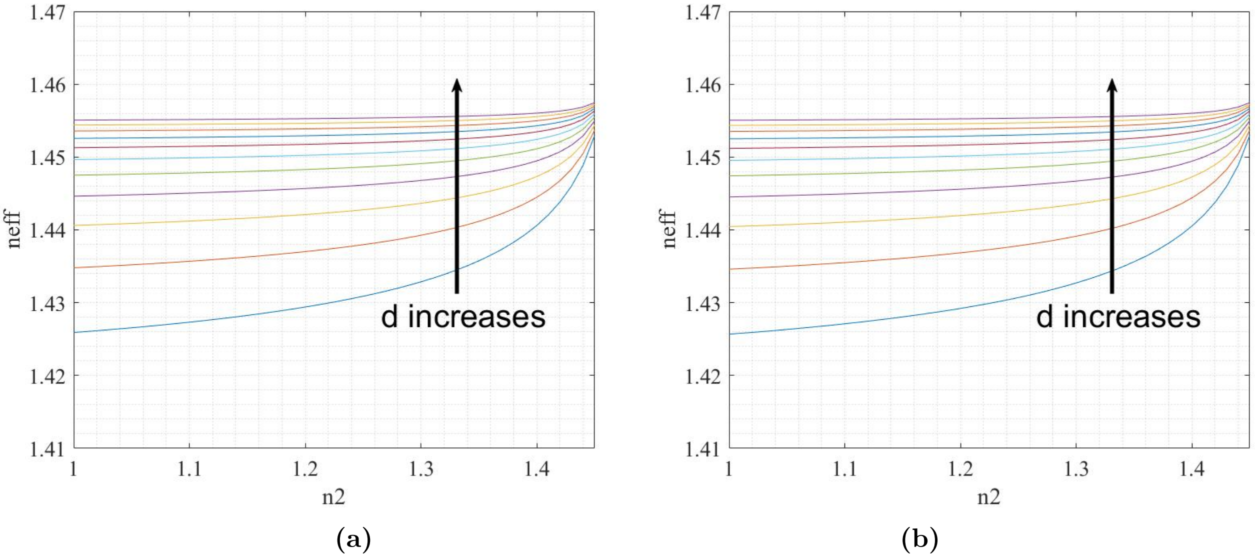

Figure 3.7: The plot of effective refractive index n_{eff} as a function of cladding index n_2 for different core thickness d from 2 μm to 10 μm calculated by (a) analytically solving the field equations and using (b) FIMMWAVE simulation (FEM solver).

3.5.1 Performance test with a planar Waveguide

It is helpful to start with a simple and well-known structure like a slab waveguide to test the performance of the software as well as to verify the feasibility of our design.

A planar waveguide was designed and Eq. (3.16) was used to calculate the effective refractive index. The effective refractive index was plotted as a function of the cladding index n_2 at different thicknesses d in order to qualitatively determine the effect of the evanescent fields on a slab waveguide. From Fig. 3.7a one can tell that the effective refractive index increases with the cladding index. The dependence is greater with a narrower core thickness. This is because a narrower core thickness allows deeper penetration of evanescence fields into the cladding. The same model is simulated with FIMMWAVE as well to be compared with the analytical solutions. By comparing results in Fig. 3.7b with Fig. 3.7a one is able to tell that the FIMMWAVE software has given reliable results for a simple structure like a slab waveguide.

In the next simulation, two 2-D planar waveguide models are considered. In one model, both the cladding and core are made of silica, while in the other, the cladding is composed of a material with a much higher thermo-optic coefficient, resulting in a different temperature dependence for the effective index of the first mode. The Bragg wavelength is calculated based on the effective index. The Bragg wavelengths for each model are calculated using both analytical and numerical (FEM) simulations. Note that the thermal expansion coefficient is not considered in this simulation to avoid confusion.

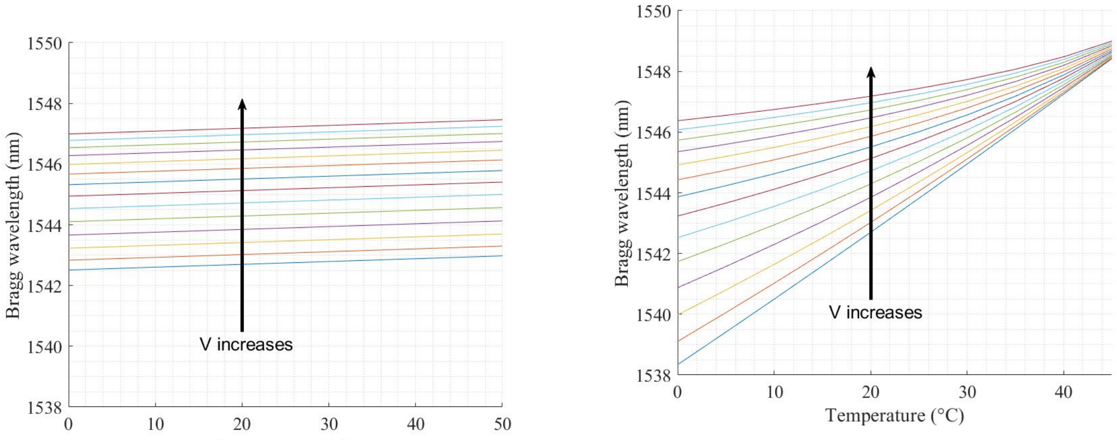

(a) Bragg wavelength of silica cladding

(b) Bragg wavelength of high thermo-optic cladding material

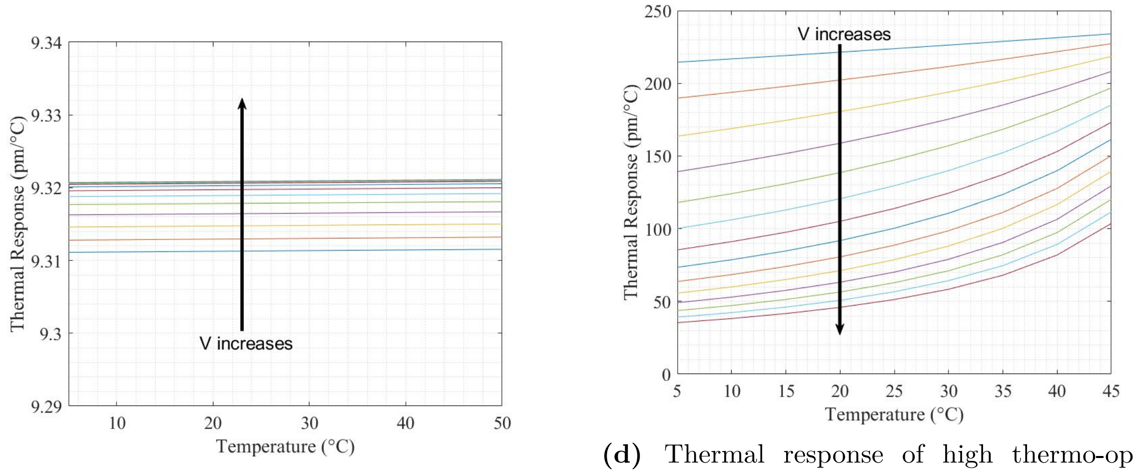

(c) Thermal response of silica cladding

(d) Thermal response of high thermo-optic cladding material

Figure 3.8: (a) and (b) Bragg wavelength in μm and (c) and (d) Thermal response in pm/ as a function of temperature for different values of the normalised frequency V parameter from 1 to 2.4 with silica cladding and cladding material with much higher thermo-optic coefficient, respectively.

The modelling results from Fig. 3.8a and Fig. 3.8b confirm that both simulation methods yield identical results for a simple structure, such as a planar waveguide. Additionally, it was concluded that the cladding material significantly affects the waveguide conditions, making this observation relevant for further work.

3.5.2 Performance test with cylindrical waveguide

The analytical results from Eq. (3.19) were compared with several solver options availiable in FIMMWAVE. The Finite Element Solver (FEM) is based on rectangular coordinates, which supports complex structures but the processing speed is slow for a cylindrical waveguide. The General Fibre Solver (GFS) is developed especially for solving for fibres with circular coordinates. The GFS with scalar option takes the same approximation as used in Eq. (3.19) and the GFS with vectorial option provides the most precise results.

The comparison is shown in Fig. 3.9. The software's GFS scalar option matches our analytical results with the same approximation. The FEM and GFS vectorial solvers agree with each other, indicating that FEM can also give high precision. Overall, despite the low processing speed, the FEM is the superior choice for its capability to handle complex structures and greater accuracy.

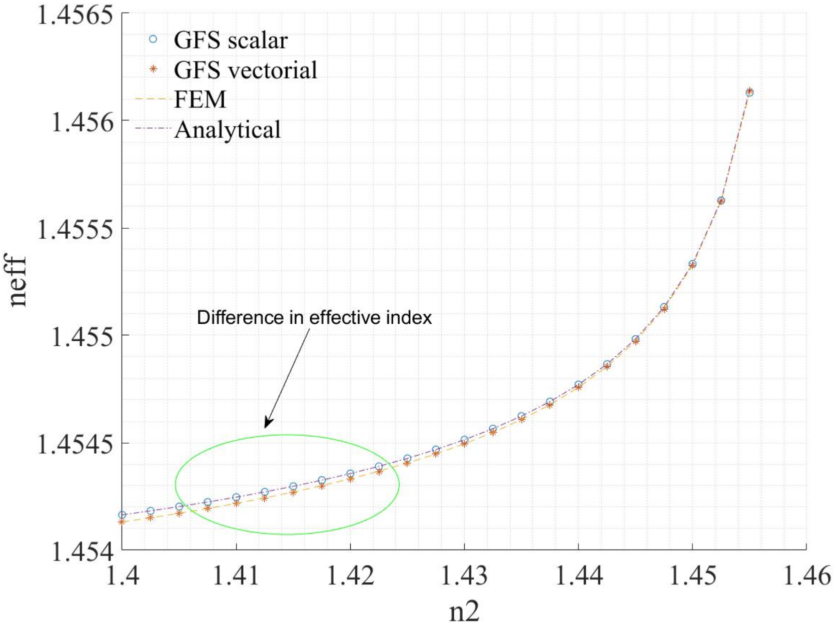

Figure 3.9: Comparison between analytical solution from Eq. (3.19), GFS scaler, GFS vectorial and FEM solver in FIMMWAVE.

3.6 Conclusion

In this chapter, different simulation techiniques are compared. Analytical waveguide theories and some simulation techniques to calculate the effective index have been introduced. Among them the FEM method was considered as the most suitable approach for its accuracy and ability to handle complex geometries. Meanwhile there are introductions on the FBG analysis by the coupled wave theory with a few examples. These allow the Bragg wavelength of the simulated devices to either be calculated by the coupled wave theory by the effective refractive index or by using the EME method directly. There are also comparisons between the analytical waveguide solutions and numerical simulations to verify the reliability of these simulation techniques.

4

Design of liquid-filled FBG temperature sensors

Contents

4.1 Introduction

In this chapter, we introduce a novel approach to differentiating between temperature and strain measurements. We have developed two types of devices to address this issue. First, we present an advanced FBG with significantly higher sensitivity compared to conventional FBGs. This enhanced sensitivity allows it to be used alongside a standard FBG, enabling independent measurements of strain and temperature. Second, we have engineered a temperature-insensitive FBG, designed specifically to measure strain without being affected by temperature variations.

The concept is based on creating microchannels in the cladding of an optical fibre and filling it with a liquid which has a dn/dT which has much higher magnitude and the opposite sign to silica. This has the effect of modifying the effective refractive index of the waveguide etc. Hence the temperature dependence of the FBG can be modified.

The FBG device configuration has several microchannels filled with liquid in the cladding adjacent to the core. The concept is shown in Fig. 4.1. The dimensions of the microchannels vary according to the design. There is a Bragg grating within the fibre core in order to obtain the desired temperature dependent properties. The microchannels run along the length of the fibre in proximity to the core where the grating is located. There are advantages to having microchannels in the cladding as it allows a weaker interaction with the optical mode, thereby allowing greater design flexibility and lower loss. The channels are brought out to the side of the fibre so that capillary filling of the liquid is possible. In this chapter there will be discussions on selection of the liquid, figures of merit and optimisation of designs to meet the requirements.

4.2 Initial investigations on waveguide geometries

In this section, I provide an introduction to my initial investigations on waveguide geometries. One aim of this work is to verify that the waveguide with microchannels in the evanescent field could affect the effective refractive index of the fibre. Another aim of this work is to find the consistency between different methods and make sure the simulations are reliable. For this reason these investigations are also known as stability tests.

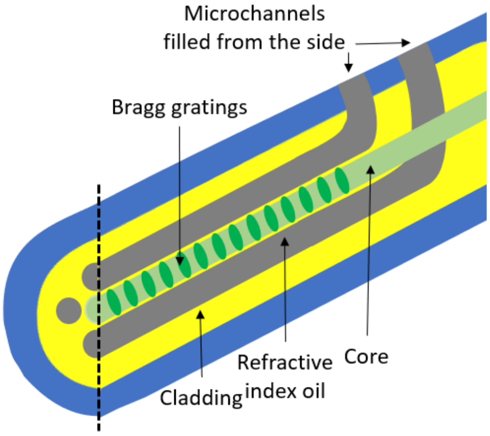

Figure 4.1: Device configuration (not to scale) in a section of fibre. The dimensions and shapes of the microchannels vary with different designs.

4.2.1 Waveguide with microchannels in evanescent field

It is not only the core but also the cladding that affects the effective refractive index of the fibre. It is not realistic to replace the whole fibre cladding with liquid, but micro-channels filled with liquid around the fibre core would be enough to improve the thermal response compared with a conventional silica FBG sensor. Thus micro-channels filled with fluid can be put in close contact with the core. In planar substrates, microfluidic channels in the evanescent field of Bragg gratings have been achieved with a femtosecond laser [89].

The layout of the micro-channels within the fibre is sketched in Fig. 4.2. In Fig. 4.2a a cylindrical waveguide with eight micro-channels is sketched. The optical mode overlaps regions with and without microchannels and results in an averaging effect of the refractive index. Thus it is possible to design a novel cylindrical waveguide that has an effective refractive index depending on the refractive index of the fluid and the contact area between the micro-channels and the core. Fibre Bragg grating sensors with a different temperature response and similar strain response are capable of discriminating temperature from strain. A device consisting of a conventional silica FBG sensor and a liquid-filled FBG sensor, can be used to measure strain and temperature independently. A change in strain causes the

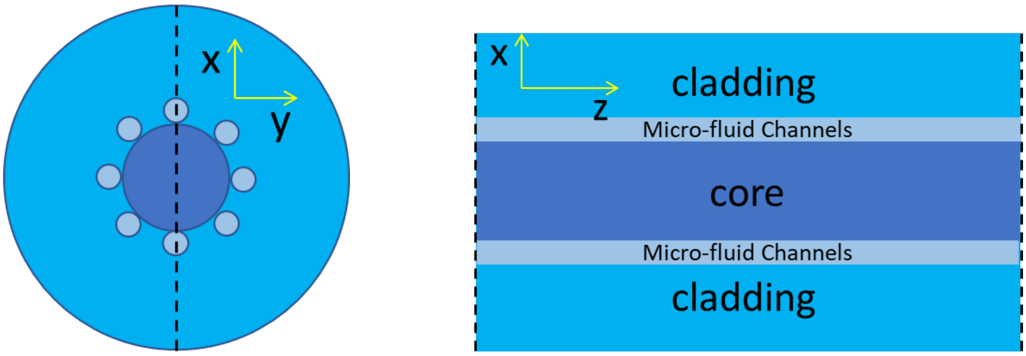

(a) Cylindrical waveguide with micro-channels **(b)** Cross-section view

Figure 4.2: (a) Sketch of Cylindrical Waveguide with micro-channels. (b) Cross-section view of (a) cut along the dashed line.

two wavelength peaks to move together, while a change in temperature causes the separation between the peaks to change.

4.2.2 Interaction with the micro-channels

Simulations were carried out in order to verify the effects of micro-channels in the evanescent field. Three models are designed and simulated. Model A is as a simple step-index waveguide for reference. Model B has twelve micro-channels that have the dimensions shown in Fig. 4.2(a) but the micro-channels have a refractive index which is constant and the same as the cladding. The effective refractive index as a function of cladding refractive index is plotted for model A and model B in Fig. 4.3(a). Model C has microchannels with dimensions shown in Fig. 4.2(a) filled with a material of varying refractive index. In model C instead of varying cladding index, the channel index is varied. Figure 4.3(b) shows how the effective refractive index varies with channel refractive index in Model C.

Comparison of models A and B in Fig. 4.3 shows that the software can solve complex structures similarly (although the processing time is almost doubled). There is near identical agreement with the solution of a standard step-index profile when the microchannels has the same refractive index as the cladding. This gives confidence the model has been set up correctly. Comparison between model A and model C demonstrates that modifications to the micro-channels are able to affect the refractive index. Although the response is only about one-third of that of the whole cladding.

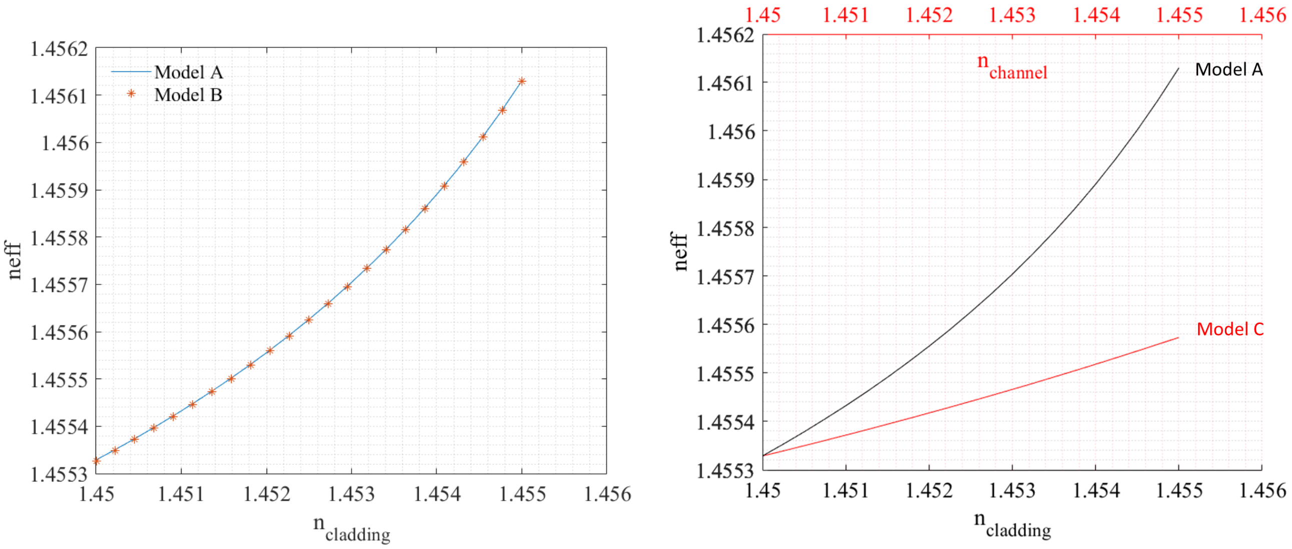

(a) Comparison between two identical models one of which has invisible channels

(b) Comparison between effects of cladding index and channel indices on the effective refractive index.

Figure 4.3: Comparison between the three models. A: step-index waveguide without micro-channels. B: step-index waveguide with micro-channels that always has the same refractive index as the cladding. C: step-index waveguide with micro-channels with fixed cladding refractive index but varying channel index. Plot of effective refractive index comparing (a) models A and B to show that the software can deal with complex geometries. (b) models A and C to show that the channel refractive index has an effect on the effective refractive index.

4.2.3 Number of microchannels

In the initial stage of the design a positive thermo-optic coefficient material was considered to be filled in the micro-channels. The effective index of the waveguide was calculated by a 2-D FEM solver and the Bragg wavelength was calculated accordingly.

The simulation started with twelve micro-channels and managed to achieve convergence for two limiting cases. When the number of micro-channels is zero the model should be identical to a conventional silica waveguide. Alternatively, when the number of micro-channels is large the structure converges to a 'band'

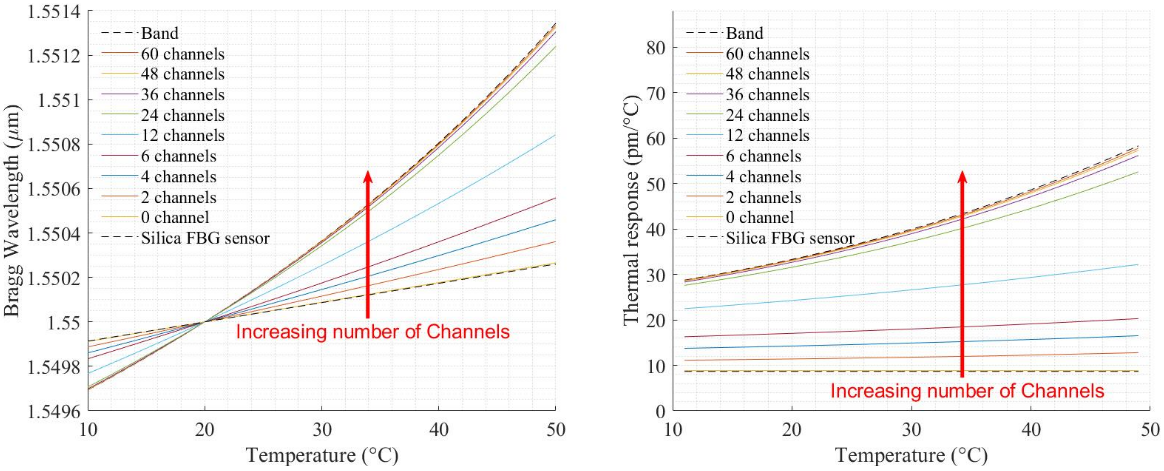

(a) Bragg wavelength for different number of micro-channels

(b) Thermal response for different number of micro-channels

Figure 4.4: Convergence test varying the number of micro-channels comparing (a) Bragg wavelength and (b) Thermal response. As the number of micro-channels increases, the sensor is eventually equivalent to an FBG sensor with a micro-channel 'band'. As the micro-channels vanish the sensor gives the same response as a conventional silica FBG sensor.

around the core. Clearly, from Fig. 4.4 the convergence has been achieved for both the upper and lower limits in terms of the number of micro-channels. Also, the model with twelve micro-channels has a higher and non-linear thermal response compared with a conventional FBG sensor [16] plotted on the graph. All models are normalised at 20°C when the core index = 1.458, cladding index = 1.455, Channel index = 1.450453 (with a much higher thermo-optic coefficient), Core radius = 4.1 μm, channel radius = 1 μm, $V = 1.8947$, and $\lambda_B = 1.55$ μm. The cladding radius is sufficiently large that there is negligable modal power at the extremity.

The simulations did not result in a practical design because the material assumed in the micro-channel region was not available. Meanwhile, the micro-channels had dimensions which were too small to be practical. However, it is undeniable that this initial work has provided a very solid foundation for future designs.

4.2.4 Consistency with 3-D simulation

The same model can also be simulated in 3-D so that the whole spectrum of transmission can be plotted against wavelength.

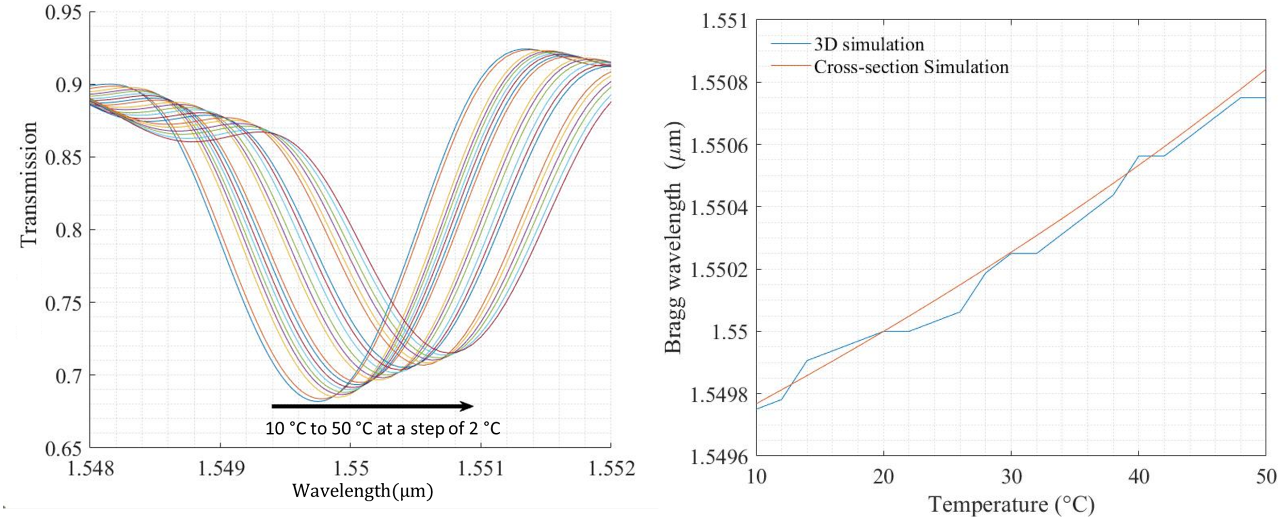

(a) Transmission Spectrum

(b) Comparison of 2-D and 3-D simulation results of the same model

Figure 4.5: Simulation of an FBG sensor with 12 channels filled with liquid (a) Transmission Spectrum calculated by 3-D simulation. (b) Bragg wavelength as a function of temperature comparing 2-D (red solid line) and 3-D (blue solid line) simulations.

The sensor with the 12 micro-channels in the previous section was simulated and some additional parameters at 20°C are: Pitch = 0.5322 μm, length of the grating $L_g = 0.5322$ mm, and $\delta n = 0.001$.

In Fig. 4.5a the transmission intensity was plotted as a function of wavelength. The shape of the transmission curve matches the Bragg grating transmission with a short L_g. The transmission spectrum shows the increase in Bragg wavelength due to an increase in temperature. The wavelength where minimum transmission occurs (assumed to be the Bragg wavelength) for each temperature was then extracted and plotted against temperature. In Fig. 4.5b the results obtained from the 3-D simulation are compared with the previous 2-D simulation. Generally, the 3-D simulation results agree with the cross-section simulation. The accuracy could be improved at a cost of processing time by increasing the number of modes. Although only the fundamental mode is useful, the FEM solver of software tends to give a better result with more modes involved. The convergence of accuracy is achieved at above 60 modes and only 32 are calculated in this simulation to save time.

4.3 Figures of merit

Before moving on to the actual design parameters, it is necessary to understand what is needed in a practical device. The most important feature that makes these devices different is their radically different temperature sensitivities compared to a conventional FBG. It is important to understand the temperature range over which the desired temperature sensitivity is achieved. Other features including loss and reflectivity revealed in reflection and transmission spectrum should also be considered. And finally, all the components made up of the device shall be sourced commercially.

Sensitivity

One of the most significant features is the temperature sensitivity of the devices. There are two extreme cases that are interesting: One is as high a sensitivity as possible and the other is as low as possible. The former would enable applications such as temperature and strain discrimination when used in combination with a conventional FBG and the latter would be used on its own as a temperature-independent sensor for other physical parameters.

Working temperature range

The working temperature range here is defined as the variation of temperature where a claimed sensitivity is achieved. Ideally, the working temperature range is as large as possible. However, it was heavily restricted by practical constraints. Therefore, the aim is that the design should be able to tune the working temperature range according to requirements.

FBG spectrum

It is also important that the FBG transmission and reflection spectrum are suitable for potential applications. This could be discussed in several aspects. Firstly, the loss of the device should be minimised, which includes the modal loss and the absorption loss. This device should be robust to noise and bending losses. Secondly, the reflectivity of the FBG should not vary with temperature. For sensing applications, the bandwidth of FBG should be as small as possible for high sensitivity.

Availablity of materials

Last but not least, all the components made up of the device should be available. These will include the liquid and the fibre types that has been chosen. The fibre used in the design was a standard single mode fibre, and the liquid will be commercially available as will be discussed in the following section.

4.4 Choice of liquid

In order to design such micro-structured devices, it is essential to consider the type of liquid to be filled into the micro-channels. Generally, the refractive index of the liquid must be close to the fibre cladding index to reduce the modal loss of the waveguide. In order to achieve novel temperature sensitivity the liquid shall also have a different thermo-optic coefficient $\frac{dn}{dT}$ compared with optical fibre made of fused silica, which is about $7.94 \times 10^{-6}{}^{\circ}\mathrm{C}^{-1}$. In the following subsections, all refractive indices and thermo-optic coefficients mentioned are for a wavelength of 1550 nm at 25°C.

Alcohol

Photonic crystal fibre (PCF) filled with optical grade ethanol [50] and methanol [46] has been reported previously. Ethanol and methanol have refractive indices of 1.3519 [90] and 1.3172 [91], respectively. Their thermo-optic coefficients are both around $-394 \times 10^{-6}{}^{\circ}\mathrm{C}^{-1}$ [92] providing a large parameter space. However, their refractive indices are very different to silica, making their incorporation into waveguides problematic. Furthermore, both of them are highly flammable and volatile at room temperature making the potential devices unstable for long term use. Therefore, either methanol or ethanol is not an optimal choice.

Glycerol

Glycerol, on the other hand, is quite stable at room temperature and non-flammable. The refractive indices and thermo-optic coefficients are 1.4473 and $-225 \times 10^{-6}°\mathrm{C}^{-1}$ [93] so very well matched to silica. Furthermore, glycerol is soluble in water, which enables easy realisation of glycerol-water mixtures that have controlled refractive indices. Due to the advantages glycerol solution was the first selection for the initial stage of investigations. But as the work further progressed, it was found that the absorption of glycerol solution at 1550 nm was far too high [94], causing a high loss in the devices fabricated. A similar concern was also observed by previous research with cladding etched fibre immersed in glycerol solution [95]. Therefore, although the achievement of glycerol-filled devices has been revealed both numerically and experimentally, glycerol solution was not chosen for the final designs.

Refractive index liquid

The success of glycerol-filled devices was encouraging, so a strategy was to look for a liquid similar to glycerol but with lower absorption. Refractive index liquids from Cargille Labs were selected for a much lower absorption and much higher magnitude thermo-optic coefficient of $\frac{dn}{dT} = -395 \times 10^{-6}°\mathrm{C}^{-1}$ [96]. Although the refractive index liquid is not soluble in common inorganic solvents such as water, a set of liquids with refractive indices varying between 1.420 to 1.460 at 1550 nm in 0.002 increments, is available to closely matching that of silica (1.444) [96]. This set of refractive index liquids became the optimal choice for the above reasons.

Polymerisable waveguide resin

A concern was the mechanical strength of the fibre. Replacing part of the glass with liquid will restrict the device's capability for measuring physical properties such as strain. As a result, a polymerisable resin has become the next choice. For example, the waveguide resins provided by ChemOptics have a thermo-optic coefficient of $\frac{dn}{dT} = -180 \times 10^{-6}°\mathrm{C}^{-1}$ and refractive indices selectable from 1.430 to 1.460. By using polymers instead of liquid the mechanical strength would be improved. Furthermore, as they do not mix with poly-acrylate polymers, this would enable the use of re-coating which would further improve the mechanical strength.

4.5 Waveguide and FBG parameters

In this section, a demonstration will be provided on how the final designs were developed by investigating which parameters are essential, which are not, and how they can be utilised. Parameters that remain constant are primarily related to fibre materials, including core index, cladding index, and their thermal and elastic properties. Meanwhile, there are sufficient degrees of freedom to explore the parameter space.

Microchannel size

The microchannel size is an adjustable parameter for controlling the effective refractive index of the waveguide. A simple test is having the core surrounded by 'a band' of microchannel filled with material of different refractive index. The simulation results are presented in Fig. 4.6. It can be seen that not only the Bragg wavelength but also the reflectivity have changed with different band radius. Thus, this should be taken into consideration for future designs.

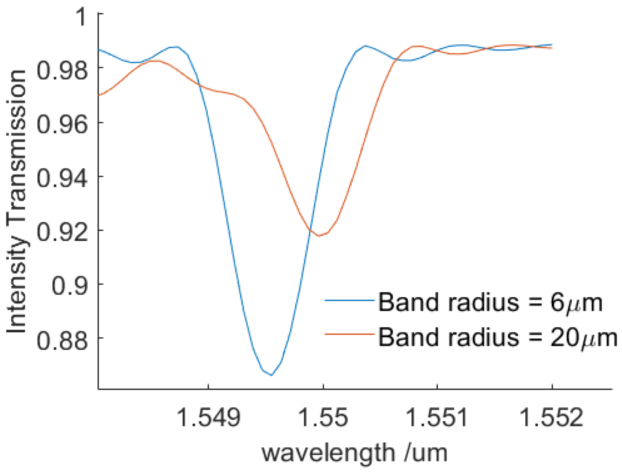

Figure 4.6: Plot of intensity transmission of FBGs with a core surrounded by microchannel 'bands' of 6 μm and 20 μm radius.

FBG length

An investigation was carried out to determine the optimum FBG length. This time the aim was to identify how the FBG conditions would have impact on the designs. Again, the band structure was used and for each FBG length a full spectrum at a range of temperature points are plotted in Fig. 4.7. For FBG devices with identical structure and identical temperature, the Bragg wavelength is unchanged. However, the reflectivity has varied according to the FBG length. These simulation results are comparable with the previous analytical calculations for FBGs. By increasing the FBG length, the reflectivity can be moved closer to the asymptotic value of the $\tanh^2(\kappa L)$ reflectivity, thereby reducing the reflectivity's dependence on temperature.

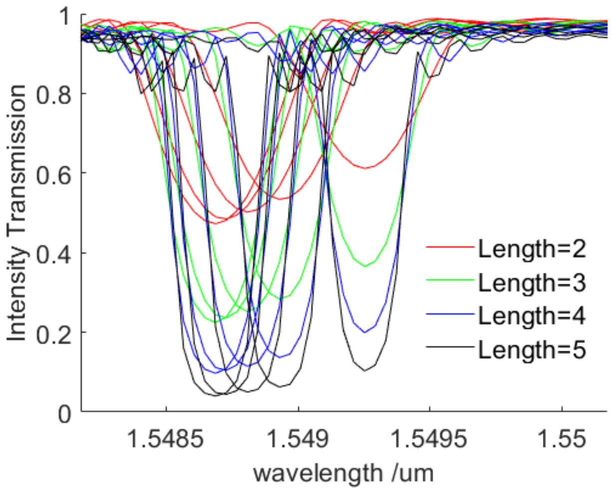

Figure 4.7: Plot of intensity transmission of FBGs with identical microchannels and different FBG lengths, for a range of temperatures of 10 to 50°C at a step of 10°C from the right to the left of the plot.

Polarisation dependence

It is also interesting to find out if the devices are polarisation dependent. In order to find this, a so-called 'kidney' shaped FBG device is designed as shown in Fig. 4.8. The idea is to make the cross section as asymmetric as possible to allow some discrimination between different angles of linear polarisation. If this is achieved it would open up a great potential on polarisation based sensors of different physical parameters. The simulated transmission spectra at different temperatures are plotted in Fig. 4.9. The spectra for different polarisations are nearly identical at a given temperature. Although the waveguide is deliberately designed as asymmetric as possible, the polarisation dependence was still negligible. The conclusion on one hand was negative as the polarisation dependent sensor was not possible to be fabricated. However, on the other hand, polarisation independence is very important for many applications.

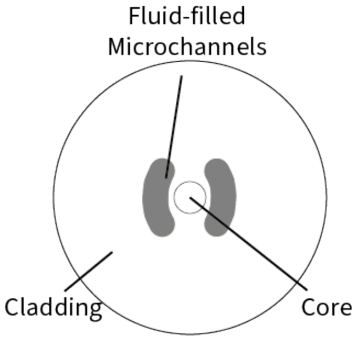

Figure 4.8: The geometry of the asymmetrical FBG devices designed to achieve discrimination with different incident polarisations. The 'kidneys' are filled with liquid materials.

4.6 Design graph

This section introduces some design graphs that will directly guide the fabrication process. After establishing a solid understanding with a number of simulations, it is now possible to identify how the temperature sensitivity is controlled with our selected refractive index liquids. With either a double cladding waveguide or a bow-tie shaped waveguide as shown in Fig. 4.10, the factors affecting the temperature sensitivity can now be simplified to two factors: i) The percentage area of liquid in the evanescent field that the liquid is filled; and ii) The actual refractive index of the liquid. Simplistically, we can consider the cladding to have an average cladding index that lies somewhere between the refractive index of the cladding n_{cl}, and the liquid, n_{liq}, depending on the size of the microchannels and their proximity to the core. As the temperature increases, the refractive index of the core, n_{co} and the cladding

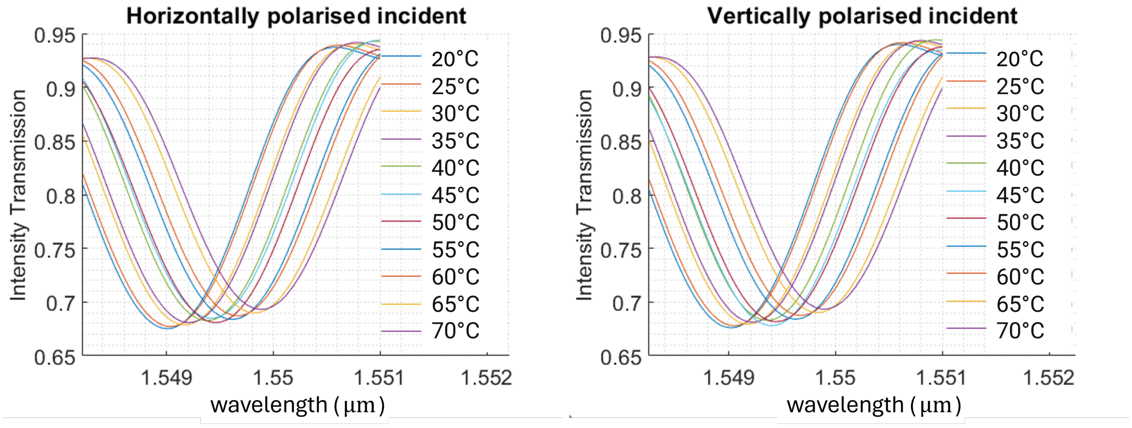

(a) Horizontal polarisation **(b)** Vertical polarisation

Figure 4.9: Simulation of an asymmetric kidney shaped FBG device at different temperatures with (a) horizontal and (b) vertical polarised incident light.

material, n_{cl} both increase, while the refractive index of the liquid, n_{liq}, decreases. By engineering the waveguide design appropriately we can adjust $\frac{dn_{eff}}{dT}$. In this work, we use two independent variables to achieve this: The refractive index liquid proportion in the cladding and the liquid refractive index at room temperature.

4.6.1 Double cladding waveguide analysis

It appears too difficult to analytically solve for the waveguide solution with microchannels of arbitrary shapes. A simplified model is therefore used for analysis. The analysis of the devices in this work use the approximation that the microchannels around the core can be represented as a continuous band of material, forming an inner cladding with index, n_{inner}, which is between n_{liq} and n_{cl}, depending on the microchannel size. This approximation allows us to use the solution for a depressed cladding waveguide [81][82]. Although this solution was for waveguides where the inner cladding has a lower refractive index than the outer material, it also holds true for cases where the inner cladding has a higher refractive index. The propagation constant β of a single-mode double-clad waveguide can be found by the following

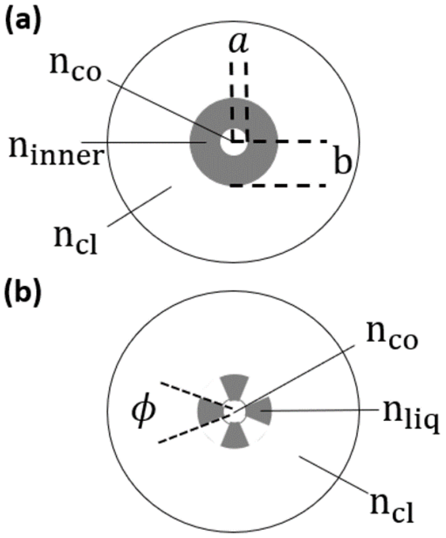

Figure 4.10: Models of the FBG for the (a) analytic model and (b) numerical simulation. The refractive index variables are indicated as follows: n_{co} = core, n_{cl} = cladding, n_{liq} = liquid, n_{inner} = inner cladding (approximating liquid microchannels within the silica). The core has radius a and the inner cladding has radius b. The proportion of liquid is varied by varying n_{inner} in the analytic model and by varying the sector angle ϕ in the numerical model.

equation[82], that has previously been presented in Chapter 2:

$$\begin{aligned}&[\gamma J_0(\kappa a)I_1(\gamma a)+\kappa J_1(\kappa a)I_0(\gamma a)]\\ &\times[\delta K_0(\gamma b)K_1(\delta b)-\gamma K_1(\gamma b)K_0(\delta b)]\\ &+[\gamma J_0(\kappa a)K_1(\gamma a)-\kappa J_1(\kappa a)K_0(\gamma a)]\\ &\times[\delta I_0(\gamma b)K_1(\delta b)+\gamma I_1(\gamma b)K_0(\delta b)]=0\end{aligned} \tag{4.1}$$

where K_ν, J_ν, and I_ν are the modified Hankel, Bessel, and modified Bessel functions of order ν, respectively, where a is the radius of the core and b is the radius of the inner cladding. The outer cladding is assumed to have an infinite radius. The terms in Eq. (4.1) are defined for our case in Fig. 4.10(a) as:

$$\begin{aligned}\kappa &= \sqrt{n_{cl}^2(1+\Delta)^2k^2-\beta^2}\\ \gamma &= \sqrt{\beta^2-n_{cl}^2(1+\Delta')^2k^2}\\ \delta &= \sqrt{\beta^2-n_{cl}^2\kappa^2}\\ \Delta &= (n_{co}-n_{cl})/n_{cl}\\ \Delta' &= (n_{inner}-n_{cl})/n_{cl}\end{aligned} \tag{4.2}$$

where n_{co}, n_{inner} and n_{cl} are refractive indices of the fibre core, inner cladding, and outer cladding, respectively, β is the propagation constant and k is the wavenumber. By solving Eq. (4.1) numerically the effective refractive index, n_{eff} is obtained, using $n_{eff} = \frac{\beta}{k}$.

The Bragg wavelength can then be estimated, since the pitch of the grating is known. The inner cladding to be the weighted average of the silica and liquid refractive indices according to a percentage contribution from the liquid. The full parameter space was analysed with different liquid proportions and refractive indices. Design graphs are plotted in Fig. 4.11. A general trend is that at lower temperatures the temperature sensitivity is negative with a positive change in sensitivity with increasing temperature. We can quantitatively analyse the effects

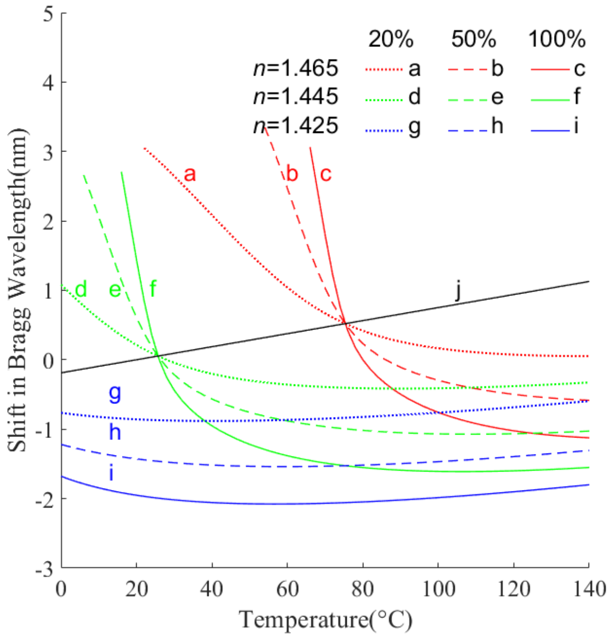

Figure 4.11: Analysis of parameters that affect the Bragg wavelength of the FBG (a)-(i) with microchannels filled by liquid with different refractive indices and proportion of liquid in the inner cladding, (j) with the inner cladding refractive index equal to that of the outer cladding.

of the two independent variables on the Bragg wavelength. Varying the liquid refractive index causes a horizontal translation of the plot and can be used to control the working temperature of the device. In contrast, varying the proportion of the liquid causes a tilting of the plot, thus determining the thermal sensitivity. This important analysis provides the information for designing a device with the desired temperature sensitivity and working temperature range.

To summarise, a liquid proportion is selected first to meet the requirement of the temperature sensitivity of the devices. Generally, a lower liquid proportion results in a more positive thermal response, and a larger liquid proportion results in a more negative thermal response. Then, the refractive index of the liquid is tuned to set the operating temperature.

In order to achieve optimized parameters for specific designs more accurate numerical simulations of the fibre were performed, based on the model in Fig. 4.10(b). The microchannels were modelled as four individual sectors of a circle, but not including the core (with a small margin around the core). This enables the liquid proportion to be varied by varying the sector angles. The FIMMWAVE (Photon Design Limited) mode solver software was employed. The fibre used in the simulation was SMF28e+ with a core diameter of 8.2 μm and a cladding diameter of 125 μm [97]. The core index, n_{co}, and the cladding index, n_{cl}, of the fibre are 1.451 and 1.445, respectively [98]. The radial length of each microchannel is 10 μm, and the axial length of the FBG and the microchannels is 6 mm. The pitches were slightly tuned so that all Bragg wavelengths were not far from 1550 nm.

Simulation results for the change in Bragg wavelength with temperature at 1550 nm are shown in Fig. 4.12. Figure 4.12(a) shows curves for a liquid refractive index of 1.43 for different proportions of liquid between 0 to 100%. Figure 4.12 (b) shows curves for a 100% liquid proportion, for liquid refractive indices between 1.42 and 1.44. The shifts in Bragg wavelength are plotted against temperature with different liquid proportions and liquid refractive indices in Fig. 4.12 (a) and (b), respectively.

A general trend is as follows: When the temperature increases, the thermal response of the Bragg wavelength increases (more positive). This is because when n_{liq} is further away from n_{co} the impact of liquid cladding is less significant than that of silica cladding. Eventually, at a higher temperature, the devices have a positive thermal response since the silica cladding dominates in the cladding region.

In contrast, at a lower temperature where the liquid refractive index is higher, the liquid cladding dominates and the thermal response is therefore negative.

A similar trend is seen from the liquid refractive index as shown in Fig. 4.12 (b) where the thermal response is more negative with a higher liquid refractive index (closer to the core index) and more positive with a lower liquid refractive index (further away from the core index). A different liquid proportion not only shifts the thermal response but also changes the range of the operating temperature. One extreme case is when the liquid proportion equals 100% where the device has a cladding made of liquid with the corresponding refractive index. In this case, the variation in thermal response due to temperature is high and can be approximated by a quadratic function. When the liquid proportion is zero the device is a conventional FBG with a constant thermal response. Therefore, by varying the liquid proportion between the two extreme cases, we can set the required thermal sensitivity. Then by appropriate choice of liquid refractive index, we can shift the operating temperature window to match the required application.

The strategy of designing such a device is therefore important and here a general method to follow is demonstrated. A liquid proportion is selected first to meet the requirement of the temperature sensitivity of the devices. Generally, a lower liquid proportion results in a more positive thermal response, and a larger liquid proportion results in a more negative thermal response. Then the refractive index of the liquid is tuned to set the operating temperature.

4.6.2 Bow-tie shaped waveguide simulation

The double cladding waveguide has shown the possibility of designing novel FBG sensors. However, there are some limitations associated with this tool. The most significant limitation is that an averaging approximation was applied which enables the trends to be shown, but which is not sufficiently accurate for a final design. In order to achieve optimized parameters for specific designs, more accurate numerical simulations of the fibre were performed, based on the model in Fig. 4.10(b).

The microchannels were modeled as four individual sectors of a circle, but not including the core (with a small margin around the core). This enables the liquid proportion to be varied by varying the sector angles. By sweeping over a range of values for the two parameters the waveguide can be treated equivalent to a bow-tie shaped waveguide where the percentage of liquid can be controlled by the angle of the bow-tie. The FIMMWAVE (Photon Design Limited) mode solver software was again employed. The fibre used in the simulation was SMF28e+ with a core diameter of 8.2 μm and a cladding diameter of 125 μm[97]. A convergence test was undertaken to determine the optimum cladding boundary to be 50 μm to speed up the simulation. The core index, n_{co}, and the cladding index, n_{cl}, of the fibre are 1.451 and 1.445, respectively [98]. The radial length of each microchannel was 10 μm, and the axial length of the FBG and the microchannels was 6 mm. The pitches were slightly tuned so that all Bragg wavelengths were not far from 1550 nm. Simulation results for the change in Bragg wavelength with temperature at 1550 nm are shown in Fig. 4.12, curves for a liquid refractive index of 1.43 for different proportions of liquid between 0 to 100% are shown in Fig. 4.12(a): Curves for a 100% liquid proportion, for liquid refractive indices between 1.42 and 1.44 are shown in Fig. 4.12(b). The shifts in Bragg wavelength are plotted against temperature with different liquid proportions and liquid refractive indices.

A general trend is as follows: At a lower temperature where the liquid refractive index is higher, the liquid cladding dominates and the thermal response is therefore negative. A similar trend is seen from the liquid refractive index as shown in Fig. 4.12(b) where the thermal response is more negative with a higher liquid refractive index (closer to the core index) and more positive with a lower liquid refractive index (further away from the core index).

In contrast, when the temperature increases, the thermal response of the Bragg wavelength increases (more positive). This is because when n_{liq} is further away from n_{co} the impact of liquid cladding is less significant than that of silica cladding. Eventually, at a higher temperature, the devices have a positive thermal response since the silica cladding dominates in the cladding region.

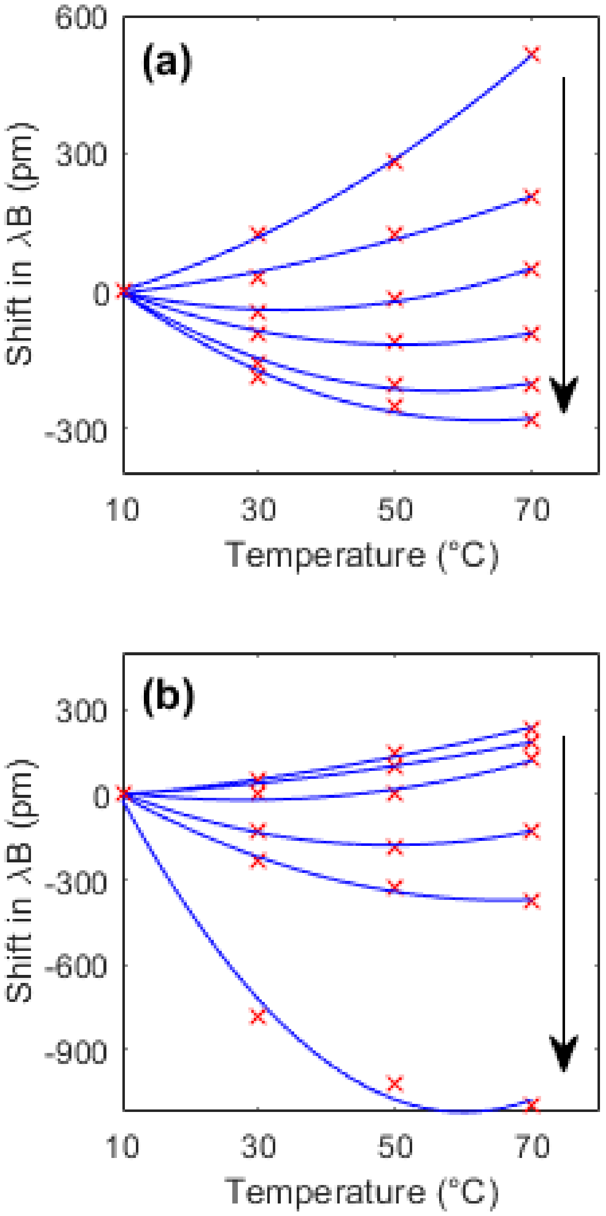

Figure 4.12: Simulation of the shift in Bragg wavelength against temperature with (a) liquid proportion from 1% (nearly purely silica cladding) to 100% (purely liquid cladding) along the black arrow, with liquid refractive index of 1.43 at 1550 nm and (b) liquid refractive index from 1.42 to 1.44 at 1550 nm along the black arrow, with a liquid proportion of 100%. The raw data labeled with red X's are fit with second-order polynomials plotted with the solid blue lines.

A different liquid proportion not only shifts the thermal response but also changes the range of the operating temperature. One extreme case is when the liquid proportion equals 100% where the device has a cladding made of liquid with the corresponding refractive index. In this case, the variation in thermal response due to temperature is high and can be approximated by a quadratic function. When the liquid proportion is zero the device is a conventional FBG with a constant thermal response. Therefore, by varying the liquid proportion between the two extreme cases, the required thermal sensitivity can be found. Then, an appropriate choice of liquid refractive index can shift the operating temperature window to match the required.

4.6.3 Comparing double cladding with bow-tie

There are now two tools for exploring the characteristics of FBG designs with novel temperature sensitivities. It is important to find the consistency between the two methods. Since the double cladding waveguide is a special shape of the bow-tie waveguide it is believed that the simulation method should give identical analysis when the liquid proportion is 100%. Hence, it is possible to compare the two tools in this specific case. The first work was to emulate the results in Fig. 4.12 (b) with the double cladding analysis method. Figure 4.13 shows a comparison of the double cladding approximation with simulation results of a bow-tie using FIMMWAVE Photon Design Ltd. It is clear in the plot that the double cladding approximation shows great consistency when there is a full band of liquid region at different refractive indices and temperatures.

It is useful to determine the effect of different microchannel cross-sections. Although the double cladding approximation cannot solve for bow-tie shaped waveguides with different sector angles directly, it is still possible to vary the shape of the double cladding waveguide by changing the radius of the liquid control region. Figure 4.14 shows simulations of the double cladding approximation and the simulation results as the radius is varied. Similarly, this plot shows consistency between the analytical solution and the simulation results. Varying the outer radius of the liquid control region does provide a new degree of freedom to design the sensors. The model is quite sensitive to radius but in reality the radius of the micro-channels is often not well controlled. This means the random error caused

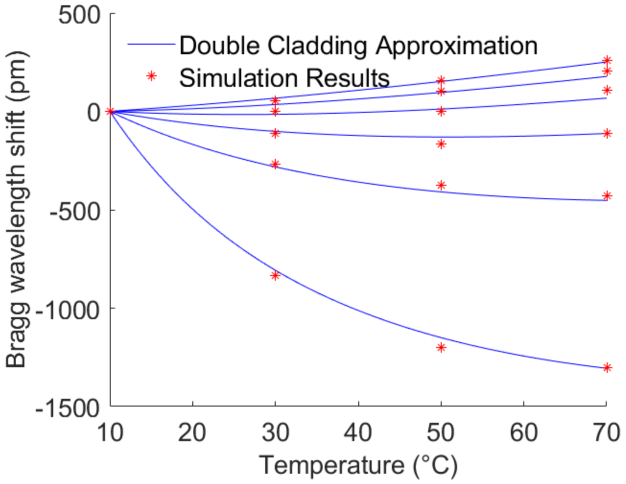

Figure 4.13: Shift in Bragg wavelength as a function of temperature for a full band of liquid obtained using the double-cladding approximation (solid blue lines) and simulations of a double cladding configuration using FIMMWAVE (red stars). The raw data labeled with red stars are simulation of the shift in Bragg wavelength against temperature with a liquid refractive index from 1.42 (top) to 1.44 (bottom) at 1550 nm, with a liquid proportion of 100%. The solid blue line plots the analytical double-cladding waveguide of the shape.

by the fabrication process is well above the design tolerance of the radius. The situation is worse when the radius is close to the core radius, but as the radius goes above two times the core radius further variation would not cause a significant difference. So, in practise, the best strategy is to make the radius at its saturation position and vary the sector angle of the band.

Although the double cladding approximation cannot give an exact calculation of the bow-tie waveguide, it is interesting to note that varying the outer radius has a similar effect to varying the sector angle. So, emulation of the results in Fig. 4.12 (a) can still be made by comparison with the analytical results provided in Fig. 4.14. The comparison is plotted in Fig. 4.15. An interesting phenomenon noticed was that although different area-related parameters are varied with different methods, similar curves were obtained. An explanation is that it is the microchannel area that determines the performance of the FBG sensor, and both sector angle and radius appeared to be a factor of that area. These results have essentially shown that the designs are shape independent. A more rigorous explanation will be introduced later in the next section when considering the filling factors.

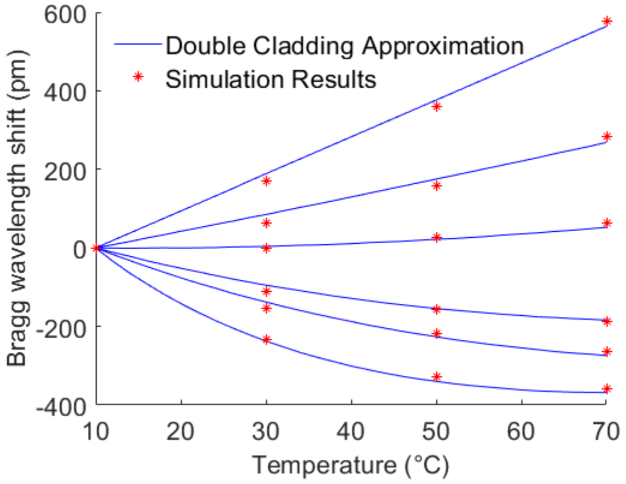

Figure 4.14: Simulation of the shift in Bragg wavelength against temperature with liquid region radius varying from 4 μm (top) to 12 μm (bottom), with liquid refractive index of 1.43 at 1550 nm. The solid blue line plots the analytical double-cladding waveguide of the shapes of various outer radius. The red stars represents the results from simulations of a double cladding configuration using FIMMWAVE.

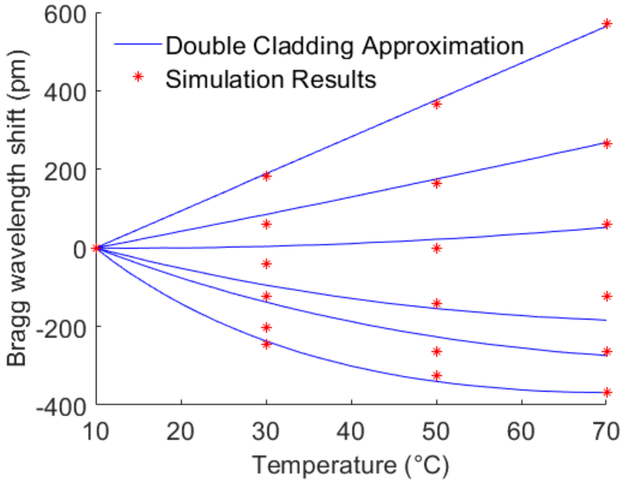

Figure 4.15: The solid blue line plots the shift in Bragg wavelength against temperature for the double-cladding waveguide calculated from the analytical model, with shapes of various outer radius, varying from 4 μm (top) to 12 μm (bottom), with liquid refractive index of 1.43 at 1550 nm. The stars are simulation results of the bow-ties shaped waveguide by varying the microchannel sector angles. The radius is tuned so that the two curves are best fit.

4.7 Optimization of temperature insensitive FBG devices

The analysis and simulation from the work above has shown the possibility of making temperature-insensitive FBG devices, which are of significant interest for many applications, such as optical filters, laser stabilization, fibre lasers, add-drop multiplexers, wind turbines, space and aerospace. The above work also indicates that it is easier to fabricate a high temperature sensitivity device because this only requires maximizing the liquid proportion around the fibre core and minimizing the difference in refractive indices between the liquid material and the core. Fabricating a temperature-insensitive device, on the other hand, is more sensitive to the geometry. The initial approach was to try to experimentally fabricate microchannels that occupy the same area indicated by the simulation (these results are presented in Chapter 7). After several iterations a device close enough was realised. Then the liquid refractive indices were tuned slightly to make the zero sensitivity point at the required temperature range. However, this method was really time consuming and has restricted further development of different geometry designs. An interesting analytical method was introduced by Dr. Frank Payne, which has dramatically simplified the problem. In the following section, it will be demonstrated how this method reaches an analytical approach to optimise the temperature insensitive design, together with some simulation work.

4.7.1 Find when the temperature sensitivity is zero

In order to find the turning point where the temperature sensitivity crosses zero, the thermal expansion can be ignored for now and the aim is to find the condition when $\frac{d_{neff}}{dT} = 0$, where n_{eff} is the effective index of the propagation mode. The derivations start by considering the problem for a step-index optical fibre, then the problem is generalised to arbitrary shaped fibre waveguides.

(a) (b)

Figure 4.16: (a) Step-index Optical fibre cross sections with core radius a; (b) General Optical fibre with arbitrary geometries as temperature control region

Step index optical fibres

The analysis starts from the simplest step-index optical fibres as shown in Fig. 4.16(a), where one could calculate n_{eff} and $\frac{d_{neff}}{dT}$ directly to find the conditions for the turning points. In this, and the following calculations, all the waveguides are assumed to be weakly guided. The waveguide modal parameters are:

$$u = a\sqrt{n_1^2k^2 - \beta^2} \tag{4.3}$$

$$w = a\sqrt{\beta^2 - n_2^2k^2} \tag{4.4}$$

$$V^2 = u^2 + w^2 = a^2k^2(n_1^2 - n_2^2) \tag{4.5}$$

where a is the radius of fibre core, n_1 and n_2 are core and cladding refractive indices, respectively, k is the free space wave number $k = 2\pi/\lambda$ and β is the propagation constant defined as: $\beta = n_{eff}k$. The eigenvalue equation for the fundamental LP_{01} mode is given by:

$$\frac{uJ_1(u)}{J_0(u)} = \frac{wK_1(w)}{K_0(w)} \tag{4.6}$$

where J_i is a Bessel function and K_i is a modified Hankel function of i^{th} order. The effective refractive index n_{eff} can be expressed in terms of the above parameters:

$$n_{eff}^2 = n_1^2 - \frac{u^2}{V^2}(n_1^2 - n_2^2) \tag{4.7}$$

Both sides of Eq. (4.7) are differentiated with respect to temperature T:

$$\frac{dn_{eff}^2}{dT} = \frac{dn_1^2}{dT}(1 - \frac{u^2}{V^2}) + \frac{u^2}{V^2}\frac{dn_2^2}{dT} - \frac{1}{2}(n_1^2 - n_2^2)\frac{d}{dT}(\frac{u^2}{V^2}) \tag{4.8}$$

where it is noticeable that u is a function of V only, and V is a function of T. So the derivative at the end $\frac{d}{dT}(\frac{u^2}{V^2})$ can be re-written as:

$$\frac{d}{dT}(\frac{u^2}{V^2}) = \frac{d}{dV}(\frac{u^2}{V^2}) \cdot \frac{dV}{dT} \tag{4.9}$$

the expression $\frac{dV}{dT}$ can be calculated from the definition of V in Eq. (4.5):

$$\frac{dV}{dT} = \frac{V}{(n_1^2 - n_2^2)}(n_1\frac{dn_1}{dT} - n_2\frac{dn_2}{dT}) \tag{4.10}$$

Meanwhile, $\frac{d}{dV}(\frac{u^2}{V^2})$ can be calculated:

$$\frac{d}{dV}(\frac{u^2}{V^2}) = \frac{2u}{V^2}(\frac{du}{dV} - \frac{u}{V}) \tag{4.11}$$

The term $\frac{du}{dV}$ can be derived by differentiating both sides of Eq. (4.6) with respect to V:

$$\frac{d}{dV}(\frac{uJ_1(u)}{J_0(u)}) = \frac{d}{dV}(\frac{wK_1(w)}{K_0(w)}) \tag{4.12}$$

$$\frac{du}{dV} \cdot \frac{d}{du}(\frac{uJ_1(u)}{J_0(u)}) = \frac{dw}{dV} \cdot \frac{d}{dw}(\frac{wK_1(w)}{K_0(w)}) \tag{4.13}$$

The derivatives of relevant Bessel functions are given by:

$$\frac{dJ_0(i)}{di} = -J_1(i) \tag{4.14}$$

$$\frac{dK_0(i)}{di} = -K_1(i) \tag{4.15}$$

$$\frac{dJ_1(i)}{di} = J_0(i) - \frac{J_1(i)}{i} \tag{4.16}$$

$$\frac{dK_1(i)}{di} = -K_0(i) - \frac{K_1(i)}{i} \tag{4.17}$$

By applying the above relationships, Eq. (4.13) becomes:

$$\frac{du}{dV}\left[\frac{J_1(u)}{J_0(u)} + u\left(\frac{J_0(u)J_1'(u) - J_1(u)J_0'(u)}{J_0^2(u)}\right)\right] = \frac{dw}{dV}\left[\frac{K_1(w)}{K_0(w)} + w\left(\frac{K_0(w)K_1'(w) - K_1(w)K_0'(w)}{K_0^2(w)}\right)\right] \tag{4.18}$$

where $J_i'(u) = \frac{dJ_i}{du}$, $K_0'(w) = \frac{dK_0}{dw}$. By substituting for Eq. (4.6) this equation can be simplified to

$$u\frac{du}{dV}\left(1 + \frac{J_1^2(u)}{J_0^2(u)}\right) = w\frac{dw}{dV}\left(\frac{K_1^2(w)}{K_0^2(w)} - 1\right) \tag{4.19}$$

It is derived from $w^2 = V^2 - u^2$ that:

$$w\frac{dw}{dV} = V - u\frac{du}{dV} \tag{4.20}$$

so Eq. (4.19) may be written as

$$u\frac{du}{dV}\left(1 + \frac{J_1^2(u)}{J_0^2(u)}\right) = \left(V - u\frac{du}{dV}\right)\left(\frac{K_1^2(w)}{K_0^2(w)} - 1\right) \tag{4.21}$$

Applying Eq. (4.6) again this can be simplified to:

$$\frac{du}{dV} = \frac{u}{V}\left[1 - \frac{K_0^2(w)}{K_1^2(w)}\right] \tag{4.22}$$

so that $\frac{du}{dV}$ becomes:

$$\frac{du}{dV} = -2\frac{u^2}{V^3} \cdot \frac{K_0^2(w)}{K_1^2(w)} \tag{4.23}$$

Eventually, by substituting this expression into Eq. (4.8), the following is obtained:

$$\frac{dn_{eff}^2}{dT} = \frac{dn_1^2}{dT} \cdot \left[1 - \frac{u^2}{V^2}\left(1 - \frac{K_0^2(w)}{K_1^2(w)}\right)\right] + \frac{dn_2^2}{dT} \cdot \left[\frac{u^2}{V^2}\left(1 - \frac{K_0^2(w)}{K_1^2(w)}\right)\right] \tag{4.24}$$

Before further analysis, it is necessary to recognise the significance of the expressions in square brackets. In fact they are equivalent to expressions for the filling factors Γ_1 and Γ_2, the fractions of modal power in the core and the cladding, respectively. Here are the derivations. The scalar modal function ψ is given by:

$$\psi = AJ_0\left(\frac{ur}{a}\right) \qquad r \leq a \tag{4.25}$$

$$= A\frac{J_0(u)}{K_0(w)} \cdot K_0\left(\frac{wr}{a}\right) \qquad r > a \tag{4.26}$$

The normalisation constant A is defined as:

$$A = \frac{w}{aVJ_1(u)\sqrt{\pi}} \tag{4.27}$$

so that the mode is normalised as:

$$\int \psi^2 r dr d\theta = 1 \tag{4.28}$$

The filling factors Γ_1 and Γ_2 are defined and derived as:

$$\Gamma_1 = \int_0^a \psi^2 r dr d\theta = 1 - \frac{u^2}{V^2} \cdot \left(1 - \frac{K_0^2(w)}{K_1^2(w)}\right) \tag{4.29}$$

$$\Gamma_2 = \int_a^i nf\psi^2 r dr d\theta = \frac{u^2}{V^2} \cdot \left(1 - \frac{K_0^2(w)}{K_1^2(w)}\right) \tag{4.30}$$

By substituting those into Eq. (4.24) a key result is obtained:

$$\frac{dn_{eff}^2}{dT} = \frac{dn_1^2}{dT} \cdot \Gamma_1 + \frac{dn_2^2}{dT} \cdot \Gamma_2 \tag{4.31}$$

For temperature compensation, the turning point of the Bragg wavelength which with temperature is of interest, satisfying the condition $\frac{d_{neff}}{dT} = 0$. Also by normalisation $\Gamma_1 + \Gamma_2 = 1$, the filling factor Γ_2 must satisfy:

$$\Gamma_2 = \frac{n_1 \frac{dn_1}{dT}}{n_1 \frac{dn_1}{dT} - n_2 \frac{dn_2}{dT}} \tag{4.32}$$

This equation has elegantly separated the geometry related parameters to the left hand side while the material parameters are to the right hand side. This will be the key equation in designing different temperature compensated FBG devices.

General weakly guiding waveguides

The conclusion drawn in Eq. (4.32) can be shown to have a similar form as for general weakly guiding waveguides with arbitrary shapes of temperature controlled regions as shown in Fig. 4.16(b). The scalar wave equation at temperature T is given by:

$$\nabla_t^2 \psi(T) + k^2 n^2(T) \psi(T) = \beta^2(T) \psi(T) \tag{4.33}$$

where $n = n_i$ in each region of the waveguide and the Laplace operator with respect to time ∇_t^2 is determined by:

$$\nabla_t^2 = \frac{\partial}{\partial x^2} + \frac{\partial}{\partial y^2} \tag{4.34}$$

At a different temperature $T + \delta T$ the wave equation becomes

$$\nabla_t^2 \psi(T + \delta T) + k^2 n^2(T + \delta T) \psi(T + \delta T) = \beta^2(T + \delta T) \psi(T + \delta T) \tag{4.35}$$

Multiplying Eq. (4.33) by $\psi(T+\delta T)$ and subtracting by Eq. (4.35) multiplied by $\psi(T)$, the following is obtained after rearranging:

$$\begin{aligned}\left(\beta^2(T)-\beta^2(T+\delta T)\right)&\psi(T+\delta T)\psi(T)\\ &=k^2\left(n^2(T)-n^2(T+\delta T)\right)\psi(T+\delta T)\psi(T)\\ &\quad+\left(\psi(T+\delta T)\nabla_t^2\psi(T)-\psi(T)\nabla_t^2(T+\delta T)\right)\end{aligned}\tag{4.36}$$

Apply integration on both sides over all space:

$$\begin{aligned}\left(\beta^2(T)-\beta^2(T+\delta T)\right)&\int\psi(T+\delta T)\psi(T)dA\\ &=k^2\int\left(n^2(T)-n^2(T+\delta T)\right)\psi(T+\delta T)\psi(T)dA\\ &\quad+\int\left(\psi(T+\delta T)\nabla_t^2\psi(T)-\psi(T)\nabla_t^2(T+\delta T)\right)dA\end{aligned}\tag{4.37}$$

By applying the Green's second identity the last integral can be written as a line integral dl with a normal $\hat{n}$ around the area of integration:

$$\begin{aligned}\int&\left(\psi(T+\delta T)\nabla_t^2\psi(T)-\psi(T)\nabla_t^2(T+\delta T)\right)dA\\ &=\int\nabla\cdot\left(\psi(T+\delta T)\nabla_t\psi(T)-\psi(T)\nabla_t\psi(T+\delta T)\right)dA\\ &=\oint\left(\psi(T+\delta T)\nabla_t\psi(T)-\psi(T)\nabla_t\psi(T+\delta T)\right)\cdot\hat{n}dl\end{aligned}\tag{4.38}$$

At a distance infinitely far away, the wave function vanishes. Both ψ and $\nabla_t\psi(T)$ approach zero on the boundary. Therefore, this integral in Eq. (4.38) becomes zero if the area of integration is assumed to be infinity. Then Eq. (4.37) is left as:

$$\begin{aligned}\left(\beta^2(T)-\beta^2(T+\delta T)\right)&\int\psi(T+\delta T)\psi(T)dA\\ &=k^2\int\left(n^2(T)-n^2(T+\delta T)\right)\psi(T+\delta T)\psi(T)dA\end{aligned}\tag{4.39}$$

When both sides are divided by δT and the limit $\delta T\to 0$ is taken:

$$\frac{d\beta^2}{dT}\int\psi^2dA=k^2\int\frac{dn^2}{dT}\psi^2dA\tag{4.40}$$

Dividing both sides by k^2 gives:

$$\frac{dn_{eff}^2}{dT}\int\psi^2dA=\int\frac{dn^2}{dT}\psi^2dA\tag{4.41}$$

If the wave function ψ is normalised, so the integrals become 1. Using that $n = n_i$ in each region A_i, Eq. (4.41) becomes:

$$\frac{dn_{eff}^2}{dT} = \sum_{i=1} \frac{dn_i^2}{dT}\Gamma_i \tag{4.42}$$

where the filling factor Γ_i is defined as the integral of the wave function over each area A_i:

$$\Gamma_i = \int \psi^2 dA_i \tag{4.43}$$

Now consider a step index fibre with core, cladding, and control region indices n_1, n_2, and n_c, respectively. Since the cladding and core are made of the same material, and the waveguide is weak, then $n_1 = n_2$, and $\frac{dn_1^2}{dT} = \frac{dn_2^2}{dT}$. Thus Eq. (4.42) becomes:

$$\frac{dn_{eff}^2}{dT} = \frac{dn_1^2}{dT}(\Gamma_1 + \Gamma_2) + \frac{dn_c^2}{dT}\sum_{i=3}\Gamma_i \tag{4.44}$$

By considering the normalised wave function, $\Gamma_1 + \Gamma_2 + \Gamma_c = 1$, hence:

$$\frac{dn_{eff}^2}{dT} = \frac{dn_1^2}{dT}(1 - \Gamma_c) + \frac{dn_c^2}{dT}\Gamma_c \tag{4.45}$$

For a temperature compensated device, the condition for $\frac{d_{neff}}{dT}$ is derived as:

$$\Gamma_c = \frac{n_1 \frac{dn_1}{dT}}{n_1 \frac{dn_1}{dT} - n_c \frac{dn_c}{dT}} \tag{4.46}$$

Note that Eq. (4.46) is in the same form as Eq. (4.32). The conclusion drawn from the step-index fibre is therefore applicable generally to different waveguides.

4.7.2 Particular solutions in bow-tie and side hole fibres

Equation (4.46) indicates that if the filling factor of the control region is known, it can be used in conjunction with the material parameters to give an optimised design. A more detailed analysis was then derived for two specific shaped waveguides, bow-tie fibres and side hole fibres.

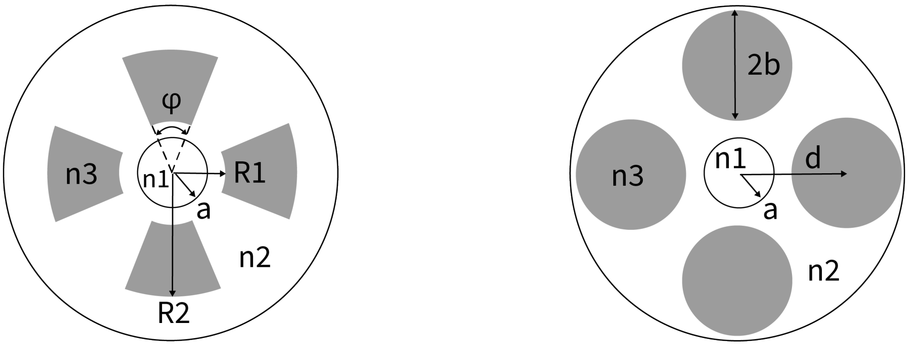

(a) Bow-tie shaped temperature control regions. **(b)** Four circular temperature control regions.

Figure 4.17: Step-index optical fibre with temperature control regions of different patterns.

Double bow-tie fibres

The design is a "double bow-tie" structure consisting of four segments. Each segment is an annulus shape enclosed by two straight lines and two arcs as shown in Fig. 4.17a. The arcs are concentric to the fibre core, with an angle of φ and radius of R_1 and R_2, respectively. Solving for the filling factor in an arbitrary geometry analytically is challenging. In the following calculations the condition $n_c = n_2$ at $T = T_{ref}$ should be satisfied, where T_{ref} is defined as the temperature when $\frac{dn_{eff}}{dT} = 0$.

At the reference temperature, the modal field will be that of a step-index fibre. The wave function is then independent of the angle φ. Thus the filling factor Γ_c in the control region is given by:

$$\Gamma_c = \int_{R_1}^{R_2} \psi^2 r dr \int_0^{\varphi} d\theta \tag{4.47}$$

By applying the wave function described in Eq. (4.26) the filling factor becomes:

$$\Gamma_c = A^2 \frac{J_0^2(u)}{K_0^2(w)} \varphi \int_{R_1}^{R_2} K_0^2\left(\frac{wr}{a}\right) r dr \tag{4.48}$$

The integral of K_0^2 follows the formula given by:

$$\int K_0^2 z dz = \frac{z^2}{2}\left[K_0^2(z) - K_1^2(z)\right] \tag{4.49}$$

By substituting Eq. (4.49) into Eq. (4.48), the following is obtained:

$$\begin{aligned}\Gamma_c = \frac{u^2\varphi}{2\pi V^2 K_1^2(w)} \cdot \{ & \frac{R_2^2}{a^2}\left[K_0^2\left(\frac{wR_2}{a}\right) - K_1^2\left(\frac{wR_2}{a}\right)\right] \\ & - \frac{R_1^2}{a^2}\left[K_0^2\left(\frac{wR_1}{a}\right) - K_1^2\left(\frac{wR_1}{a}\right)\right] \}\end{aligned} \tag{4.50}$$

When Γ_c in Eq. (4.50) meets the condition given by Eq. (4.46) it is possible to obtain a temperature compensated device. Note that although the double bow-tie shaped waveguide is easy to calculate, the difficulty of fabrication makes it less preferred compared with the side hole fibre introduced in the next subsection.

Side hole fibres

A side hole fibre here is defined as a step index fibre with a temperature control region consisting of a series of circular shapes as shown in Fig. 4.18. It is possible to analytically calculate the filling factor Γ_c at temperature when $n_3 = n_2$ by applying the step index equations, where the wave function is the same as Eq. (4.26) when $R > a$:

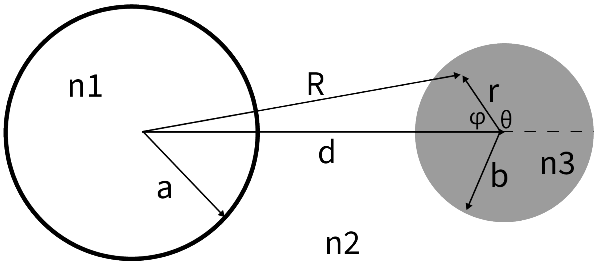

Figure 4.18: The geometry of the step index fibre with a side hole as a temperature control region.

$$\psi = A\frac{J_0(u)}{K_0(w)} \cdot K_0\left(\frac{wR}{a}\right) \tag{4.51}$$

The normalisation constant A is given by:

$$A = \frac{w}{aVJ_1(u)\sqrt{\pi}} \tag{4.52}$$

The filling factor of the control region Γ_c is given by:

$$\Gamma_c = \int \psi^2(R) r dr d\theta \tag{4.53}$$

Using the cosine rule, the distance R centred on the fibre core centre can be written as a function of the distance r centred at the hole centre:

$$R = \sqrt{r^2 + d^2 - 2rd\cos\varphi} \tag{4.54}$$

By applying the addition theorem for Bessel functions [99], and the angle relationship $\varphi = \pi - \theta$:

$$K_0\left(\frac{wR}{a}\right) = I_0\left(\frac{wr}{a}\right)K_0\left(\frac{wd}{a}\right) + 2\sum_{p=1}^{\infty}(-1)^p I_p\left(\frac{wr}{a}\right)K_p\left(\frac{wd}{a}\right)\cos(p\theta) \tag{4.55}$$

The integral of $K_0^2\left(\frac{wR}{a}\right)$ over θ can be calculated as the terms $\cos(p\theta)$ are orthogonal over the range 0 to 2π, and $\int_0^{2\pi}\cos^2(p\theta)d\theta = \pi$. The integral over the whole control region becomes:

$$\int K_0^2\left(\frac{wR}{a}\right)rdrd\theta = 2\pi\int_0^b I_0^2\left(\frac{wr}{a}\right)K_0^2\left(\frac{wd}{a}\right)rdr + 4\pi\sum_{p=1}^{\infty}\int_0^b I_p^2\left(\frac{wr}{a}\right)K_p^2\left(\frac{wd}{a}\right)rdr \tag{4.56}$$

Some relevant Bessel function integrals are given by:

$$\int zI_p^2(\lambda z)dz = \frac{z^2}{2}I_p^2(\lambda z) - I_{p-1}(\lambda z)I_{p+1}(\lambda Z) \tag{4.57}$$

$$\int zI_0^2(\lambda z)dz = \frac{z^2}{2}I_0^2(\lambda z) - I_1(\lambda Z) \tag{4.58}$$

By substituting the above integrals into Eq. (4.56):

$$\int K_0^2\left(\frac{wR}{a}\right)rdrd\theta \tag{4.59}$$

$$= \pi b^2 K_0^2\left(\frac{wd}{a}\right)\left(I_0^2\left(\frac{wb}{a}\right) - I_1^2\left(\frac{wb}{a}\right)\right) \tag{4.60}$$

$$+ 2\pi b^2\sum_{p=1}^{\infty}\left(I_p^2\left(\frac{wb}{a}\right) - I_{p-1}\left(\frac{wb}{a}\right)I_{p+1}\left(\frac{wb}{a}\right)\right)K_p^2\left(\frac{wd}{a}\right) \tag{4.61}$$

Then the filling factor Γ_c is calculated to be :

$$\Gamma_c = \frac{w^2b^2}{a^2V^2}\cdot\frac{J_0^2(u)}{J_1^2(u)K_0^2(w)} \tag{4.62}$$

$$\cdot\left[K_0^2\left(\frac{wd}{a}\right)\left(I_0^2\left(\frac{wb}{a}\right) - I_1^2\left(\frac{wb}{a}\right)\right)\right. \tag{4.63}$$

$$\left.+2\pi b^2\sum_{p=1}^{\infty}\left(I_p^2\left(\frac{wb}{a}\right) - I_{p-1}\left(\frac{wb}{a}\right)I_{p+1}\left(\frac{wb}{a}\right)\right)K_p^2\left(\frac{wd}{a}\right)\right] \tag{4.64}$$

By applying the eigenvalue equation Eq. (4.6), the expression for Γ_c finally becomes:

$$\Gamma_c = \frac{u^2b^2}{a^2V^2K_1^2(w)} \tag{4.65}$$

$$\cdot\left[K_0^2\left(\frac{wd}{a}\right)\left(I_0^2\left(\frac{wb}{a}\right) - I_1^2\left(\frac{wb}{a}\right)\right)\right. \tag{4.66}$$

$$\left.+2\pi b^2\sum_{p=1}^{\infty}\left(I_p^2\left(\frac{wb}{a}\right) - I_{p-1}\left(\frac{wb}{a}\right)I_{p+1}\left(\frac{wb}{a}\right)\right)K_p^2\left(\frac{wd}{a}\right)\right] \tag{4.67}$$

Now by equating Eq. (4.67) with Eq. (4.46) the geometry and refractive indices of a side-hole temperature compensated FBG devices can be predicted.

4.8 Conclusion

The work introduced in this chapter has shown a complete path from an idea to manufacturable device designs. In the initial stages of the work it was verified by simulation how the microchannels would affect FBG performance. Then the problem was set up to find the best liquid and optimise the waveguide and FBG parameters. After which, general design graphs for two different methods were generated, simplifying the problem into two parameters, the liquid area and the liquid refractive index. Further work was been introduced to optimise the temperature compensated device for more precise future manufacturing such as making custom fibres. The designs also introduce some tolerance which allows fabrication with non-perfect accuracy.

The significance of this work is that the design graphs derived from double cladding fibre or bow-tie shaped fibre provide a guideline on fabricating FBG devices with various temperature sensitivities over defined temperature ranges. For a laser fabricated FBG device, although the focal position was reasonably accurate, there was some tolerance on the sizes and shapes of the micro-channels. So the design graphs which provide the relationship between the temperature sensitivity and the hole area were more than enough for fabrication. In fact, with the help of these design graphs, FBG sensors with an ultra high temperature sensitivity or an ultra low temperature sensitivity have successfully been fabricated, which are discussed in the later chapters.

For a more accurate fabrication with custom fibre however, the hole geometries will be very precisely controlled. In the later chapters, work on the optimisation of temperature-compensated FBG devices, which provide more accurate sweeping of geometry parameters, will be necessary. Thus, designs with bow-tie shaped holes and side holes have been analysed. The designs with side holes are further simulated for an optimised design that is suitable for custom fibre fabrication in the later chapters.

5

Direct laser writing with aberration correction

Contents

5.1 Introduction

The refractive indices of glasses can be modified by exposure to intense light. The development of femtosecond lasers has allowed a much higher laser intensity and as a result, a wider range of studies on laser-matter interaction has been established. Also a femtosecond laser has less heat dissipation into surrounding areas. Permanent physical and chemical modifications of transparent materials induced by lasers were demonstrated in 1996 with near infra-red femtosecond pulses, including refractive index modification [100][101] and etching rate enhancement [102]. By focusing the femtosecond laser into the bulk of transparent materials, desired patterns can be written onto the materials. This technique, known as Direct Laser Writing (DLW) or Femtosecond Laser Inscription (FLI) [103] [104], has been widely used and has allowed a variety of applications such as 3-D integrated optical devices [105], and microfluidic chips [106].

In this work, a femtosecond direct laser writing system was used extensively for important processes of fabrication including FBG formation and laser assisted chemical etching. Aberration correction was used to overcome distortion due to the refractive index mismatch of the material being processed and the surrounding air. In this chapter, there will be demonstration of the femtosecond direct laser writing system used and the aberration correction methods.

5.2 Femtosecond Direct Laser writing system

5.2.1 System configuration

A regenerative femtosecond laser system (Light Conversion Pharos SP-06-1000-PP) was used at a second harmonic generation wavelength of 515 nm and a pulse duration of 170 fs. A half-waveplate in conjunction with a polarizer was used to control the pulse energy between 10 and 300 nJ. A spatial light modulator (SLM) (Hamamatsu X10468) was used to compensate for the aberration generated in the optical path of the whole system. The fibre was taped onto a microscope slide and placed on a motion stage (x, y: Aerotech ABL10100L and z: ANT95-3-V). The objective used had a ×20 magnification and numerical aperture of 0.5.

5.2.2 Laser writing process

This section briefly introduces the physical principles behind DLW and how they can be used for fabrication of devices.

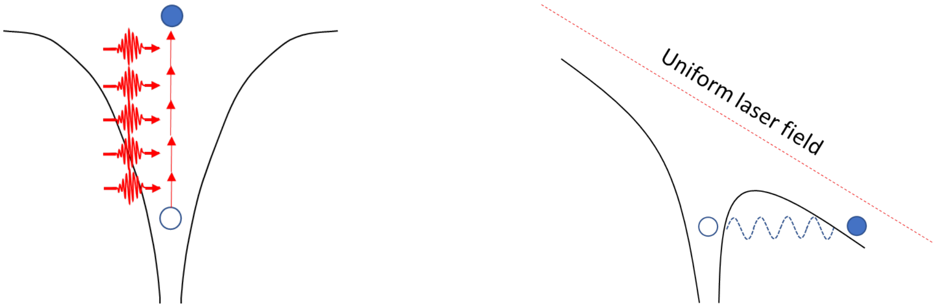

(a) Multiphoton ionisation **(b)** Tunnelling ionisation

Figure 5.1: Two mechanisms of nonlinear photoionisation. When $\gamma >> 1.5$ multiphoton ionisation dominates and when $\gamma << 1.5$ tunnelling ionisation dominates. For $\gamma \approx 1.5$ we expect an intermediate between both.

Light-matter interaction

For a transparent material such as fused silica, there is no linear absorption of the induced laser photons at visible light wavelengths. Thus, in order to achieve optical breakdown followed by material damage, one of the two nonlinear absorption mechanisms of photons must take place, that is photoionisation and avalanche ionisation [107]. As a result of both ionisation mechanisms, the plasma of free electrons is formed and free carriers start to accumulate.

Nonlinear Photoionisation

Photoionisation refers to the excitation of electrons from the atoms' valence band by absorption of energy of induced light [108]. There are two possible nonlinear photoionisation processes during FLI, multiphoton ionisation and tunnelling ionisation [109].

One single photon of visible light is unable to provide sufficient energy to excite an electron from the valence band to the conduction band. However, the electron can simultaneously absorb multiple sub-bandgap photons as shown in Fig. 5.1(a). The total energy gained by the electron by absorbing photons must be higher than the bandgap energy given by [110]:

$$N\nu h > E_g \tag{5.1}$$

where N is the number of photons absorbed by the electron, ν is the photon frequency, h is the Plank's constant and E_g is the bandgap energy, which is about 8.9 eV for silica[111]. During multiphoton ionisation, the photoionisation rate P_{MPI} is given by [107]:

$$P_{MPI} = \sigma_N I^N \tag{5.2}$$

where I is the intensity of the laser at focus and σ_N is the multiphoton absorption coefficient [112]. From this estimation, we realise that the rate is largely dependent on the laser intensity. Multiphoton ionisation is dominant when the induced laser has high frequency and low intensity.

As the intensity increases, the potential barrier is lowered by the induced electric field of the laser. The potential barriers that prevent electrons from escaping from their parent atoms are weakened. As a result, quantum tunnelling occurs and electrons are released into the conduction band as shown in Fig. 5.1b. This type of ionisation is called tunnelling ionisation. Compared with multiphoton ionisation, tunnelling ionisation has less dependence on laser intensity.

Both of the mechanisms can be described within the same theoretical framework. The likelihood of multiphoton ionisation and/or tunnelling ionisation to take place is modelled by the Keldysh parameter γ [113],

$$\gamma = \frac{\omega}{e}\left[\frac{mcn\epsilon_0 E_g}{I}\right]^{\frac{1}{2}} \tag{5.3}$$

where ω is the angular frequency of the induced laser, e and m are the charge and mass of a single electron, respectively, c is the speed of light, n is the refractive index of the material and ϵ_0 is the free space permittivity. Despite the material parameters, γ is dependent on the frequency and the intensity of the induced laser. For high frequency and low intensity such that $\gamma >> 1.5$, multiphoton ionisation is dominant. While for a higher intensity when $\gamma << 1.5$, tunnelling ionisation dominates. For FLI the Keldysh parameter is approximately 1 therefore both multiphoton and tunnelling ionisation are expected [107].

(a) Free carrier absorption **(b)** Impact ionisation

Figure 5.2: Photons are absorbed by the electrons in the conduction band followed by impact ionisation.

Avalanche photoionisation

Photon absorption also occurs in electrons within the conduction band. After free-carrier absorption of several photons, an electron may gain enough energy to impact excite another electron from the valence band across the bandgap. The two electrons end up at a minimum of the conduction band. Both electrons will then keep absorbing photons and impact ionise others. This ionisation process, called avalanche ionisation, is continuous as long as there are sufficient 'seed' electrons and a strong electric field. The condition for avalanche ionisation is similarly given by Eq. (5.1), but in this case N refers to the number of photons absorbed by an electron in the conduction band. The 'seed' electrons are initially provided either by ionised impurities, thermal effects or nonlinear photoionisation (including multiphoton and tunnelling ionisation)[107].

Optical breakdown

As more electrons are excited to the conduction band a micro-plasma of free carriers is formed. When the free electrons have accumulated, the frequency of the plasma increases and eventually it reaches the laser frequency; the plasma becomes strongly absorbing and boosts the avalanche photoionisation [109]. This is often considered as the threshold for optical breakdown when permanent damage will be found in the material. Modifications to the material may occur when the energy is transferred from the plasma to the lattice. For femtosecond pulses, the time scale for absorption of photons is much less than that for energy transfer between ions in the lattice (several picoseconds) [114]. Therefore the effects from the lattice heating process and laser-induced photon absorption are decoupled.

When there is only nonlinear photoionisation, the threshold intensity for optical breakdown varies significantly between materials of different bandgap energies. However, when avalanche ionisation dominates, the rate is approximately linearly dependent on the intensity so the threshold does not vary much for different bandgap energy [115]. Therefore, the theory of optical breakdown can be applied to a wide range of materials.

Generally, the modifications to the material are classified into three types depending mainly on the laser intensity [116]: (i) A modification of the refractive index caused by the densification of the materials [117], causing a smooth refractive index change [100] or a birefringent index modification [101]. (ii) A higher pulse energy causes formation of nano-gratings or nano-pores [103], which are resultant from the interference of electric field. The nano-pores are easier to be washed away by a chemical etchant such as HF or KOH. (iii) With higher intensity, the plasma will cause micro-explosions and break the lattice [118]. This so-called laser ablation process forms tracks at the micrometre scale.

5.2.3 Femtosecond laser assisted selective chemical etching

Figures of merit

There are two main figures of merit that determine the performance of etching and help us to think about the parameter space. Firstly, a reasonable etching rate is expected. Based on the Bragg grating conditions of the device, the aim is to fabricate micro-channels that are several millimetres long. To complete the etching process within several days, the goal is to achieve an etching rate of tens to a hundred micrometres per hour.

Selectivity S should also be taken into consideration, defined as the ratio of the etching rate of the modified region to that of the unmodified region given by [110].

$$S = (l + \epsilon t)/\epsilon t) \tag{5.4}$$

where l is the distance etched in the laser modified region, ϵ is the pristine material etching rate depending on the etchant and material, and t is the etching time. Note in the equation that an extra term of ϵt appears in the numerator assuming that pristine material etching also takes place in the laser modified region. The devices with microchannels are approximately several millimetres in length and several micrometres in diameter. Thus, in order to ensure that the channels have a uniform cylindrical shape a selectivity of up to one thousand is expected.

Etchant

The mechanism of HF as an etchant is well understood. HF reacts with pristine silica with a series of four sequential steps after which an Si-O bond is broken due to the insertion of an HF molecule [119]. Among the four steps, the replacement of the first oxygen atom is 20 times slower than the subsequent steps [120]. After laser inscription, the average number of oxygen molecules attached to each silica molecule reduces in the laser modified region [121]. As a result of fewer Si-O bonds being broken (which limits the rate of a chemical reaction) the etching rate in the modified region is needed to be much faster than that of pristine silica.

On the other hand, a similar theory of silica densification cannot be applied to KOH. One reasonable explanation involves the formation of microcrystalline silica within the bulk of the region exposed to FLI [122]. The hydroxide molecules provided by the KOH can bind to the silica molecules of crystalline silica and break the Si-Si bonds [123]. Therefore, crystalline silica gives a much higher etching rate of up to three orders of magnitude compared with pristine silica [124]. As a result, KOH often provides a significantly higher selectivity compared to HF.

Studies have shown that the etching rate of HF is up to 300 μm/hour [125] while that of KOH is a bit less at 290 μm/hour[126]. However, in terms of selectivity

KOH performs much better as it does not react with pristine silica. A study has shown that under controlled parameters the maximum selectivities for 5% HF and 8 mol/L KOH were found to be 66 and 955, respectively [110].

Parameter Study

It is necessary to study the parameters that affect the performance of femtosecond laser assisted etching (FLAE), including the laser parameters. Intensity related parameters such as pulse energies [127], pulse duration [126], repetition rate [104] and writing speed [128] have been investigated in the previous studies. The intensity should be high enough to excite the electrons and cause avalanche photoionisation but in a limited range to prevent micro-explosions around the channel, which leads to a trade-off between etching rate and selectivity. In addition, the polarisation of the laser should also be considered since the electric field is essential to the photoionisation process. For the multiphoton ionisation mechanism to take place, the wavelength of the laser should be such that the photon energy is sufficient. Also, sub-picosecond pulses are fundamental requirements in order to decouple lattice heating and photon absorption during the photoionisation process. In order to achieve higher selectivity, the direction of polarisation should be perpendicular to the writing direction [125]. For the same reason, a selected direction of polarisation would significantly improve the surface roughness [103]. Beam shaping methods using a spatial light modulator (SLM) will give better control of the written patterns [129].

Etching Trials

In order to identify a suitable recipe for etching, etching trials were conducted on a rectangular fused silica substrate. The laser used was a Pharos SP-06-1000-PP with a pulse duration of 170 fs, repetition rate up to 1 MHz, a wavelength of 514 nm, pulse energy up to 1 mJ and an average power up to 6 W. Initially, the same parameters were used as Ross *et al.* with KOH as the etchant [103].

The experiment set-up is shown in Fig. 5.3. The laser beam was shaped by an SLM and focused into the bulk of the sample, which was placed on a translation stage. straight channels were written with different powers, writing speeds and polarisations.

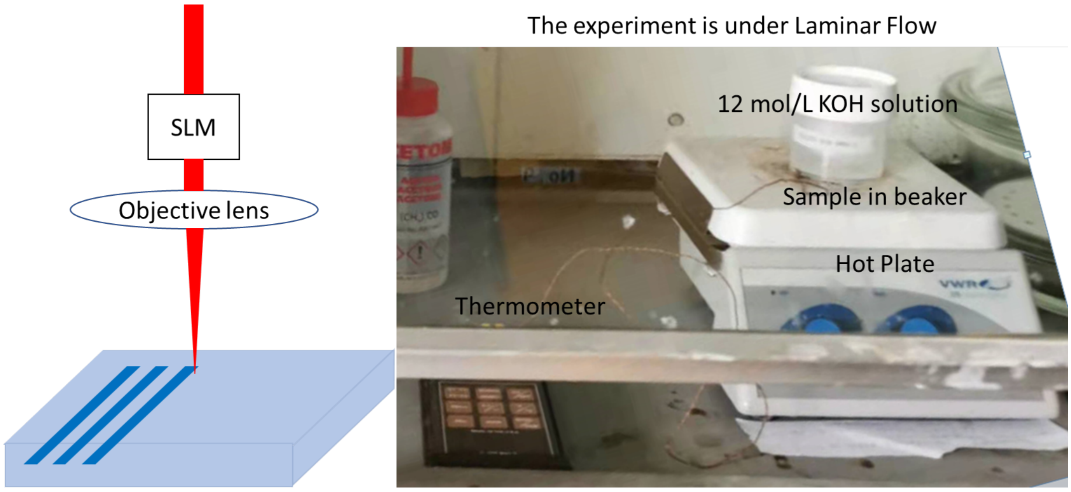

(a) Laser writing on a rectangular substrate. **(b)** KOH etching of the substrate

Figure 5.3: Experiment set-up of our etching trials: (a) Femtosecond laser inscription of nanogratings followed by (b) Chemical etching with 12mol/L KOH solution heated to 85°C.

Then the sample was polished on both edges to expose the modified region. Finally, the sample was placed in 12 mol/L KOH solution and heated to 85 °C.

Some of the results of the etching trials are presented in Fig. 5.4. A maximum etching rate of 130 μm/hour was achieved at a writing speed of 0.5 mm/s, power above 300mW and when the polarisation of the laser was perpendicular to the writing directions.

The parameters are then applied to a microchannel. in a bulk substrate with two entrances from the surface. The etched channel is presented in Fig. 5.5. The etching took 4.5 hours. The middle part of the channel seemed not to be fully etched thus one more etching may be required.

5.3 Aberration correction by direct laser writing

5.3.1 Introduction

Direct laser writing plays a significant role in the fabrication processes, including the FBG formation, laser assisted chemical etching and potentially direct laser ablation for LC alignment. Unfortunately, the intrinsic mechanism of direct laser writing relies heavily on the quality of the laser beam focus. Attempts have been reported

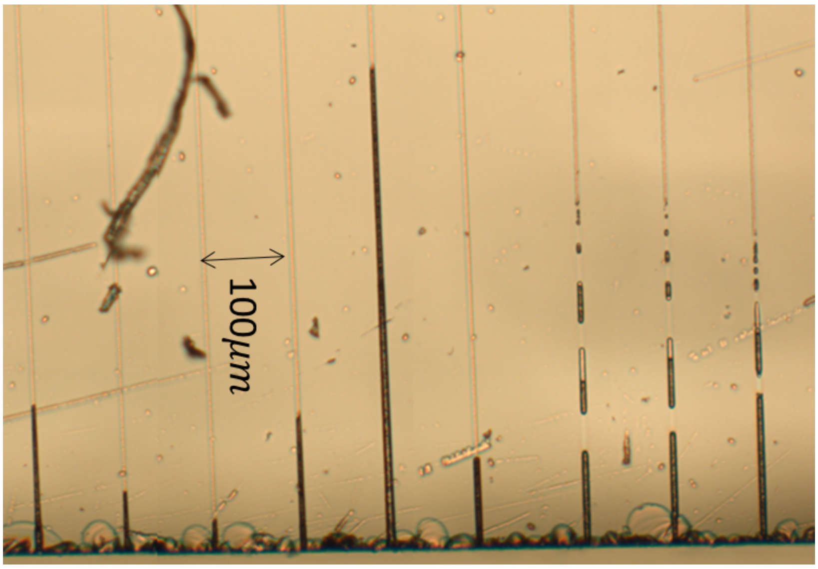

Figure 5.4: Some etching results following the steps in Fig. 5.3 taken on a microscope. The separations between two adjacent channels are 100 μm. The channels are written with different power, polarisation of laser and writing speed. However, the difference in etching depth is mainly due to the surface polishing condition.

Figure 5.5: Etching results of a microchannel with entrances from the surface of a fused silica bulk substrate. Top view taken under a microscope. The two parts of the figure each show a half of the same channel. The channel is 1100 μm in length and about 7 μm in width. The first and last 50 μm of the channel are 45° written from surface. Then the channel is written horizontally at the depth of 50 μm and length of 1 mm.

to resolve this problem such as immersing the fibres in oil [130][74][131][132], putting the fibres in a ferrule [133] and using a cylindrical lens [134]. Beam shaping is another solution and has be reported in for different applications including the fabrication of symmetric micro-channels [135], waveguides [136] and FBGs in D-shaped fibre [137]. However, these methods are not suitable for mass production. Moreover, since the designed FBGs filled with liquids should have more than one entrance from the side of the fibre, there is a requirement on focusing the laser beam into different positions inside the fibre. Hence the aberration of a laser beam varies according to the focal position. For example, when focusing on the surface of the fibre there is no aberration caused by the fibres, while focusing in the centre of the fibre raises a combination of astigmatism and defocus. There is a requirement of continuous variation in aberration parameters to create a channel from the evanescent field to the fibre surfaces. This introduces a method based on adaptive optics with an SLM as a development from a previous work by the group [138]. The aberrations while focusing at different positions within the fibre were calculated. A wavefront compensation could then be applied to the laser beam before the objective lens so that the focal position is corrected.

5.3.2 Geometrical Analysis

Define the Coordinates

The origin of distortions at the focus comes from wavefront difference or aberration. Without aberration, a parallel wavefront is required at the pupil plane for the best spherical wavefront towards the focus. The wavefront can be characterised by the relative phase delay ψ at different spatial positions. Now we consider an interface

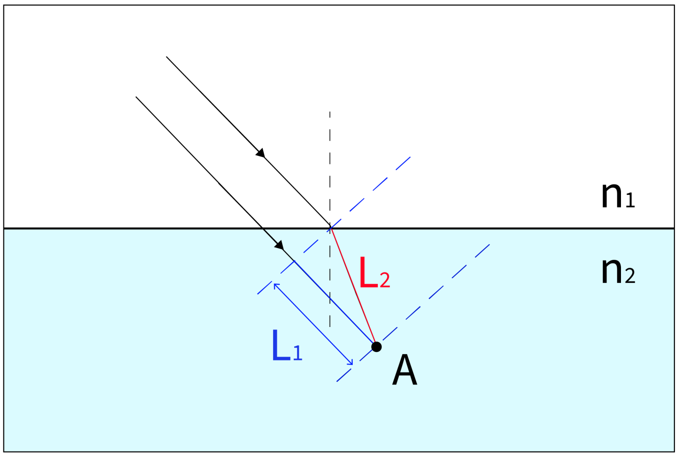

Figure 5.6: Interface between two materials with refractive indices of n_1 and n_2. This plot is used to define the phase delay caused by refraction.

between two transparent materials with refractive indices of n_1 and n_2 respectively as shown in Fig. 5.6. The figure indicates two possible paths of light rays sourced from an infinite distance reaching the same point A inside the second material. One path assumes the ray reaches A without any refraction while the other takes refraction into consideration. The optical path difference between the two paths can be used to define the phase delay ψ, given by:

$$\psi = \frac{2\pi}{\lambda}(n_2 L_2 - n_1 L_1) \tag{5.5}$$

where λ is the wavelength of incident of the rays, n_1L_1 and n_2L_2 are the optical paths. The next aim is to put the phase delay ψ in a more complex and realistic circumstance by considering focusing a laser beam into a position A of an optical fibre. It is assumed that refraction only occurs at the air-fibre interface (negligible refraction at the cladding-core interface). Note that because of the geometry of the fibres it is easier to trace the light from the focal point back to the pupil plane,

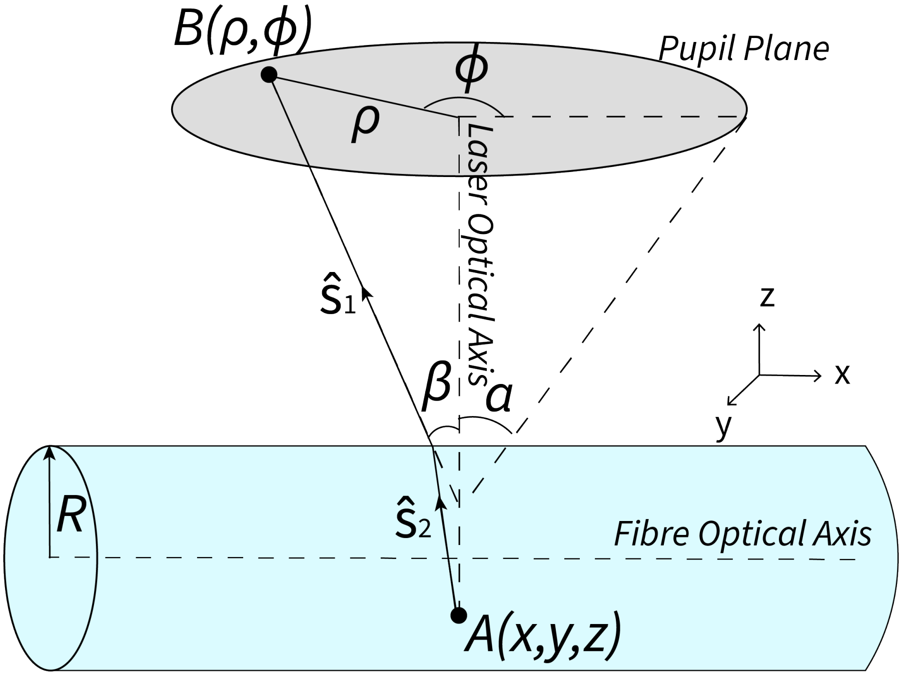

Figure 5.7: The coordinate system set up for the aberration calculation. A light ray is traced from a position $A(x, y, z)$ inside the fibre sample with a radius R, to a position $B(\rho, \phi)$ at the pupil plane. The light ray propagates along the directions $\hat{s}_1$ and $\hat{s}_2$ before and after refraction. The ray approaches the pupil plane at an angle of β from the laser optical axis. The acceptance angle of the pupil plane is α

this will be explained later. The coordinate system is established in Fig. 5.7 as follows: a general ray at a direction $\hat{s}_2$ is traced from the focal point $A(x, y, z)$ in a Cartesian coordinate with an origin on the fibre optical axis. This ray is refracted at the interface between the fibre glass and the air then propagates in the direction $\hat{s}_1$. Both $\hat{s}_1$ and $\hat{s}_2$ are unit vectors so that $\|\hat{s}_1\| = 1$ and $\|\hat{s}_2\| = 1$. The ray approaches the pupil plane at an angle of β from the laser optical axis, and reaches a point $B(\rho, \phi)$ at the pupil plane. The acceptance angle of the pupil plane is α.

Snell's Law in vector form

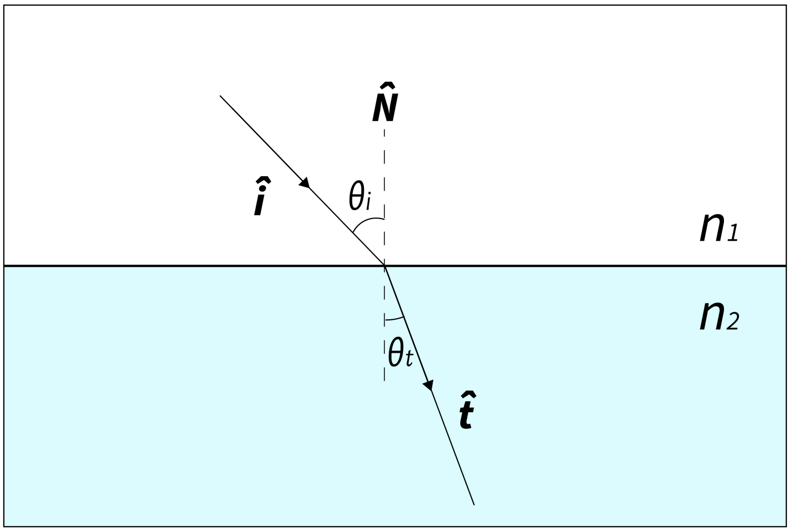

Figure 5.8: Plot of a ray refracted and transmitted through the interface of two media of different refractive indices applying Snell's law.

It is obvious that since $\hat{s}_2$ is a refracted ray from $\hat{s}_1$ they must satisfy a relationship defined by Snell's law. In this subsection a three dimensional vector form of Snell's law is derived. In Fig. 5.8, a light ray in direction $\hat{\imath}$ is refracted at the interface between the two media with different refractive indices n_i and n_t such that it is in a direction $\hat{t}$. The angle of incidence is θ_i, the angle of refraction is θ_t and the unit vector for the normal at the intersection is $\hat{N}$. The unit vectors $\hat{\imath}$ and $\hat{t}$ can each be decomposed into two vectors along horizontal and vertical directions as:

$$\hat{\imath} = \vec{i_{\parallel}} + \vec{i_{\perp}} \tag{5.6}$$

$$\hat{t} = \vec{t_{\parallel}} + \vec{t_{\perp}} \tag{5.7}$$

where the parallel subscript $\|$ is for that along the interface and the perpendicular subscript $\perp$ indicates the direction along the normal. Snell's law defines the relationship between the angles of incidence and refraction, and the refractive indices as:

$$n_i \sin(\theta_i) = n_t \sin(\theta_t) \tag{5.8}$$

where the trigonometric terms can be written as:

$$\sin(\theta_v) = \frac{\|\vec{v_\|}\|}{\|\hat{v}\|} = \|\vec{v_\|}\| \tag{5.9}$$

where $\hat{v}$ is a general unit vector decomposed similarly as in Eq. (5.7). So that Eq. (5.8) can be re-written as:

$$\begin{aligned} n_i\|\vec{i_\|}\| &= n_t\|\vec{t_\|}\| \\ \|\vec{t_\|}\| &= \frac{n_i}{n_t}\|\vec{i_\|}\| \end{aligned} \tag{5.10}$$

Since the vectors $\vec{i_\|}$ and $\vec{t_\|}$ are parallel to each other we have:

$$\begin{aligned} \vec{t_\|} &= \frac{n_i}{n_t}\vec{i_\|} \\ &= \frac{n_i}{n_t}[\hat{i} - \vec{i_\perp}] \end{aligned} \tag{5.11}$$

By substituting $\vec{i_\perp} = \cos\theta_i \hat{N}$ it becomes:

$$\vec{t_\|} = \frac{n_i}{n_t}[\hat{i} - \cos\theta_i \hat{N}] \tag{5.12}$$

By Pythagoras, the perpendicular component can be found as:

$$\vec{t_\perp} = \|\vec{t_\perp}\|\hat{N} = \sqrt{1 - \|t_\|\|^2}\hat{N} \tag{5.13}$$

Now the transmitted vector $\hat{t}$ can be written as the sum of the two components as:

$$\begin{aligned} \hat{t} &= \vec{t_\|} + \vec{t_\perp} \\ &= \frac{n_i}{n_t}[\hat{i} - \cos\theta_i \hat{N}] + \sqrt{1 - \|t_\|\|^2}\hat{N} \end{aligned} \tag{5.14}$$

Using the trigonometric relationship in Eq. (5.9) and after some re-arrangement $\hat{t}$ becomes:

$$\hat{t} = \frac{n_i}{n_t}\hat{i} + \left(\sqrt{1 - \sin^2\theta_t} - \frac{n_i}{n_t}\cos\theta_i\right)\hat{N} \tag{5.15}$$

The Snell's law in Eq. (5.8) can be used again here to re-write the trigonometric terms of refractive angle as:

$$\begin{aligned}\sin^2\theta_t &= \left(\frac{n_i}{n_t}\right)^2 \sin^2\theta_i \\ &= \left(\frac{n_i}{n_t}\right)^2 (1-\cos^2\theta_i)\end{aligned} \tag{5.16}$$

By taking into consideration that $\cos\theta_i = \hat{\imath}\cdot\hat{N}$ the following is obtained:

$$\hat{t} = \frac{n_i}{n_t}\hat{\imath} + \left(\sqrt{1-\left(\frac{n_i}{n_t}\right)^2 (1-(\hat{\imath}\cdot\hat{N})^2)} - \frac{n_i}{n_t}(\hat{\imath}\cdot\hat{N})\right)\hat{N} \tag{5.17}$$

This is the vector form of Snell's law. This equation can be further simplified and written as the cross product form by employing the vector triple product rule:

$$a\times(b\times c) = (a\cdot c)b - (a\cdot b)c \tag{5.18}$$

$$(a\times b)\times c = (a\cdot c)b - (b\cdot c)a \tag{5.19}$$

By applying the relationship $|a\times b| = \|a\|\|b\|\sin\theta$ the equation Eq. (5.17) becomes:

$$\hat{t} = \frac{n_i}{n_t}\hat{N}\times(\hat{\imath}\times\hat{N}) + \sqrt{1-\left(\frac{n_i}{n_t}\right)^2 \|\hat{\imath}\times\hat{N}\|^2}\hat{N} \tag{5.20}$$

Calculate the aberrations

It is now possible to substitute in the unit vectors $\hat{s}_1$, $\hat{s}_2$ and $\hat{N}$ into Eq. (5.20) as:

$$\hat{s}_2 = \frac{n_1}{n_2}\hat{N}\times(\hat{s}_1\times\hat{N}) + \sqrt{1-\left(\frac{n_1}{n_2}\right)^2 \|\hat{s}_1\times\hat{N}\|^2}\hat{N} \tag{5.21}$$

Note that $\hat{s}_1$ is made an independent variable which can be defined in terms of the pupil plane coordinates:

$$\hat{s}_1 = \begin{pmatrix}\rho\,\sin(\alpha)\cos(\phi) \\ \rho\,\sin(\alpha)\sin(\phi) \\ \sqrt{1-\rho^2\sin^2(\alpha)}\end{pmatrix} \tag{5.22}$$

This definition for $\hat{s}_1$ will be used later.

Now let the unit vectors $\hat{N}$ and $\hat{s}_2$ interact at a point I, such that the ray traced inside the fibre $\vec{AI}$ can be written as:

$$\begin{aligned}\vec{AI} &= \vec{OA} + \|\vec{AI}\|\hat{s}_2 \\ &= \begin{pmatrix}x+L_2s_{2x} \\ y+L_2s_{2y} \\ z+L_2s_{2z}\end{pmatrix}\end{aligned} \tag{5.23}$$

where the physical path L_2 was defined earlier in Fig. 5.6, and s_{2x}, s_{2y}, and s_{2z} are the orthogonal components of $\hat{s}_2$. So the unit vector $\hat{N}$ is :

$$\hat{N} = \frac{1}{R}\begin{pmatrix} 0 \\ y + L_2 s_{2y} \\ z + L_2 s_{2z} \end{pmatrix} \tag{5.24}$$

where R is the fibre radius. Now there is a relationship between $\hat{N}$ and $\hat{s}_2$, the next step is to find an expression for L_2. Note that the vector $\vec{OI}$ points from the fibre optical axis to the fibre surface, the fibre radius R can be used to write an equation:

$$(y + L_2 s_{2y})^2 + (z + L_2 s_{2z})^2 = R^2 \tag{5.25}$$

This quadratic equation can be solved for L_2 using the quadratic formula:

$$L_2 = \frac{-b \pm \sqrt{b^2 - 4ac}}{2a} \tag{5.26}$$

the positive root of which is taken, where

$$\begin{aligned} a &= s_{2y}^2 + s_{2z}^2 \\ b &= 2(y s_{2y} + z s_{2z}) \\ c &= y^2 + z^2 - R^2 \end{aligned} \tag{5.27}$$

By substituting Eq. (5.24) and Eq. (5.22) into Eq. (5.21), it can be used to solve for s_{2x}, s_{2y} and s_{2z} with a fixed pupil plane point $B(\rho, \phi)$ and focal point inside the fibre $A(x, y, z)$. Then the physical path L_2 can be calculated.

It is straightforward to show that the physical path L_1 in Fig. 5.6 is:

$$L_1 = L_2 \|\hat{s}_1 \cdot \hat{s}_2\| \tag{5.28}$$

Therefore, the optical phase delay ψ tracing from the position $A(x, y, z)$ to the position $B(\rho, \phi)$ is:

$$\psi(x, y, z, \rho, \phi) = \frac{2\pi}{\lambda}(n_2 - n_1\|\hat{s}_1 \cdot \hat{s}_2\|)L_2 \tag{5.29}$$

5.3.3 Numerical analysis

Notice that Eq. (5.21) is a transcendental equation with no analytical solution, but the equation can be solved numerically.

Solve for the equation

The first method I attempted was to solve for the equation by iteration. For every position $B(\rho, \phi)$ on the pupil plane, the path needs to be calculated to reach a position $A(x, y, z)$ inside the fibre. However, since the normal vector $\hat{N}$ is undetermined, an initial estimate of s_2, say s_2' is made. Then it is possible to locate the interface and a normal vector $\hat{N}'$ so that a refracted unit vector s_1' can be calculated. Then this predicted s_1' is compared with the actual s_1 defined by the pupil position $B(\rho, \phi)$. This process is iterated until eventually an s_1' value which is sufficiently close is obtained. However, there are several circumstances where the iteration does not converge. Firstly, it is not always predictable in what direction s_2 should be shifted in order to improve the estimate of s_1. There are positions where an increase in ρ or β of s_2 would cause them to decrease in s_1. Secondly, the iteration can ofter get stuck in a local maxima where one of the ρ and β falls is optimium while the other is still far away. A better initial estimate would make the iteration faster but it is still complex to deal with all the circumstances.

An alternative method used was to scan the whole parameter space of s_2. The equation Eq. (5.21) was used to calculate a predicted s_2' for each position of s_1. Instead of iterating the difference, this time the minimum difference from s_2 and s_2' was plotted over the whole parameter space. This method was slower but more reliable compared with the iteration method as the program always gives a solution. The results were further improved by optimising the steps. Practically, the iteration method works better when the focal position A is near the centre of the fibre and above the centre of the fibre. However, the scan method gives a better estimation when tracing the focus near the point of total internal refraction. In the following subsections both methods are used for numerical derivation depending on the circumstances.

Z Depth

In terms of the FBG designs, it is most useful to correct for aberrations at different depths. It is less necessary to calculate the aberrations on the sides since the

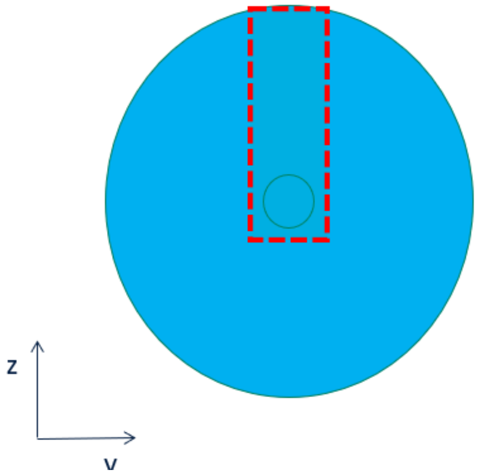

Figure 5.9: The region where the aberration correction is required for the novel FBG devices fabrication.

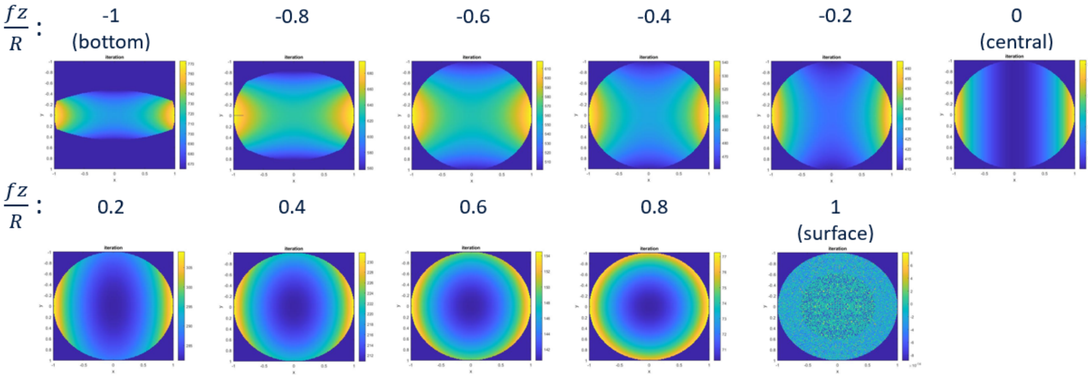

Figure 5.10: Wavefront error focusing at different depth of fibre as a ratio of the radius of fibre.

evanescent field is quite small. The actual working region of the aberration correction required is as shown in Fig. 5.9. The parameters used here are as follows: $NA = 0.5, n_1 = 1, n_2 = 1.46$, and $\lambda = 6.014\mu m$. As discussed in the previous section, for a focus that is further away from the edges of the fibre the iteration method is faster to maintain sufficient accuracy. The wavefront error or aberration while focusing at different depths within the fibre near the centre is plotted in Fig. 5.10. Interestingly, the pupil plane when focusing near the bottom was not fully analysed. This is because the light at a point near the bottom can never reach the pupil plane at certain angles due to total internal reflection. The ray tracing for a focus at the bottom of the fibre is plotted in Fig. 5.11. For a focus position at the bottom of the

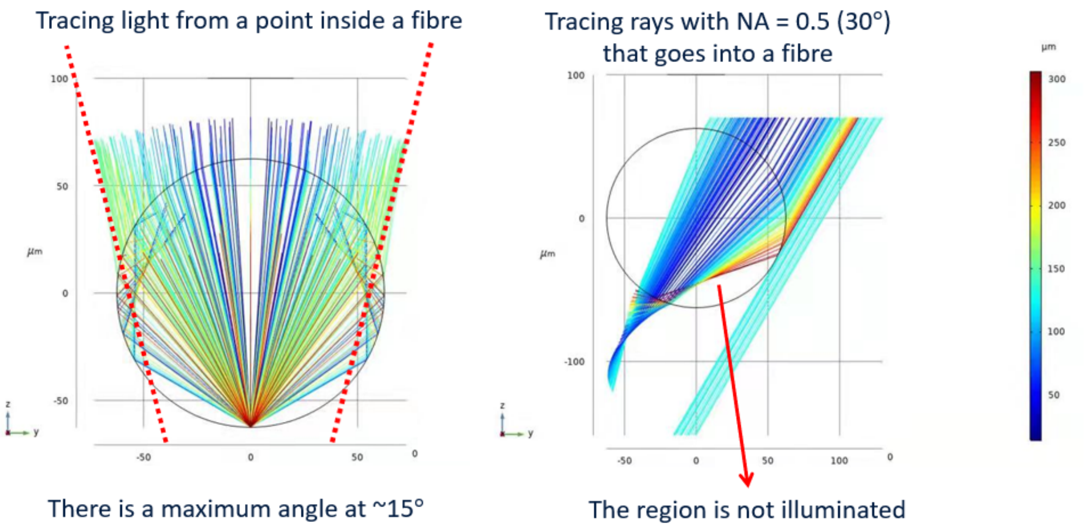
Tracing light from a point inside a fibre

Tracing rays with NA = 0.5 (30°) that goes into a fibre

There is a maximum angle at ~15°

The region is not illuminated

Figure 5.11: COMSOL plot by Tongyu Liu showing why an incomplete pupil plane is viewed by tracing a light from the bottom and tracing parallel rays from the pupil.

fibre, there is a maximum angle depending upon maximum pupil size. For parallel rays heading towards this focal position there is a certain region that the rays at this angle will never reach. Both of these circumstances indicate that with the current parameters the pupil plane at $NA = 0.5$ is not complete near the bottom.

Zernike decomposition of depth

It is easier to program for the laser fabrication system using Zernike coefficients rather than a full wavefront plot. Zernike polynomials are a series of polynomials orthogonal on a unit disc such as a pupil, defined as:

$$Z_n^m = R_n^m(\rho)\cos(m\phi) \qquad if\,even \tag{5.30}$$

$$= R_n^m(\rho)\sin(m\phi) \qquad if\,odd \tag{5.31}$$

where n, m are positive integers satisfying $n \leq m$ and the radial function R_n^m is defined as:

$$R_n^m = \sum_{k=0}^{\frac{n-m}{2}} \frac{(-1)^k (n-k)!}{k!\left(\frac{n+m}{2}-k\right)!\left(\frac{n-m}{2}-k\right)!}\rho^{n-2k} \qquad if\,(n-m)\,is\,even \tag{5.32}$$

$$= 0 \qquad if\,(n-m)\,is\,odd \tag{5.33}$$

The orthogonality is proved as :

$$\int_{\phi=0}^{2\pi}\int_{\rho=0}^{1} Z_i Z_j \rho d\rho d\phi = \pi \qquad if\, i = j \tag{5.34}$$

$$= 0 \qquad if\, i \neq j \tag{5.35}$$

where i and j are index integers given by certain combinations of n and m. The wavefront error ψ, calculated in the previous section, can be written as a sum of the first n terms of Zernike polynomials as:

$$\psi(\rho,\phi) = \sum_{k=1}^{n} A_k Z_k(\rho,\phi) \tag{5.36}$$

The aberration calculated has been decomposed into Zernike coefficients plotted in

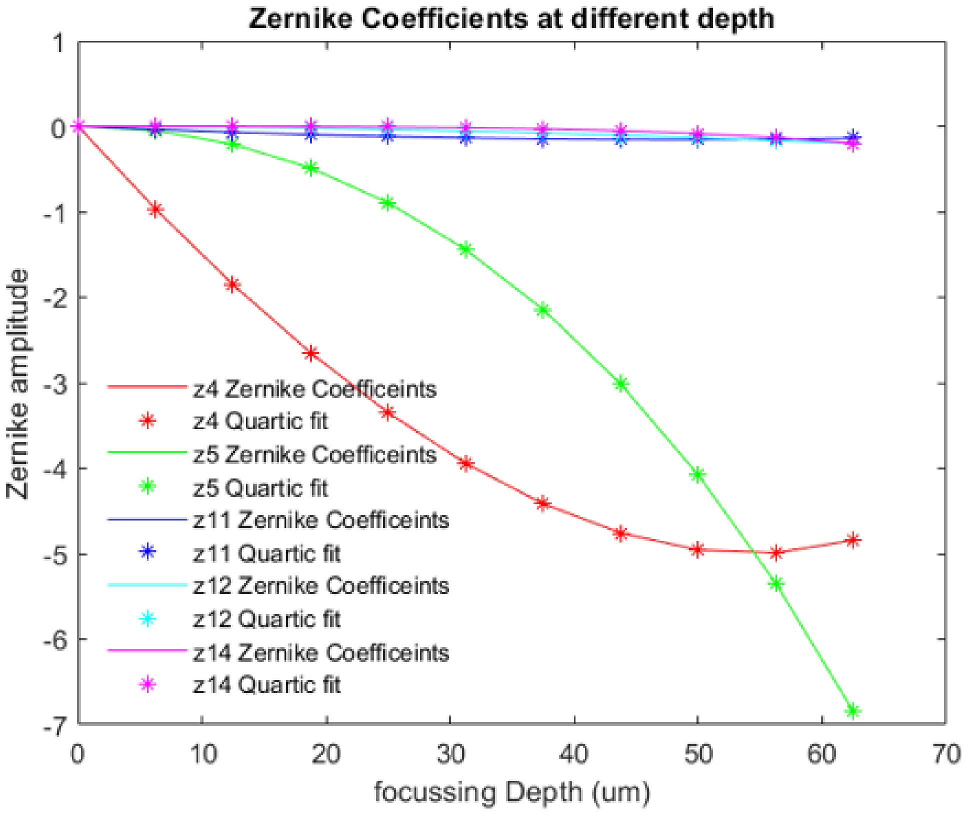

Figure 5.12: Zernike Coefficients when focusing into the fibre at different depths with no y displacement. A quartic polynomial fit was also plotted for better transformation into the actual fabrication parameters.

Fig. 5.12. It is noticed from the figure that the main aberrations here are Z_4 and Z_5 which are known as defocus and astigmatism, respectively. Defocus is more dominant near the surface, while astigmatism is more significant near the bottom of the fibre.

Y shift

Although less useful it is interesting to determine what the aberration looks like at different y. The figures are as plotted in Fig. 5.13. The same plot at the centre of the fibre core is plotted as well. This time, as the focal position is closer to the edge of fibre, it is more difficult to predict the normal unit vector $\hat{N}$. Therefore, the numerical scanning method is more favourable. A similar Zernike decomposition was carried out for moving the focus along the x axis and is plotted in Fig. 5.14. A large amount of tilt is observed because of the asymmetric shape of fibre surfaces moving away from the centre. The light beam from the left side and right side reach the fibre bulk with different normal vector $\hat{N}$. Also a certain amount of defocus and astigmatism should be expected.

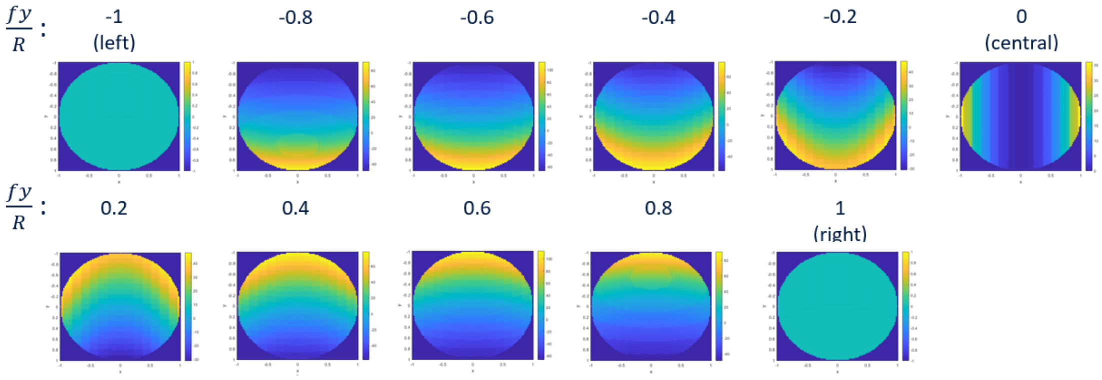

Figure 5.13: Wavefront error focusing at different y position of fibre as a ratio of the radius of fibre.

5.4 Conclusion

In this chapter, there is a demonstration on how direct laser writing with aberration correction can be used to fabricate the designed fibre devices. The first half of the chapter introduces the direct laser writing system with femtosecond lasers including their physics. Then there was a focus on one of the most important steps, the femtosecond laser assisted chemical etching and the optimum set of parameters to use.

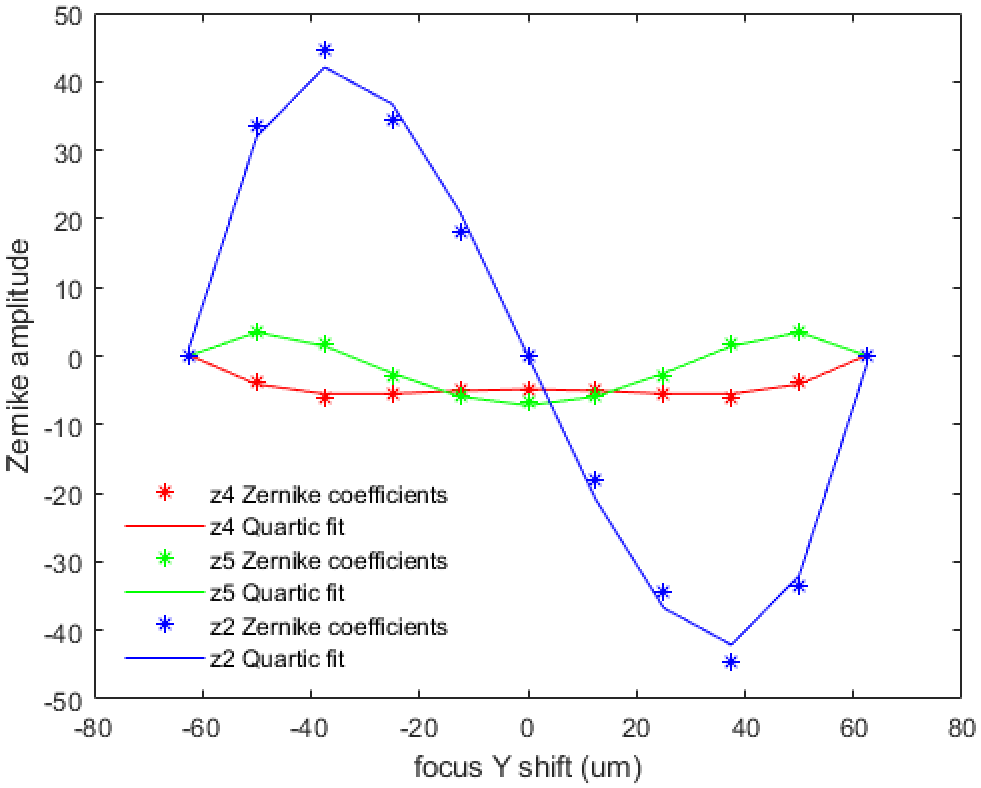

Figure 5.14: Zernike Coefficients when focusing into the fibre at different y shift at the centre depth. A quartic polynomial fit was also plotted for better transformation into the actual fabrication parameters.

The second half of this chapter discussed aberration correction applied to DLW inside fibre. This work was an extension on previous work by investigating the aberration compensation at points over a wide area of the fibre cross-section. The problem has been analysed and different numerical simulations methods given. It was found that different numerical evaluation methods were suitable for different applications depending on the complexity of the geometry. Wavefont errors at different depth and horizontal positions were calculated and decomposed into Zernike coefficients for analysing and laser writing purposes. It was observed that the defocus and astigmatism dominates while focusing at different depth and the tilt is even larger while shifting the focus horizontally.

This chapter provides a foundation for a key step of the whole fabrication process. The unique FBG designs provide the capability for realising novel FBG devices.

6

Fabrication of liquid filled devices

Contents

6.1 Introduction

In this chapter, there will be an introduction to how the liquid filled devices are fabricated. The devices are manufactured from bought-in SMF 28e+ single mode fibre which is readily commercially available. This is transformed into a liquid-filled FBG device. The chapter starts with an overview of the fabrication process, followed by a discussion on each steps of fabrication and this is followed by parameter optimisation for the actual fabrication. The chapter will contain as many details as possible for the future duplication of the work. There will also be some preliminary experimental results that demonstrates the fabrication process.

6.2 Fabrication process overview

The whole fabrication process is as illustrated in Fig. 6.1. The first three steps are laser fabrication processes including FBG formation (Step 2) and nano-pore formations (Steps 1 and 3). Then the nano-pores are etched leaving microchannels (Step 4), which will later be capillary filled with liquid (Step 5).

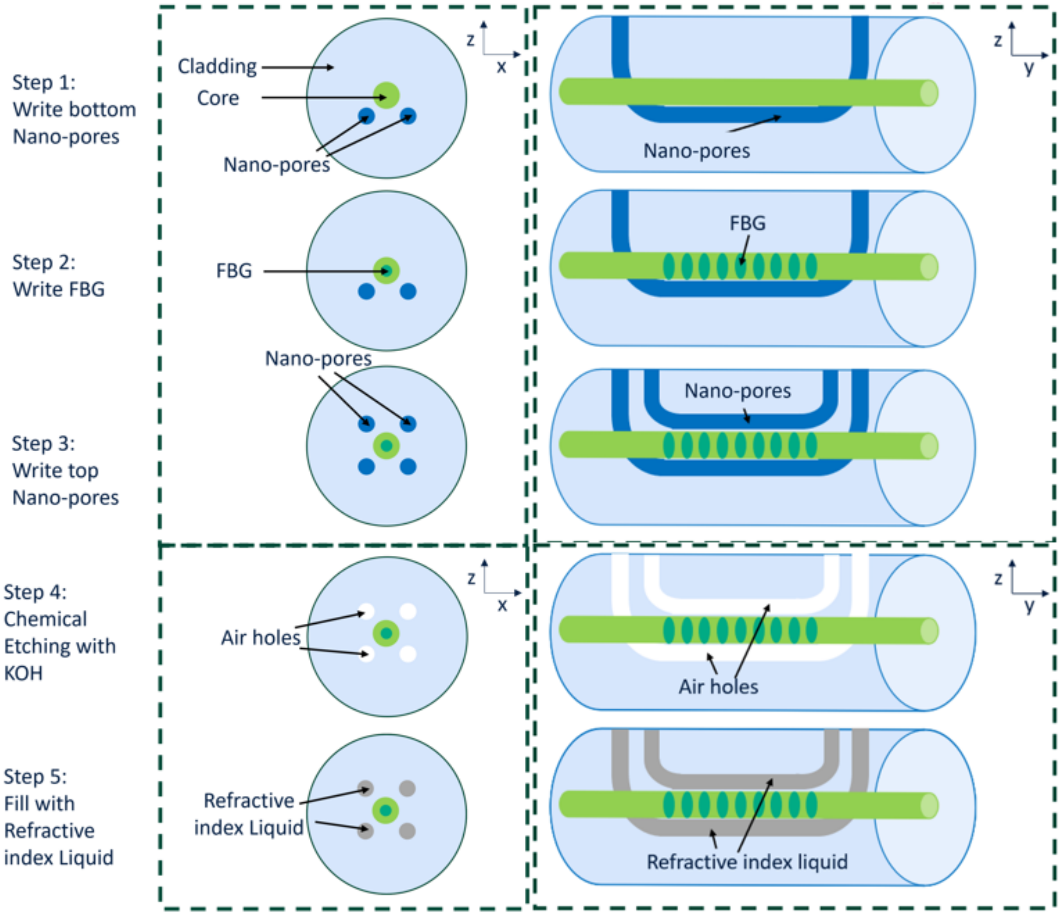

Figure 6.1: The whole fabrication process including FBG formation, microchannel formation, chemical etching and capillary filling.

6.3 FBG formation

The first main step of fabrication is writing the FBG with the femtosecond laser. After stripping off the coating, the aberration correction technique from the previous chapter can be used. The sample is attached to the motion stage with tape and an LED array of a different wavelength to the laser was used to illuminate the fibre core.

6.3.1 Locating the core

The FBG quality is quite sensitive to its position within the fibre core. Principally, the optimised position is to focus at the centre of the fibre core. However, in practice, there are several parameters involving position information that should be taken into consideration.

It is straightforward to find the correct location horizontally. The fibre is uniform along the optical axis so there is no difference in where to focus the light. Care is needed when moving the focus horizontally perpendicular to the fibre optical axis. Fortunately, if the core is visible from the LED illuminated from the bottom, the focus can be located by the position of the core.

Locating the core in terms of depth is more challenging. Here three terms are introduced regarding the depth, take focusing a laser beam on the surface of a glass bulk for example. The first depth information that can be observed is where the surface image is sharp on the camera. As described in the previous chapter, there is an imaging system sharing the same optical path as the laser beam, and this image was used to find the core position in the previous paragraph. The problem is that the imaging system is not always confocal with the laser writing beam. So this position will only be used as an approximate indication.

Given the above reason, a more accurate way of locating the laser depth is to set the laser beam with a slightly lower power so that the glass bulk is not damaged and to observe the reflection pattern. If the laser is focused optimally on the surface there will be an Airy disk pattern with approximately one ring since the laser intensity is quite dim. Instead of imaging of the glass surface, we are imaging the laser focus reflection on the surface. The imaging method of reflected light does not need to consider the difference between the different optical paths but relies on the imaging system, which makes it not an optimal choice. The reason is that different objectives are required for different experiments so the tube lens used for camera imaging is interchanged frequently. Thus it might be worth the time required to adjust them precisely each time. Thus again this indication was not accurate enough. However, it is always a good practice to unify the sharp surface position and the laser reflection position. The process involves moving the tube lens forward and backward and to move the sample up and down until the two positions are in the same plane.

A more accurate way of identifying the depth position was to use a higher power laser pulse energy to be just above the silica damage threshold. The advantage of this method compared with the previous ones is this will no longer require the precision of the imaging system. This means that wherever the tube lens and the camera are placed, the tracks are only determined by the relative position between the laser objective and the sample surface. However, there is also a draw-back that the laser voxel at focus has a certain volume so the tracks will be formed at several different depths. There are two steps to compensate for this effect. The first step is to write tracks at various depths in small increments. Then the thickest track observed is taken to be written on the surface. However, in practice there is always an offset between the thickest track position and the actual focal position. Thus, the next step is to add this offset to the measured position. It is preferable not to damage the sample surface to locate the depth information. Therefore, an additional test on a glass bulk is recommended.

The whole process is demonstrated as follows. Firstly, by moving the sample while looking at the camera, the position of the motion stage z_1 of the sharpest surface is found. Then the laser beam is turned on and a second position z_2 of the best Airy disc image is found. The laser power is increased so that a track can be formed. The third position z_3 is the position where the thickest track is formed. The difference between z_3 and z_2 is recorded as $z_{offset1}$. So that on the actual sample, it is only necessary to measure the position at the best laser reflection image and add $z_{offset1}$ to it. In order to find the second offset this position is used to fabricate some nano-gratings in fibre and glass bulks. By measuring the difference between the actual nano-grating position and the focal position (by cleaving the samples) it was found that this offset seems to be a constant value for the same laser power used, recorded as $z_{offset2}$. Note that although $z_{offset1}$ is imaging system dependent, $z_{offset2}$ is quite constant so it is not necessary to cleave the sample every time. After finding the surface, it is quite straightforward to shift the depth by 62.5 μm which is the radius of standard single mode fibre.

6.3.2 FBG orders

The FBG order is dependent on the quality of light focus. Specifically, it is important to consider the required pitch of the FBGs that can be fabricated. As demonstrated earlier the Bragg wavelength λ_B of an FBG is given by:

$$m\lambda_B = 2n_{eff}\Lambda \tag{6.1}$$

where m is the FBG diffraction order, n_{eff} is the effective refractive index of the fibre waveguide, and Λ denotes the pitch of the gratings. Practically, for a Bragg wavelength $\lambda_B = 1550nm$, the pitch required for first, second, and third order are approximately 0.53 μm, 1.07 μm and 1.60 μm, respectively. Theoretically, the FBG reflectivity decreases with number of diffraction orders [139], which means the first order FBG is preferred. However, practically, the second order FBG often provides the best quality as experimentally demonstrated previously [71]. This idea will be briefly explained here. While the Abbe resolution can be estimated by:

$$\text{Abbe Resolution} = \lambda/2\text{NA} \tag{6.2}$$

where λ is the laser wavelength for the femtosecond laser which is 514 nm, and NA is for the objective which is NA = 0.5 for our system. These give an Abbe resolution of approximately 0.5 μm. This is equivalent to the pitch required for the first order FBG. Therefore, with an ideal aberration correction the first order FBG can be fabricated with high quality, but in most cases second order FBGs are easier to be fabricated. In this work second order FBGs are the primary choice for fabrication.

6.3.3 FBG pitch

According to Eq. (6.1), where $m = 2$, the pitch required for the second order FBG is ≈ 1.07 μm. For the direct laser writing system, the FBG was written by moving the translation stage while turning on and off the pulse picker that control the laser output at a constant frequency. The laser at default is at a repetition rate of 1 MHz. A 0.1071 mm/s writing speed together with 100 Hz repetition rate will give the correct pitch. Thus the pulse picker should operate at a frequency of 1 MHz/100 Hz = 10000 times/s. Other pairs such as 1.071 mm/s together with 1000 shutter frequency could also give an identical FBG. All of the combinations with reasonably low stage moving speed (like < 10 mm/s) would be able to fabricate similar quality of FBGs.

6.3.4 FBG Coupling coefficient

The coupling coefficient of an FBGs κ is mainly determined by the refractive index change δn of the laser modified regions, given by:

$$\kappa = \frac{\pi \delta n}{\lambda_B} \Gamma \tag{6.3}$$

where Γ is the confinement factor of the fibre core. As demonstrated in the earlier chapters the coupling coefficient affects both the reflectivity and the bandwidth of an FBG.

The refractive index modification is directly related to the laser power or the laser pulse energy, which in our system are controlled by a half waveplate followed by a polariser. The difference between the angle of waveplate and the polariser allows a continuous control of the laser pulse energy. The lower limit of the laser power is the minimum by which a track of modified refractive index is formed, which is approximately 0.02μJ per pulse for fused silica. By increasing δn, the increased coupling coefficient will effectively decrease the length of FBG since the majority of light is reflected by the front sections of the gratings. Eventually, at sufficient high pulse energy the FBG will reach saturation. Another upper limit of the FBG writing process is the formation of nano-gratings or nano-pores. They are formed when the energy carried by the spatial resonance is large enough to create explosions on the nano-scale. Among these two phenomenons that limit the pulse energy, it is always the nano-pore formation energy that is reached before the satuation energy. Therefore, the upper limitation of the laser pulse energy is defined by the nano-pore formation energy which is about 0.2 μJ.

Laser power not only affects the coupling coefficient in terms of δn, but also in terms of the confinement factor Γ. This is because the laser focal voxel size is dependent on the laser power. A higher laser power or pulse energy results in a larger radius focal voxel, making the refractive modified region occupy a larger region in the core. Hence the coupling coefficient in fact has a second order effect on the coupling coefficients. In practice, by some iterative experiments, it apears that a pulse energy around 0.13 μJ gives a sufficient FBG reflectivity of $> 10\%$ being far enough away from the nano-pore formation.

6.4 Microchannel formation

Microchannels in this thesis refer to the air holes on a micrometre scale to be filled with the liquid. The microchannels have various of shapes but have general dimensions of ≈ 5 μm in radius and ≈ 5 mm in length consistent with the FBG length. The microchannels should also have entrances to enable the liquid to fill in. In principle, the entrances could be in from the side of the fibre or the cross section of the fibre. However, in practice, filling the liquid from the cross-sections causes extra problems when splicing. Hence all the microchannels have more than two entrances all from the side of the fibre.

Fabrication process

The process of the microchannel fabrication is called ultrafast laser assisted etching (ULAE). A laser modified region is required by employing motion stages. The difference is that a higher pulse energy is used to create nanopores, which are needed for the ULAE process. These allow erosive chemicals such as HF or KOH etch the nano-pores and form microchannels. In order to do this the laser pulse energy should be above the threshold of the nano-pore formation mentioned above. Practically, a pulse energy between 0.26 to 0.29μJ would be sufficient. A higher pulse energy would caused larger laser voxel and modify more region than required, reducing the precision.

In step 4 the fibre sample will be placed in the etchant and heated to 60°C for a sufficient amount of time for etching. The difficulty of the etching process is that the chemical will not only etch the laser modified region but also affect the pristine fibre material, making the microchannel dimensions less precisely controlled. Furthermore, the etching will go through a channel of several millimetres to one direction but only a few micrometers to another. Therefore, it is quite necessary to iterate the laser and etching parameters to achieve the best recipe. The following sections will introduce an optimised etching parameters based on a previous work by *Ross et al.*[103]

Selection of etching material

In terms of chemical selection there are really two candidates, hydrofluric acid (HF) and potassium hydroxide (KOH). KOH was the optimal choice for several reasons. A significant parameter for this process is the selectivity, defined in Chapter 5 as the etching speed of the laser modified region compared with the pristine material. KOH has a higher selectivity of up to 1400[128][126] compared with around 100 for HF[121]. Both can give an etching speed of around 300 μm/hour.

As mentioned earlier, the process requires a fully etched length of several millimetres along the FBG direction while keeping the tolerance in the orthogonal direction to within several micrometres. The selectivity is then required to be at least over 1000. In fact, in the first practical device the microchannls were 3 mm in one direction while 7 μm radius circular cross-section. The waveguide would allow less than 2 μm for over etching thus a selectivity of 1500 must be achieved, which is higher than that of KOH. To solve this problem, an additional entrance was added at the midpoint of the 3 mm length, splitting both channels into 1.5 mm segments. Then the required selectivity is around 750. So in terms of selectivity only KOH satisfies the requirement. Another fact to consider is that

HF poses a significantly higher safety risk compared to KOH due to its highly corrosive nature and potential for severe health hazards upon exposure. HF can cause deep tissue damage, particularly through its ability to penetrate the skin and react with underlying tissues, potentially leading to systemic toxicity and even death. Moreover, HF exposure requires specific treatment protocols, including calcium gluconate therapy, to mitigate its effects [140]. In contrast, while KOH is caustic and can cause burns upon contact, its effects are typically localized to the skin and mucous membranes, with lower potential for systemic toxicity. Proper handling and safety precautions are necessary for both substances, but the consequences of mishandling HF are considerably more severe compared to KOH. KOH was thus selected for the above reasons.

Laser Parameter optimisation

The laser parameters affect the chemical etching process as well. Ideally, only the laser modified regions should be removed and thus several parameters should be kept optimised. Firstly, it is important that the laser polarisation is perpendicular to the laser writing direction. This is due to the fact that the nano-pores formed by the harmonics of the electric field are continuous in one direction while periodic in the other. While moving the focal spot the continuous direction would easily join together leaving 'barriers' if the wrong polarisation is used. This light-matter behaviour restricts the direction of the polarisation to be perpendicular to the laser writing direction. Also the polarisation should be perpendicular to the long axis of the optical fibre to achieve maximum length of smooth nano-pores.

The pulse energy of the laser plays a significant role as well. Within the stated range, the actual pulse energy required is dependent on the repetition rate. The key idea for improving the etching rate and thus selectivity is to keep well-ordered nano-pores. The repetition rate should be kept below 500 kHz and the pulse energy should not be too large to disorder the nano-pores[141]. Practically, a good combination is to use 0.265 μJ pulse energy combined with a repetition rate of 250 kHz.

Etching Parameter optimisation

The etching parameters were based on a recipe given as 12 mol/L concentration of KOH solution combined with 85°C temperature. The upper limit of the concentration was not too significant, as long as the liquid is not too viscous to flow into the nano-pores via the entrances. However, it is important to keep sufficient amount of active KOH molecules in the liquid which restricts the lower limit.

The temperature is a bit more interesting to control. It has been shown that the temperature does not appreciably affect the etching speed of pristine material but does have an effect on the laser modified region[103]. This phenomenon gives us the ability to tune the selectivity for the actual device. For example, if a higher selectivity is required, the temperature should be tuned to be above 85°C while if some over-etching is expected the etching could occur at lower temperatures, which is the reason that 60°C was actually selected for our process. The actual recipe did not give the best selectivity nor etching speed, but was more viable for the specific dimensions of the required microchannels.

The etching time of a specific structure is also significant and dependent on the temperature used. Generally, a longer etching time is to be paired with lower temperature. Hence the challenge is to trade off between these two factors. To find the best combination the etching temperature is kept constant and the etching time was varied. The recipes were different for different cross-section and lengths of the microchannels and can only be predicted within certain limitations.

Over-etching should always be considered due to the intrinsic property of laser assisted etching, especially in smaller dimensions. The laser focus has an intensity variation profile that is graded rather than stepped. Consequently, the selectivity should also vary along the radial direction of the laser beam voxel decreasing away from the centre. Hence, the over-etching could not be entirely eliminated and should always be considered. It was found through experimentation that the etched region should be approximately a factor of 1.5 times larger than the laser modified region observed on a microscope.

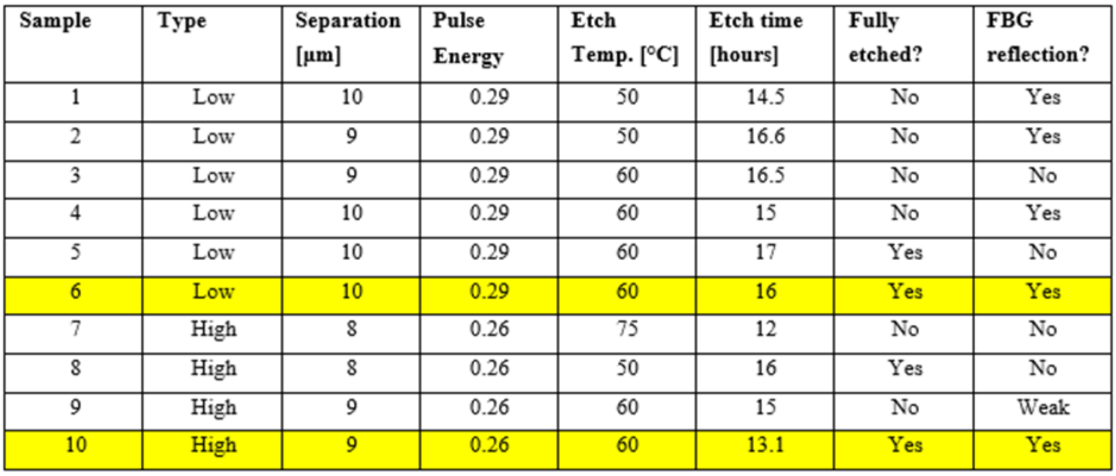

Sample	Type	Separation [µm]	Pulse Energy	Etch Temp. [°C]	Etch time [hours]	Fully etched?	FBG reflection?
1	Low	10	0.29	50	14.5	No	Yes
2	Low	9	0.29	50	16.6	No	Yes
3	Low	9	0.29	60	16.5	No	No
4	Low	10	0.29	60	15	No	Yes
5	Low	10	0.29	60	17	Yes	No
6	Low	10	0.29	60	16	Yes	Yes
7	High	8	0.26	75	12	No	No
8	High	8	0.26	50	16	Yes	No
9	High	9	0.26	60	15	No	Weak
10	High	9	0.26	60	13.1	Yes	Yes

Figure 6.2: The fabrication details of the samples. Each sample is a laser fabricated single mode fiber, prior to filling. Type: indicates if the sample is fabricated for a High or a Low sensitivity device, Separation: The center to center seperation between the channels and the core, Pulse Energy: The laser pulse energy, Etch Temp: The etching temperature, Etch Time: The etching time, Fully etched?: Yes if the channels were etched the whole way along, FBG reflection?: Yes if a Bragg reflection was visible.

The etching parameters of some samples that are close to success are presented in Fig. 6.2.

6.5 Liquid filling

Capillary filling Process

The remaining step was to capillary fill the liquid into the microchannels. Capillary effects, also known as capillary action or capillary force, is defined as a process to passively manipulate liquids. These effects are determined by the interaction between the surface tension of a liquid and the geometry and surface chemistry of the solid support[142]. Capillary filled microfluids are commonly described as 'passive' because they generally lack real-time control over flow, unlike 'active' devices that rely on external peripheral control mechanisms[143]. One advantage of capillary fill over active filling methods is its simplicity and lack of reliance on external power or control systems. Capillary fill utilizes the natural capillary action of the microchannels to draw fluids into the device, requiring only the manipulation of the device's geometry and surface properties. In this section, there will be an introduction to the filling methods.

Initially, the fact that the microchannel geometries were designed with multiple entrances suggests a straightforward method to fill the fibres: confine the liquid to one entrance while keeping the others clear. However, the capillary effect extends beyond the microchannels, affecting the liquid outside the fibre as well. Consequently, there's a risk that the liquid outside the fibre may reach the alternate entrance sooner than its counterparts inside the microchannels. In such cases, all channels become blocked, halting the capillary effect. To address this issue, experiments were conducted at various temperatures to assess whether viscosity could improve the situation. However, only a small, random subset of samples exhibited fully filled microchannels, indicating inefficiency and lack of temperature dependence.

When all the entrances are blocked, an alternative approach was to fully immerse the fibre in excessive liquid. At higher temperature, presumably under low pressure, and after sufficient long time the air gaps inside the fibre core tends to move out of the channel due to the unbalanced pressure. As a result, the microchannels would be well-filled with liquid.

Filled channels

There are several methods to verify if the channels are filled. The most direct method was to observe it under the microscope. As illustrated in Fig. 6.3, at high magnification it is possible to tell the regions of fibre with slightly different refractive indices. Light from the microscope is reflected by the boundaries between the cladding, filled microchannels and the core. The cylindrical shaped core and microchannels also act like micro-lenses that cause the edges to be dimmer than the centre region. Additionally, the image also shows an unfilled region near the entrance which appears as a dark region. This is because the lower refractive index of the air acts like a concave lens that diverges light away from the centre of the microchannels.

Besides, since the FBG devices fabricated were sensitive to variation in refractive indices, the filling quality can be seen in the spectrum. The filling strategy mentioned above was tested. The sample with empty channels was placed at room temperature, fully immersed in excess liquid with a refractive index of 1.43. Reflection spectra were

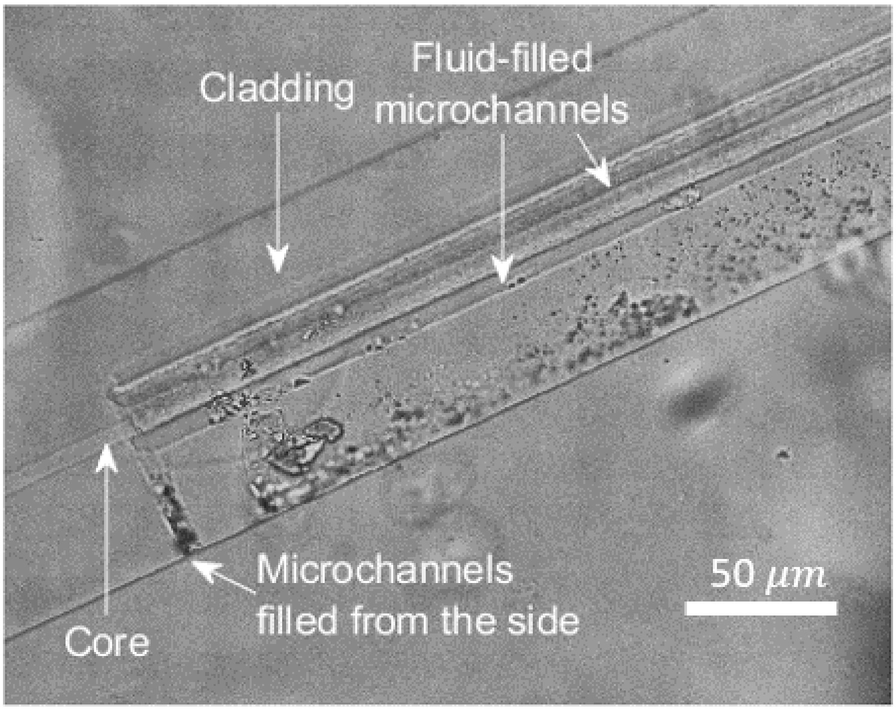

Figure 6.3: A microscope image of a micro-structured FBG device near one end of the microchannels.

measured at 50°C after different amounts of time and these are plotted in Fig. 6.4. Firstly, the Bragg wavelength is different for different filling times. A shorter filling time results in a lower overall refractive index due to the air gaps and thus the Bragg wavelength is shorter. Secondly, the reflectivity is different for different filling properties. For one the propagation mode is affected by the air-liquid boundaries which results in external loss. Also the distorted structure allows cladding (guided by the air cladding interface) causing modal losses. Meanwhile, it is noticed that there is additional Fabry-Perot interference at shorter filling time indicating the existence of air gaps. After 24 hours, the Bragg wavelength seems to be unchanged after longer times. The microscope images also shows fully filled microchannels. These observations serve to validate the effectiveness and reliability of the method.

The samples in Fig. 6.2 are filled with liquid of different refractive indices and presented in Fig. 6.5.

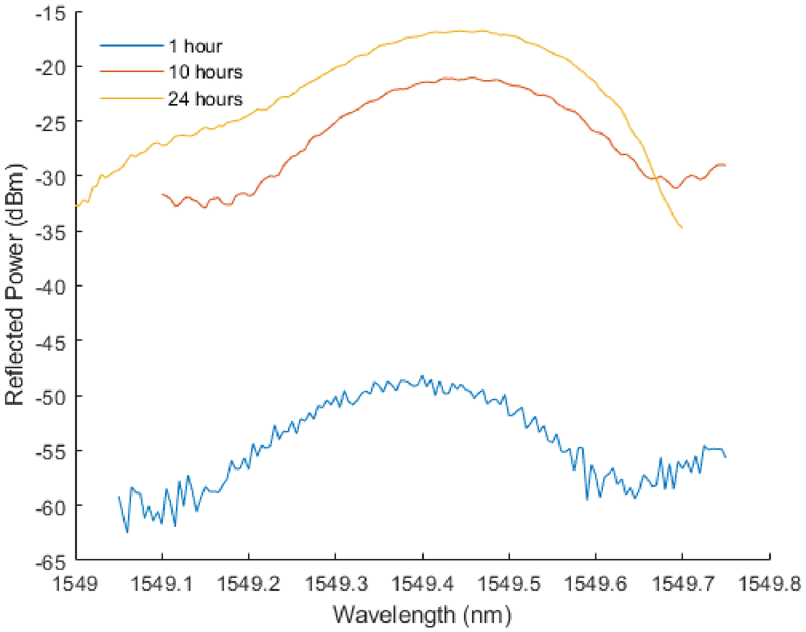

Figure 6.4: Reflection spectrum measured to test the capillary filling effect when immersing the sample in the refractive index liquid at room temperature after different times.

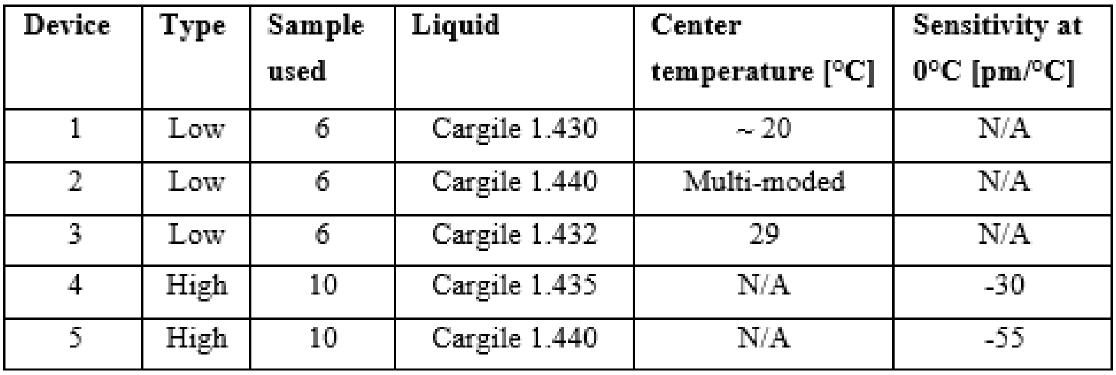

Device	Type	Sample used	Liquid	Center temperature [°C]	Sensitivity at 0°C [pm/°C]
1	Low	6	Cargile 1.430	~ 20	N/A
2	Low	6	Cargile 1.440	Multi-moded	N/A
3	Low	6	Cargile 1.432	29	N/A
4	High	10	Cargile 1.435	N/A	-30
5	High	10	Cargile 1.440	N/A	-55

Figure 6.5: Device performance data. The samples in Table S1 were filled with different liquids and their performance as an FBG sensor was measured. The center temperature is only applicable to the low temperature sensitivity devices. The Sensitivity at 10 °C is only applicable to the high temperature sensitivity devices.

6.6 Apparatus for waveguide characterisation

While a comprehensive introduction to the fabrication parameters has been provided, further tests and investigations are necessary to facilitate iterative improvements. Various tools are available to assess the performance of the fabricated waveguides and ascertain whether similar fabrication parameters should be employed in subsequent iterations. These tests aid in refining the fabrication process and optimizing the functionality of the waveguides.

Waveguide testing

The waveguide testing rig is a standard setup for waveguide characterisation. The sample is placed on a 6-axis motion stage. Light from a tunable laser (Agilent 8164A) is coupled into the sample's waveguide via an optical fibre on a 3- axis stage. Light is coupled out of the waveguide with a 50x objective lens on a 3-axis stage and image onto an InGaAs camera (Hamamatsu C14041-10U).

The waveguide testing rig was mainly used for cross-section investigation of the fibres. The fibres were imaged from the side to examine the quality of the fabrication process and tune the design. In Fig. 6.6 there are some example microscope images of a device design with four side-holes before etching. They were used to determine the optimum laser parameters. The microchannels in the top left figure are smaller than expected, which indicate that the pulse energy used for the laser fabrication was not sufficient. In the top right figure the microchannels are not centred, indicating that the depth was not correct. The dark regions show the paths towards the entrances which are helpful for determining the orientation. The figure at the bottom shows microchannels that are mostly corrected as they have the right sizes and positions.

Refractive index measurement with UV-Vis spectroscopy

In order to measure the refractive index, a known length of cavity of several micrometres is required. The Ultraviolet-Visible (UV-Vis) (Agilent Cary 8454 UV-Vis) spectroscopy is used to measure the thickness of an empty cell. When light propagates through a cell of a certain thickness, reflection will occur at both

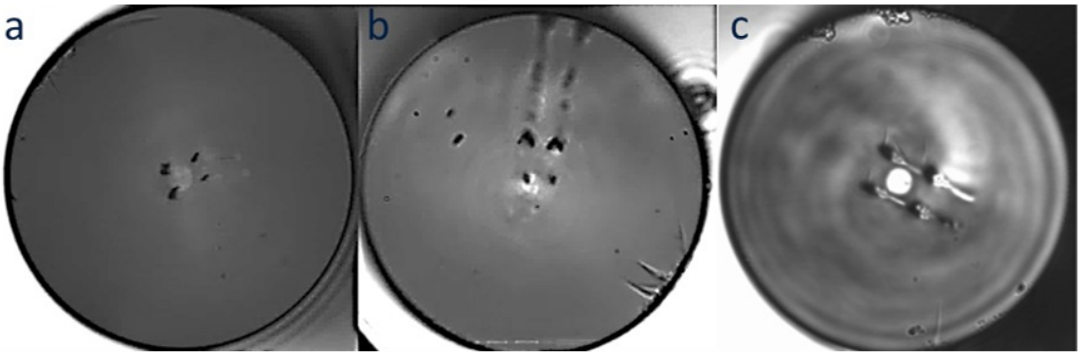

Figure 6.6: Examples of fibre devices with microchannels that have (a) wrong pulse energy, (b) wrong position and (c) correct size and positions. All measured by the waveguide testing apparatus.

interfaces (the air-slice A interface and the air-slice B interface). There will be a phase difference between the two reflected signals, This forms a Fabry-Pérot Cavity. When they are constructive the transmission is maximum and they are destructive the transmission is minimum. The transmission spectrum for an example 5 μm commercial liquid crystal cell is plotted in Fig. 6.7. Each peak in the figure indicates that the thickness t equals to a whole integer of half-wavelength λ, that is $t = N\lambda/2$ where N is an integer counting from zero. It was noticed in the graph there is a bit of noise near the infra-red region. This is probably due to the insufficient time in pre-heating of the UV-Vis.

Given a series of N and λ where peaks occur we are able to find the thickness by calculating the gradient of N versus reciprocal of $\lambda/2$, as the plot shown in Fig. 6.8. A 5μm commercial glass cell was measured and the air gap was calculated to be 4.8400 μm.

Since this measurement uses Fabry-Perot interference which is in fact a measurement of the optical path, this method can also be used for refractive index measurement for a given thickness.

Refractive index measurement

The refractive index measurement of a desired liquid can be carried out similarly using Fabry-Pérot interference. An experiment measuring the refractive index of a 85 % glycerol solution was taken as an example. A commercial cell of 5 μm

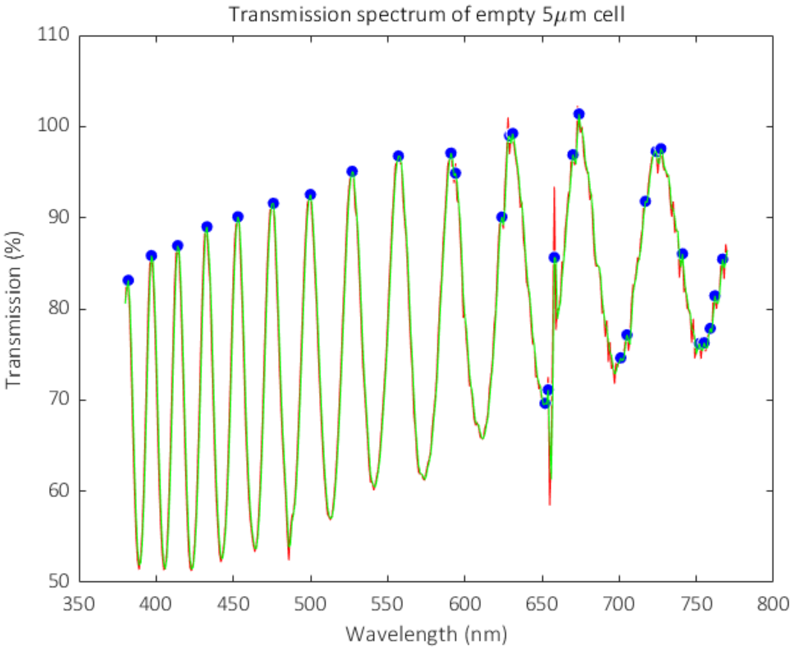

Figure 6.7: Transmission spectrum of an empty 5 μm commercial glass cell. At each peak the thickness d is an integer multiple of half wavelength.

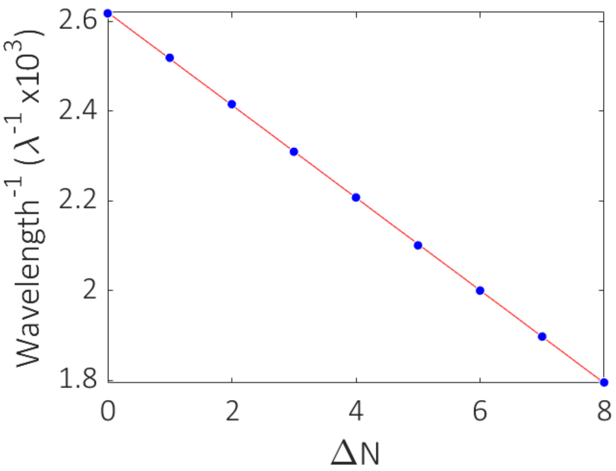

Figure 6.8: Peak wavelength (reciprocal) vs number of peaks.

was used and the thickness of the blank cell was measured to be 5.15 μm. The cell was filled with liquid and the optical path was measured again to be 8.09 μm. The ratio gives the average refractive index of the glycerol solution to be 1.5709 between 400 to 700 nm wavelength. However, according to the published materials the refractive index of glycerol solution should be below 1.47. The error of measuring the thickness is much larger than expected.

Another problem preventing me from using the UV-Vis is that the actual devices are designed for the optical communication wavelengths at around 1550 nm. A tunable laser source is used to scan from 1400 nm to 1620 nm to obtain a similar spectrum with the same commercial cell of around 5 μm. Several trials were made but the frequency for the desired cavity could not be found. A main reason is that at 1550 nm the refractive indices of the liquid to be measured was quite close to those of the glasses of the commercial cell. The precision of the lab experiments was not high enough to tell the difference, not to mention meeting the desired precision of <0.001. For the above reasons, the refractive indices information given by the manufacturers data sheets were used instead.

6.7 Ancillary processes for device fabrication

In additional to the main steps of fabrication, there are also some ancillary processes that are necessary for device fabrication.

Sample preparation

The fibre sample should have no coating on to enable the laser fabrication process. The coating of the fibre samples is stripped off with a stripper of a suitable size followed by acetone cleaning to remove any residuals. The stripped fibre will then be taped onto a microscope slide and placed onto the motion stage.

Fibre cleaving

The sample fibre was cleaved to make a 10 cm section before the process of laser fabrication. Compared with fabrication on a full length of fibre, a sectional fibre is easily handled both on the motion stage or in the etching process. A number of samples can be fabricated in a short time to allow comparison of different laser and etching parameters. Cleaving may also be necessary for observing the cross-sections of the fibres.

The cleaving process is fairly simple, a commercial fibre cleaver FC6RS from SUMITOMO Ltd. was used. A sharp rotation blade was used to create a weak point in the fibre and a mechanical pressure was applied to cleave the fibre. Alternatively, when the fibre length was not sufficient to be placed on the fibre cleaver, a ruby blade can be used to manually create the weak point, followed by pressure cleaving.

The cleaver works perfectly well for a single mode fibre but it is not quite suitable for the laser modified fibre samples with microchannels. Due to the mechanism for cleaving with pressure the structure near the microchannels is often damaged, especially with larger dimension of microchannels. Thus, there is room for improvement using a more precise cleaving method such as laser cleaving[144].

Microchannel refilling

Sometimes a sample is to be filled with different liquid several times to find the optimised refractive indices. This requires a flushing process to remove all the liquid material inside the fibre microchannels. The simplest way is similar to the liquid filling process by fully immersing the fibre samples into volatile cleaning agents such as IPA to sufficiently exchange with the liquid inside the microchannel. Then the cleaning agents can be evaporated by heating under a low pressure. The microchannels can be filled and re-filled a large number of times in practice.

Fibre splicing

Fibre splicing is a process that creates seamless connections between optical fibres to maintain signal integrity. During fibre splicing, two optical fibres are carefully aligned and fused together to form a continuous optical path, ensuring minimal loss of signal strength and transmission efficiency [145]. Various techniques are employed for fibre splicing, including fusion splicing, which involves heating the fibres with an electric arc or laser, causing them to melt and fuse together at the splice point[146]. Fibre splicing is necessary for connection of cleaved samples to a long fibres with connectors.

6.8 Conclusion

To conclude, this chapter has demonstrated a fabrication process for liquid filled fibre devices. All the main steps including FBG formation, microchannel formation and liquid filling have been discussed in detail with sufficient information for future possible duplication. The aberration correction techniques described in Chapter 5 were employed. A recipe for the fabrication of the actual devices will be presented Chapter 7 in relation to the specific devices. The necessary ancillary processes were also described. In addition, there was an introduction of a work on progress liquid crystal alignment experiments, which provided some preliminary results on putting LC into the microchannels.

7
Sensor Evaluation

Contents

7.1 Introduction

This chapter demonstrates novel liquid filled fibre devices experimentally. The chapter starts with a demonstration of apparatus for spectral characterisation of an FBG sensor device. In the second part there will be experimental results of some highlighted FBG devices that gave impressive results using these characterisation methods.

The results in this chapter has been presented in the top international conference, The 28^{th} Optical Fiber Sensors (OFS-28) Conference. I was awarded the Best Paper Award at the conference for my paper titled *Fiber Bragg grating sensors with ultrahigh or ultralow temperature sensitivity'* [147].

7.2 Sensor characterisation

In order to determine the viability of the fabricated devices, they must be experimentally evaluated. Specifically, there are requirements of measuring the transmission and reflectivity spectra at controlled temperatures, strains, and input polarisation.

7.2.1 Transmission and reflection spectrum

The most important part of the sensor characterisation apparatus is the spectrum measurement. To test the FBG, connectorised pigtails were spliced onto the bare fibre ends of the device. A polarisation controller was connected to the FBG. The light source used was a tunable laser (Aglient 8164A). The high coherence source will potentially result in a small amount of Fabry-Pérot ripple on the spectra. For transmission measurements, the other end of the FBG was connected to the optical power meter within the 8164A. Transmission spectra were recorded by scanning the tunable laser in steps and recording the power on the power meter under automatic. To measure the reflection spectrum an optical circulator is used as shown in Fig. 7.1, so that the reflected light can be separated from the input light. The FBG device could be plugged directly from the light source to a photodiode for the transmissive power measurement. By scanning the wavelengths of the laser it is possible to obtain the spectrum for the sensor purposes.

The reflection spectrum, however, needs one more step to accomplish the measurement. An additional equipment such as either a multiplexer or a circulator was used. Among which, the optical circulator is a better choice for a lower signal loss. It consists of three or more ports, with light entering through one port and

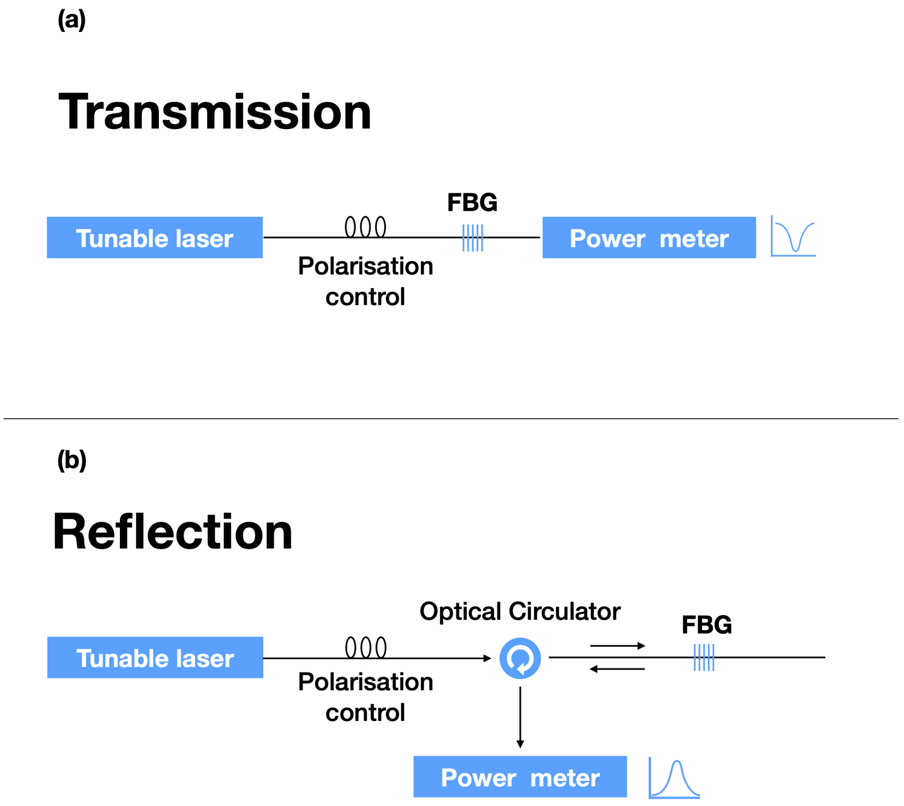

Figure 7.1: System for measuring FBG devices with a tunable laser source and a polarisation controller. (a) The transmission spectrum is measured directed by the power meter. (b) The reflected signal is sent to the power meter by an optical circulator.

exiting through the next port in sequence so that the reflected signal could be measured using the same photodiode mentioned above.

7.2.2 Temperature Control

Since the FBG devices are designed for novel temperature sensitivities, an apparatus for accurate temperature control is required. A temperature controlled mount for the FBGs was therefore designed and constructed. The set up used a temperature controller (Thorlabs ITC4001) together with a Peltier Controller and a negative temperature coefficient (NTC) thermister.

The FBG temperature mount was custom-designed and fabricated by the in-house workshop. The mount was made of two layers of brass metal with 250 μm V-grooves so that the fibre sample could be placed sandwiched in between the two pieces of metal. Another larger groove was used to place the thermister as close as possible to the fibre groove so that the thermister experiences the same temperature as the fibre. The brass metals were placed onto one side of the Peltier module. The bottom end of the Peltier was securely mounted to a heat sink with nylon screws to prevent energy transfer between two sides of the Peltier module. All the components attached were treated with a layer of heat sink compound to ensure good thermal transfer. The temperature controller system can precisely control the temperature to within 0.001°C and the response time was a few seconds.

During the measurements of the FBG spectra, the FBG sample should be immersed inside the same liquid used for filling. This is because as the sample is heated, the thermal expansion effect would drive the liquid out through the entrances. Otherwise when the temperature cools, the amount of liquid remaining will be smaller than initially, causing air cavities inside the microchannels. It is therefore not straightforward to measure the reflectivity at descending temperatures. Thus most results measured in the later sections are with ascending order of temperatures. In a future commercial device, the holes would be sealed, so this problem would not arise.

7.2.3 Strain Measurement

A strain measurement system has been constructed to test the FBG sensors. Two 3-axis motion stages were employed, each with the fibre sample attached at one end, to control the extension of the fibre. This allows the strain to be calculated by the extension over the original length. A challenge was the method to attach the fibres firmly onto the stages without sliding. A simple magnetic clamp does not provide sufficient force to hold the fibre firmly. A super glue would result in destruction of samples. Therefore, the best option was to use some screwed clamps. It was found, however, that the samples were not strong enough to be properly strain tested. Future work will investigate methods of sealing the fibres followed by recoating the stripped fibre, to increase the mechanical strength.

7.3 Experimental Results on Glycerol-filled FBG devices

These two sections present experimental results for selected FBG devices. A demonstration of a glycerol-filled FBG will be provided as an initial stage of the research. followed by FBG devices filled with refractive index liquids. The design process allows great control over the temperature sensitivity with in limits imposed by the material properties. However, the ultra-high sensitivity FBG device and the temperature compensated FBG device are of most interest. There will also be a comparison of the experimental results with the simulation results followed by loss and polarisation analysis.

In the initial stage of experiment an aqueous glycerol solution was chosen for its ease of assess. The refractive indices of the glycerol-water solution can be easily tuned by varying the proportion of glycerol.

7.3.1 First novel FBG device

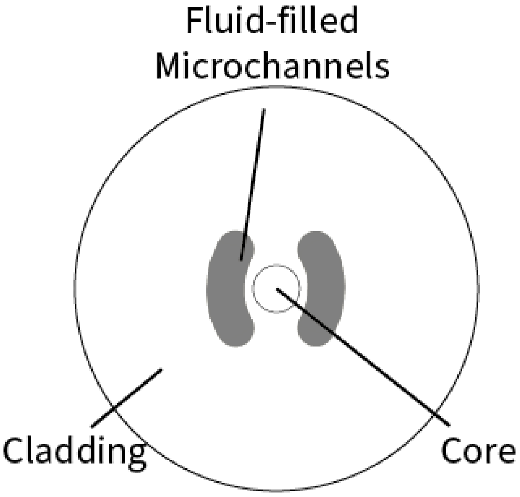

Figure 7.2: The geometry of the first FBG devices that provided novel temperature sensitivities experimentally. The 'kidneys' are filled with liquid materials.

The first FBG device with novel temperature sensitivity was fabricated with a 'kidney' shaped cross-section as described in Fig. 7.2. Several FBG devices with microchannels had been fabricated but none of them were fully filled with glycerol solution, leaving some air gaps that caused multiple peaks in the reflection spectrum. At that time while struggling to fill in the liquid, I was also trying to identify the polarisation dependence of the device experimentally while running the simulations. A kidney shaped sample was easy to fabricate compared with a double bow-tie shaped device because it was simply combinations of circles. So this sample was initially fabricated for polarisation tests where the microchannels are written further away from the core. Occasionally this sample was over-etched, making the microchannels large enough to allow more glycerol solution to be filled in. So I eventually got an optimal sample with sufficiently large area of microchannel cross-section but with the core kept clear from being etched. Meanwhile, the simulation results of this kidney shaped waveguide described in the previous section have shown that this device does not give strong polarisation dependence. All of those reasons led to the first working novel FBG device.

The device was first filled with 85% concentration glycerol solution. The reflection spectra were measured at different temperatures. The liquid was then cleaned out and refilled with 94% concentration glycerol solution and the same measurements were repeated. The spectra is shown in Fig. 7.3. Note that the reflection spectra filled with 85% glycerol solution at some high temperatures became distorted. This was because when the liquid is heated, it expands out of the entrances of the microchannels and leaks out of the fibre device. When the liquid is cooled down some air gaps arise. The air holes have much smaller refractive indices and thus the high contrast waveguide would make the fibre multi-moded, and hence more reflection peaks are observed. This could be avoided by immersing the device, especially the entrances, in the same liquid or by sealing the entrances. It can be seen that these are early forms of temperature-insensitive and ultra sensitive FBG devices.

7.3.2 Comparison with simulations

Besides being the early forms of temperature-insensitive and ultra sensitive FBG devices, a more important role of this first device was to allow optimisation of the simulation parameters. Since the refractive indices of the glycerol solutions were

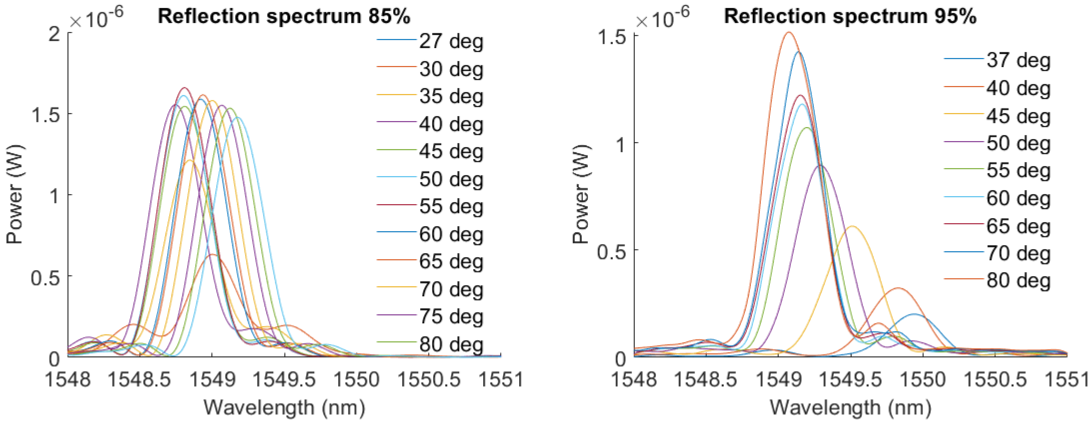

(a) 85% glycerol reflection spectrum **(b)** 94% glycerol reflection spectrum

Figure 7.3: Experimentally measured spectra of an FBG with over-etched kidney shaped microchannels in the cladding filled with (a) 85% concentration glycerol solution and (b) 94% concentration glycerol solution at a range of different temperatures. The core radius is 4.1 μm and the microchannel diameters are about 9μm

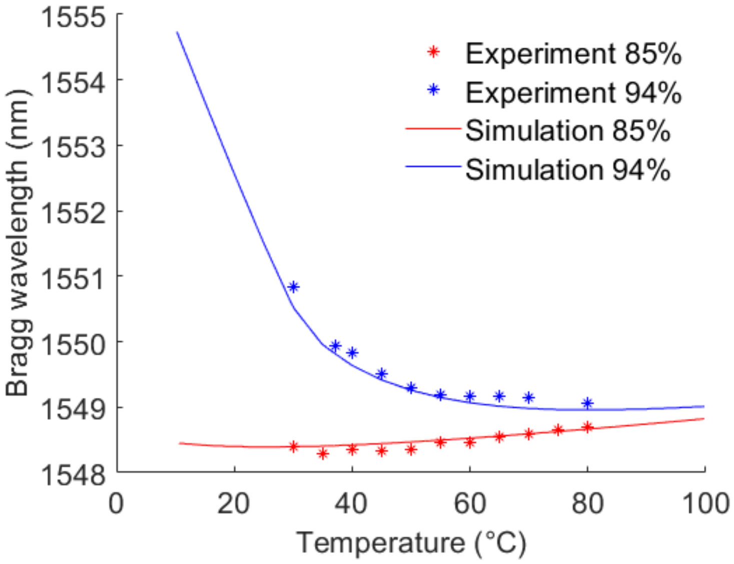

Figure 7.4: Comparison between the over-etched kidney shaped microchannels filled with glycerol solution of two different concentrations. The simulation results are plotted as solid lines and the experimental results are plotted as stars.

precisely known from their concentrations, it was possible to back calculate the exact refractive indices of the fibre core and cladding with the aid of simulations and published measurement data for SMF-28e+. The actual refractive indices of optical fibre are not publicly disclosed and the optical fibre data sheets generally quote a mode field diameter instead. The experimentally measured Bragg wavelengths together with simulation results are plotted against temperature in Fig. 7.4.

The refractive index values 1.451 and 1.444 for the core and cladding, respectively, measured by Wu *et al.* were the most reliable [98].

Although this over-etched kidney device was not optimal for either a high temperature sensitivity device or a compensated temperature sensitivity device, it was an essential step as the design graph presented in the previous section could not have been produced without the work on this sample. The design graph was needed to develop the optimised devices.

7.3.3 Glycerol temperature sensitivity device

Thanks to the development of design graph, it is now possible to design FBG devices with desired temperature sensitivities within specified temperature ranges. Glycerol-filled FBG sensors with novel temperature sensitivities in room temperature ranges are presented in this subsection. Glycerol is non-toxic and non-flammable with a much larger thermo-optic coefficient of $\frac{dn_{gly}}{dT} = -225 \times 10^{-6}°\mathrm{C}^{-1}$[93] than that of fused silica. Furthermore, pure glycerol has a refractive index of 1.4473 at 1550 nm at room temperature [148]. Another advantage is that glycerol can be easily tuned to a lower refractive index by dilution with water to match the refractive index of fused silica, making it easier for designing different devices that meet different requirements.

Here we present the high sensitivity and low sensitivity devices filled with glycerol solution in Fig. 7.5 and Fig. 7.6, respectively. Compared with the device introduced in the previous section, the microchannels in the high sensitivity device was split into four smaller 'kidneys'. Also the microchannels are brought closer to the core. As a result, these microchannels would occupy more area in the evanescent field, and provide more symmetric shape to reduce polarisation dependence. A solution of 90% glycerol concentration was chosen for the high sensitivity device while keeping the liquid refractive index as close to the core as possible. The device becomes multi-moded at temperatures below 24°C and at its temperature sensitivity was as high as -50 pm/°C.

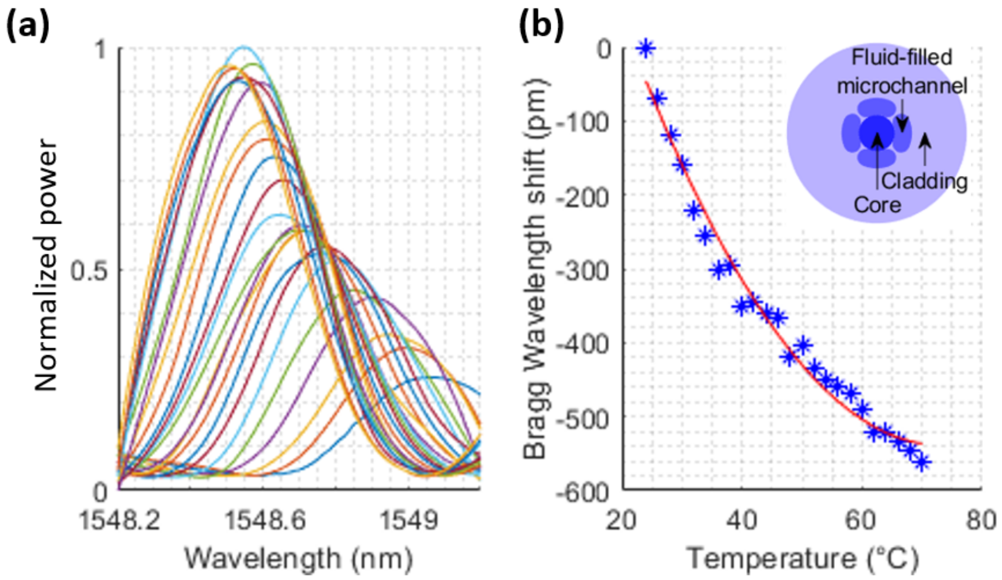

Figure 7.5: A high temperature sensitivity FBG with glycerol filled microchannels (a) the reflection spectrum at temperatures from 22°C to 70°C, and (b) a plot of Bragg wavelength shift against temperature. Inset: the cross-section profile.

For the lower sensitivity device, there are four circular microchannels which are further away from the core to reduce their overlap with the evanescent field and a lower 85% glycerol solution was chosen. In a room temperature range of 14 - 50°C, the overall peak to peak variation in Bragg wavelength was ± 17.5 pm, on average 0.97 pm/°C. This is an order of magnitude less than that of a traditional FBG.

A key disadvantage of glycerol solution, however, is the high absorption at 1550 nm [93]. As a result, the loss of the device was as high as 5 dB at room temperature. Furthermore, as the temperature varies, the mode width of the propagation mode varies accordingly, changing the proportion of power within the glycerol region. Hence, the loss will depend on temperature. The features mentioned above make glycerol devices unsuitable for practical use. Therefore, glycerol was not used in the final device.

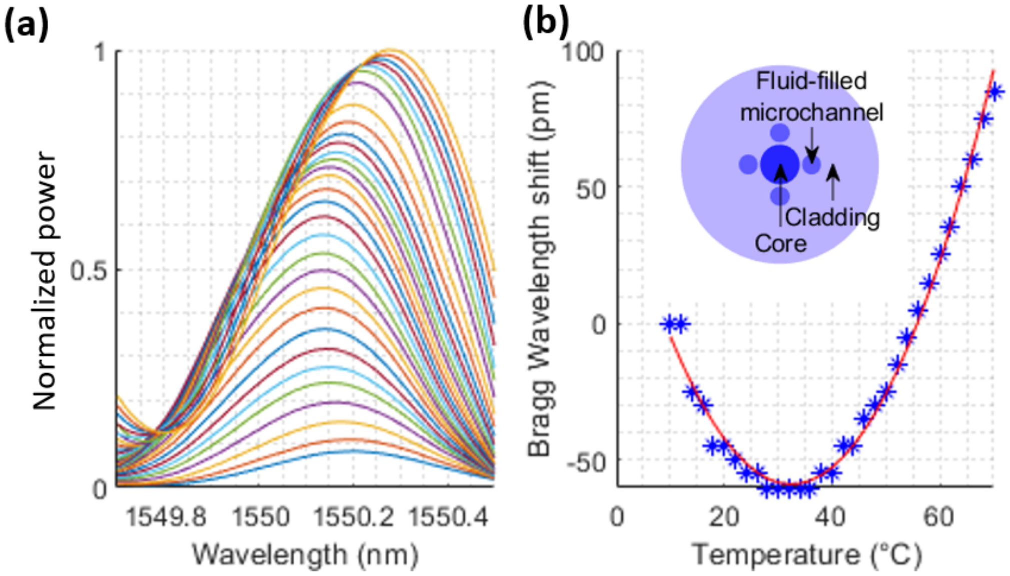

Figure 7.6: A compensated temperature sensitivity FBG device with glycerol filled microchannels. (a) the spectrum of reflection at different temperatures from 10°C to 70°C and (b) plot of the Bragg wavelength shift against temperature. Inset: the cross-section profile.

7.4 Refractive index liquid-filled FBG devices

Given the results for the FBG devices filled with glycerol solution, it was realised that the glycerol absorption could significantly affect the device performance. In this subsection some fully functional FBG devices with specified temperature sensitivities and low losses are experimentally demonstrated.

7.4.1 A high temperature sensitivity FBG spectrum

One motivation for this work is to fabricate a high thermal sensitivity FBG device with low loss that could be used for temperature and strain discrimination. However, to be practical the loss needs to be lower than can be obtained with glycerol. Hence here, specially formulated refractive index liquid with low loss from Cargille Laboratories are used. The highest sensitivity is obtained with the entire evanescent field occupied by the liquid cladding. However, a core surrounded entirely by fluid is mechanically unstable. So some connections are left in between the liquid filled channels as shown in Fig. 7.7.

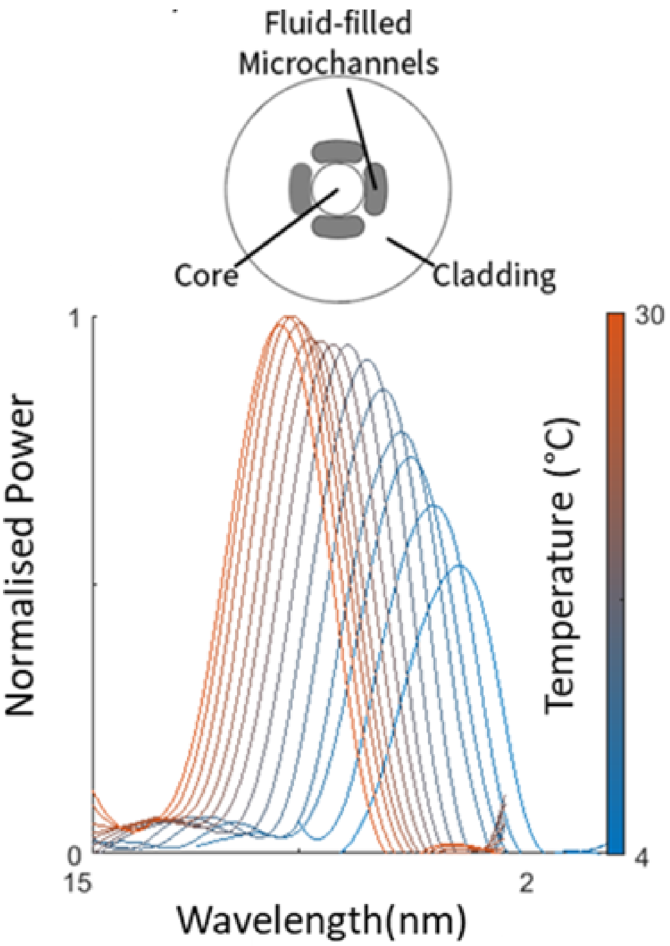

Figure 7.7: Experimentally measured reflection spectra at different temperatures from 4°C to 30°C in steps of 2°C of a high thermal sensitivity FBG device. The device has microchannels filled with refractive index liquid. Inset: the cross-section profile. Each of the four channels are about 7μm wide and 10μm long

Each of the four channels is about 7 μm × 10 μm in cross-section arranged symmetrically leaving approximately a 0.5 μm gap between each other and close contact with the core. A relatively high refractive index of the liquid was chosen to be 1.440 at 1550 nm so that the operating temperature is at room temperature.

The measured spectrum of this device is filtered to remove Fabry-Pérot ripples, and plotted in Fig. 7.7 over the working range of 4 to 30°C. Figure 7.8 shows the peak Bragg wavelength and the peak reflectivity against temperature over a wider range of 4 to 40°C. The bandwidth for the measured spectrum at different temperatures is approximately uniform at 0.5 nm. The maximum temperature sensitivity is as large as -55 pm/°C and over the temperature range of 4°C to 20°C

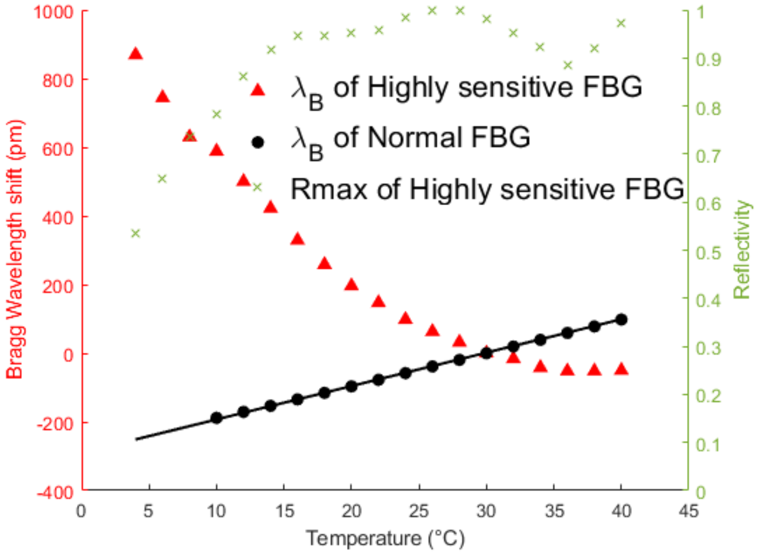

Figure 7.8: Experimentally measured Bragg wavelength λ_B (primary y-axis) and peak reflectivity R_{max} (secondary y-axis) at different temperatures from 4°C to 40°C of a high thermal sensitivity FBG device and a normal FBG for comparison. The device has microchannels filled with refractive index liquid.

the average thermal response was measured to be -42 pm/°C. However, as the temperature increases, the sensitivity tends to reduce in magnitude and move to the positive side. Over the temperature range of 4 to 30°C the average temperature sensitivity within this range is -33 pm/°C.

Generally, the reflectivity is lower at both high and low temperatures. At a lower temperature, the liquid refractive index is closer to the core index. The mode has expanded to the liquid region thus the coupling coefficient is lower. As a result, we expect a high thermal response but a low peak reflectivity. This could be mitigated by writing the grating line through a greater cross-section of the core. As temperature increases, the coupling coefficient gradually decreases, thus the thermal response decreases while the peak reflectivity increases. When the temperature increases further the device will experience loss due to a mismatch in the cladding refractive index, resulting in coupling to radiative modes. This phenomenon is illustrated diagrammatically in Fig. 7.9, where the refractive index profile is plotted against the fibre position on the same graph with the sketched fundamental mode profile, for different temperatures.

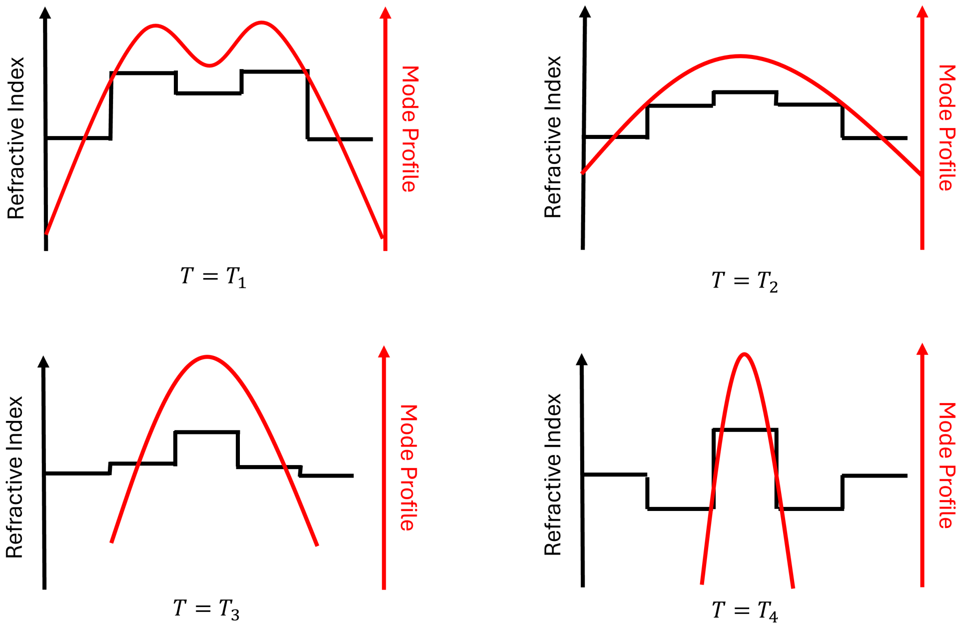

Figure 7.9: Sketch of the modal profile at various positions across the fibre's cross-section on the same graph as the refractive index profile at different temperatures. The temperatures T_1 to T_4 are illustrative and increasing temperature, such that $T_1 < T_2 < T_3 < T_4$.

7.4.2 A temperature-insensitive FBG spectrum

An FBG with a compensated thermal response using the low loss refractive index liquid has also been designed and fabricated. The thermal response has a turning point where the thermal response is very flat. In order to keep a low thermal response near the turning point the liquid proportion in the evanescent field was reduced by moving the micro-channels further away from the core, as shown in Fig. 7.10. The proportion of liquid in the evanescent field is approximately 35% at room temperature. The four channels are circular in shape with a diameter of approximately 7 μm leaving a larger gap of 1 μm away from the core to allow some over-etch. The microchannels are fabricated with a higher pulse energy of 0.290 μJ to overcome the aberration caused by the asymmetric fibre top surface when the focal position is further away from the center. The liquid refractive index was chosen to be 1.432 at 1550 nm so that the device operates at room temperature with zero sensitivity centred at approximately 30°C.

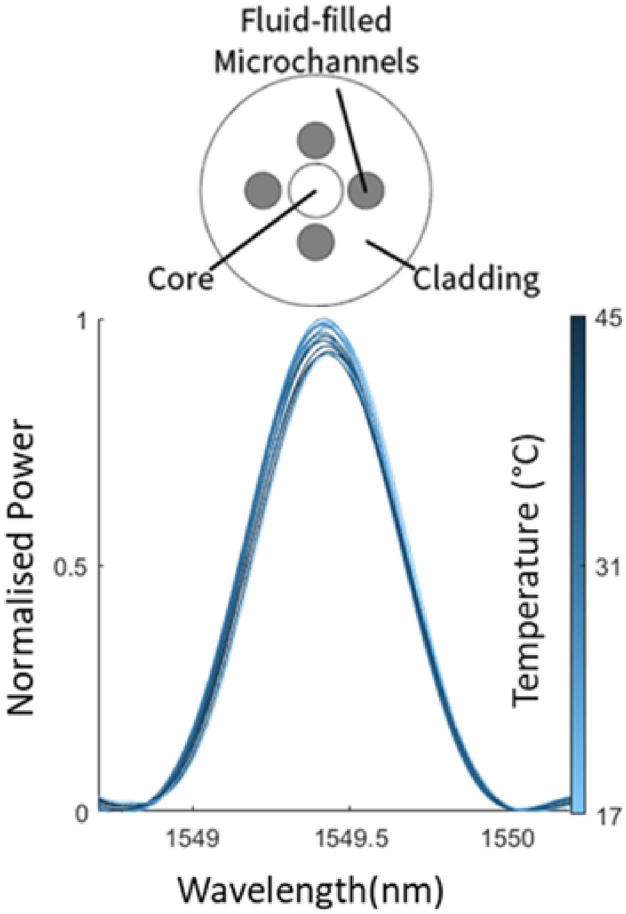

Figure 7.10: Experimentally measured reflection spectra at different temperatures from 17°C to 45°C in steps of 2°C of a compensated thermal sensitivity FBG device. Inset: The cross-section profile. The core radius is 4.1 μm and the channel diameter is about 7μm.

Figure 7.10 shows the reflectivity spectra for the FBG over a temperature range of 17 to 45°C. These spectra show the device to be extremely temperature stable with only ±12.5 pm wavelength variation over this range, which is an 11-fold improvement over a conventional device. Furthermore, there is only 6.9% reflectivity variation, showing the device to be insensitive to both reflectivity and wavelength. The bandwidth is also very constant at approximately 0.5 nm. This is better than the high-sensitivity device since the modes are more confined within the core. The Bragg wavelength and peak reflectivity are shown in Fig. 7.11 over a wider temperature range of 5 to 49°C. This shows the device to be useable over a very wide temperature range, with only ±61.5 pm variation.

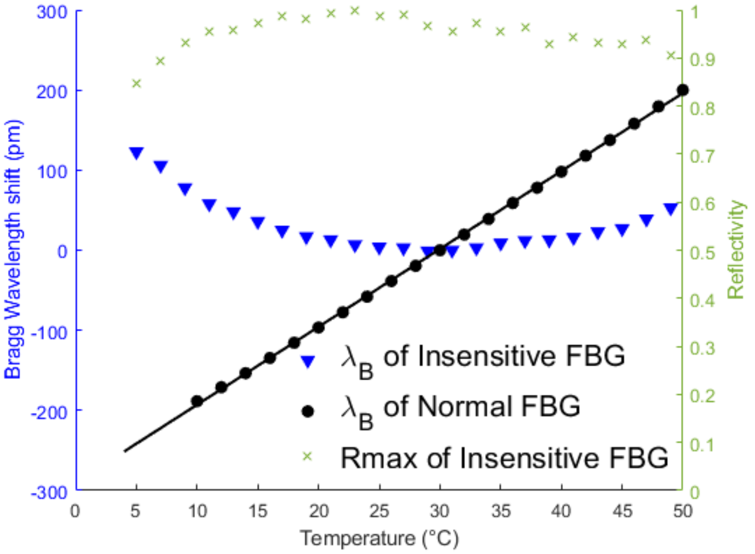

Figure 7.11: Experimentally measured Bragg wavelength λ_B and peak reflectivity R_{max} at different temperatures from 5°C to 49°C of a compensated thermal sensitivity FBG device and a normal FBG for comparison. The device has microchannels filled with refractive index liquid.

7.4.3 Comparison with simulations

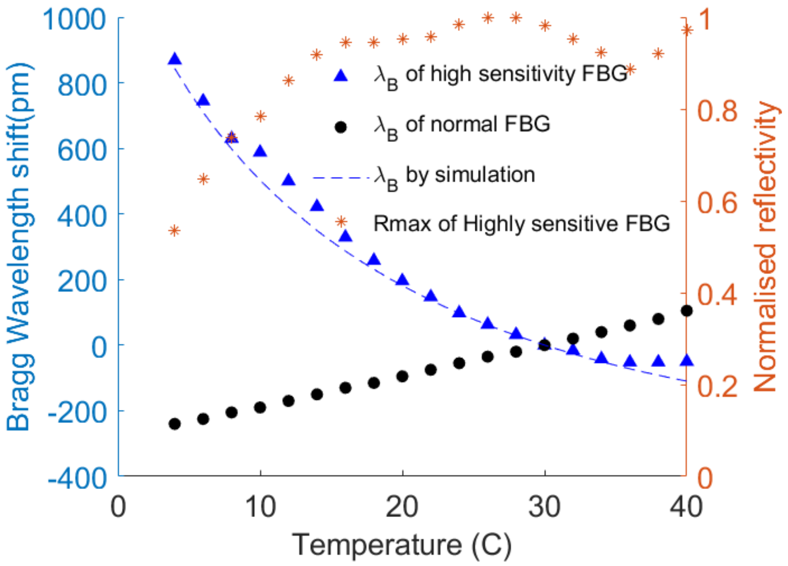

Figure 7.12: Comparison of experimental measured Bragg wavelengths with simulation results of the high temperature sensitivity FBG device. The device has microchannels filled with refractive index liquid. The dashed line shows simulation results.

The exact shapes for the fabricated devices were then simulated to prove the validity of the results. The simulation was using the FEM method from FIMMWAVE

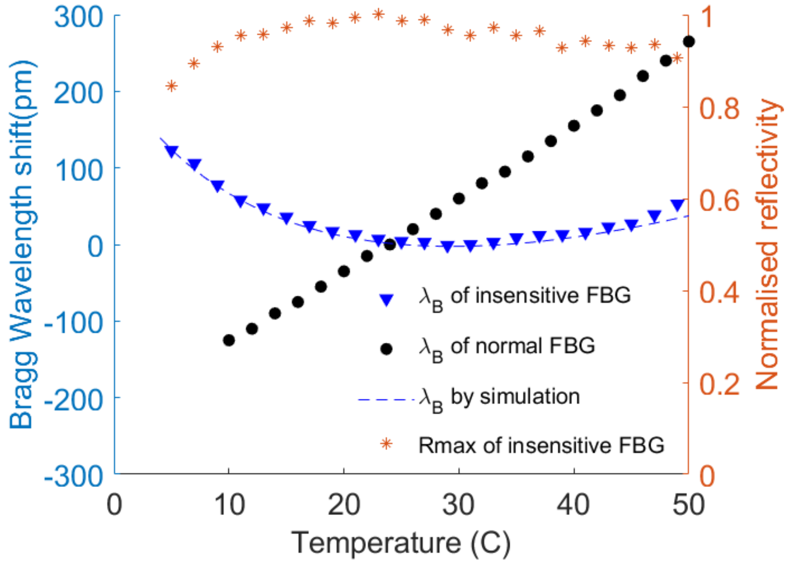

Figure 7.13: Comparison of experimental measured Bragg wavelengths with simulation results of the temperature compensated sensitivity FBG device. The device has microchannels filled with refractive index liquid. The dashed line shows simulation results.

with 120 diagonal elements, 60 modes to obtain the transmission spectrum of the fundamental TE mode. The simulation techniques have been explained in Chapter 3.

The experimental data that plots Fig. 7.7 and Fig. 7.10 are reused in Fig. 7.12 and Fig. 7.13, respectively. Additionally, the simulated results are plotted as dashed lines. The parameters are exactly as designed besides taking into the consideration of over-etching the microchannels. Instead of 7 μm in diameter the microchannels were calculated to have 9 μm diameter to achieve the measured performance. It can be seen that in both cases the simulation results and experimental measured Bragg wavelengths show excellent agreement, indicating the reliability of the method.

7.4.4 Polarisation analysis

The polarisation performance of the temperature compensated device was investigated with the following mechanism. At each temperature, a spectrum is plotted with the test scan. The wavelength is set to be on one side of the peak of the Bragg wavelength. Then the polarisation panels are tuned in order of quarter-wave followed by half-wave, and quarter-wave to achieve a maximum reflection signal and a minimum reflection signal respectively. These two positions are considered as two orthogonal or two extreme polarisations. Spectra of both of them are presented in Fig. 7.14. The spectra show some variation in intensity at different polarisations. The spectra are then re-plotted to reveal the Bragg wavelengths for each polarisation in Fig. 7.15a. The difference in Bragg wavelengths are then plotted in Fig. 7.15b. This shows a maximum of 17 pm in the working temperatures.

While simulations did not show this much birefringence, the polarisation origin was due to the asymmetrical fabrication method using the femtosecond laser. The measured birefringence are comparable in magnitude to FBG devices employing similar aberration correction methods [138]. This alignment is reasonable as birefringence accumulate constructively with each fabrication step. However, unlike a conventional FBG, the differences in Bragg wavelengths are not constant with temperature. As depicted in Fig. 7.15a, the temperature responses for different polarisations resemble those of a device with slightly varied liquid refractive indices. This suggests that birefringence arises not only within the core where the FBG is inscribed, but also due to the non-symmetrical filled microchannels. Future work will be eliminate this asymmetry by improving the fabrication process using techniques such as plane to plane [149].

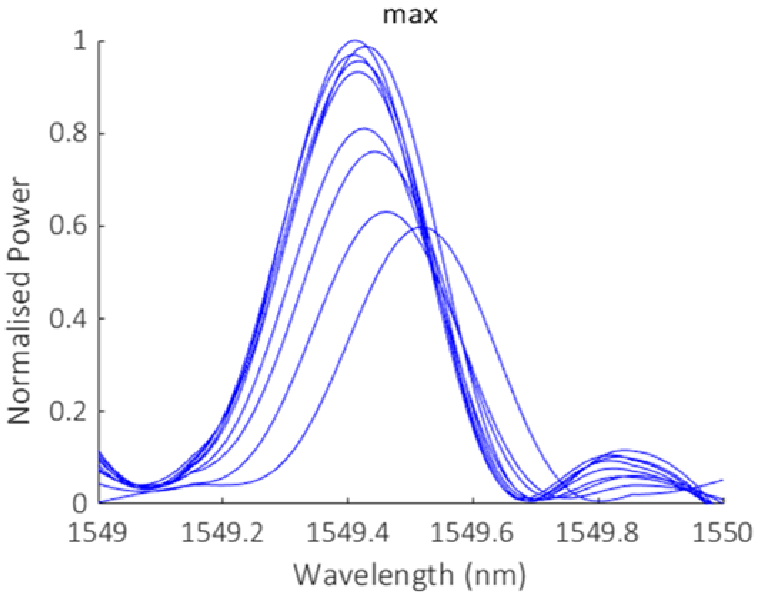

(a)

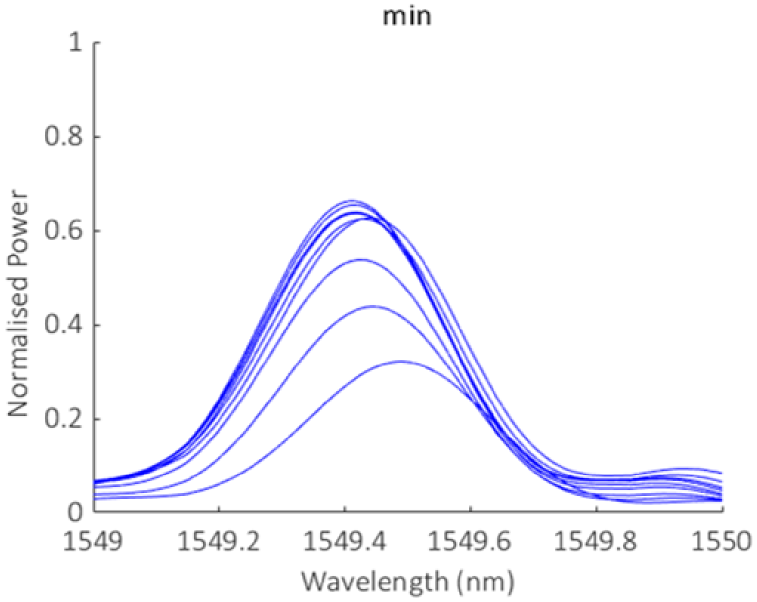

(b)

Figure 7.14: (a) Reflection spectra of the temperature compensated FBG device with one extreme polarisation.(b) with another extreme polarisation.

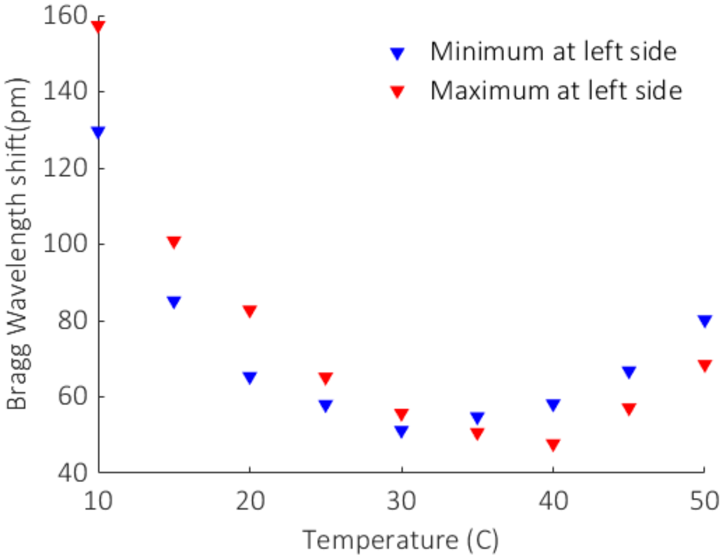

(a)

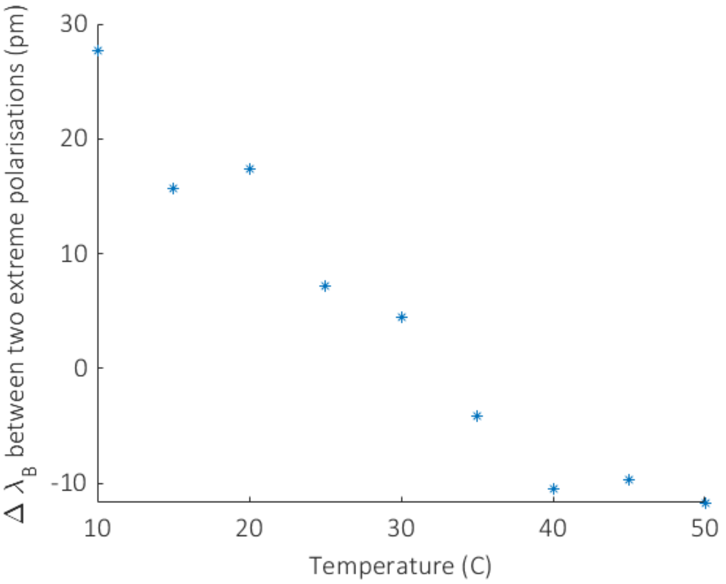

(b)

Figure 7.15: Plot of (a) the Bragg wavelength shift of the two extreme polarisations. (b) the difference in the Bragg wavelength between the two extreme polarisations. Where the extreme polarisations are found by locating the maximum and minimum reflection at a wavelength close to the peak with the polarisation controller

7.4.5 Loss analysis

The fabricated temperature compensated device was spliced to FC/APC pigtails and the insertion loss was measured to be 1.29 dB. The transmission spectrum at room temperature is shown in Fig. 7.16 at an input power of 0.71 mW. The loss was mainly due to the defects during the manufacturing process in either FBG formation or microchannels formation. Among these factors, etching primarily contributes to the loss. During the etching process, damage to the fibre core may occur, and the non-smooth surface of the microchannels can also cause light scattering. The transmission spectrum also shows that the FBG had a reflectivity of approximately 10% indicating that the FBG is still far from saturation.

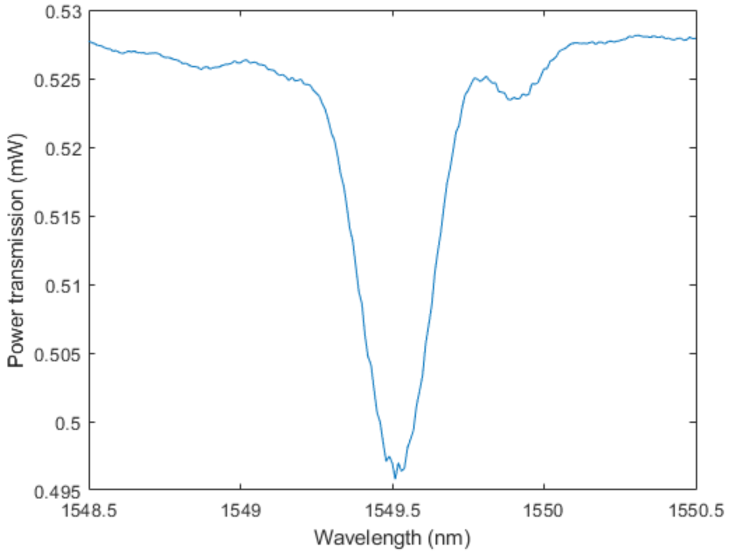

Figure 7.16: The transmission spectrum at room temperature for the temperature-insensitive FBG. The device has microchannels filled with refractive index liquid. The input power was measured to be 0.71 mW.

7.5 Discussions

It is clear from the plots in Fig. 7.7 and Fig. 7.10 that we have tuned the temperature sensitivity to be either very high or very low in a temperature range around room temperature. It is notable that a design with any desired temperature sensitivity in between can also be fabricated. While a large temperature coefficient gives better sensitivity, it also requires more bandwidth for a given operating temperature range, thus reducing the number of sensors that may be multiplexed. Hence having the ability to adjust the sensitivity is a useful design parameter. Meanwhile, the spectra remain single mode with only one peak present. The loss was measured to be -1.29 dB so the devices are suitable for many practical applications. The main source for the losses are defects during the laser fabrication and etching processes which can be improved with better manufacturing. As the device is made of standard fibres there should be no additional splicing nor mode-mismatch losses between dissimilar fibre types. The amplitude is fairly stable for the high-sensitivity device and extremely stable for the temperature-insensitive device in their working temperatures. Glycerol was initially used for the injected liquid, but it was found that the loss at 1550 nm was high and there was a large variation in reflectivity with temperature. Rather than room temperatures, devices could also be designed to have high or low temperature sensitivities for elevated temperatures such as for monitoring lithium-ion batteries.

The applications for the high temperature sensitivity device involve simultaneous strain and temperature measurements by using it in conjunction with a conventional FBG. Each measurement gives two comparable Bragg wavelengths λ_1 and λ_2 from each of the two devices. Therefore, temperature and strain discrimination can be achieved by solving the matrix:

$$\begin{pmatrix}\Delta\lambda_1\\ \Delta\lambda_2\end{pmatrix} = \begin{pmatrix}K_{\epsilon 1} & K_{T1}\\ K_{\epsilon 2} & K_{T2}\end{pmatrix}\begin{pmatrix}\epsilon\\ \Delta T\end{pmatrix} \tag{7.1}$$

where K_{ij} are the sensitivities for strain ϵ and temperature change ΔT for the two FBG devices. The novel FBG device could also be used in thermally-tunable devices such as filters and add-drop multiplexers, where the reflected wavelength is determined by temperature.

The temperature-insensitive device, on the other hand, could be used for strain sensing with low temperature cross-sensitivity, using only a single sensor per measurement. As a result, there is no reduction in multiplexing as the bandwidth per measurement is less than two sensors. Also, there are no additional complicated schemes required and the device can be simply a replacement of existing sensors. Another application is for low-cost temperature stabilized components, such as optical filters, FBG stabilized lasers, and fibre lasers. The temperature-insensitive device would further improve the wavelength tolerance of such devices. The process is compatible with all step-index fibres, such as fibre for 980 nm pump lasers. The temperature insensitive devices would also find application wherever a stable reference is required, such as for spectroscopy instrumentation and optical fibre sensor interrogators.

A future work on these devices is to further control the operating temperature. Developments such as using material with a smaller value of dn/dT and fabricate devices with more precisely controlled microchannel shapes would not only further compensate or increase the temperature sensitivities, but also significantly enlarge the operating temperature to cover more application circumstances.

7.6 Conclusion

This chapter has introduced how novel FBG sensors are measured and developed. The transmission spectra of the FBG sensors were measured with a tunable laser source, and a polarisation controller together with a power meter. For reflection spectra measurement an additional optical circulator is required. The temperature was measured with a temperature controller and the strain was measured with two 3-axis motion stages.

The experimental results started from a coincidence and ended quite successful. It was first believed that glycerol solution was the optimum choice. However, due to the high absorption of the glycerol solution at telecommunication wavelengths the losses and reflectivities have become unacceptable. Even though, there were two novel FBG devices fabricated, one with sensitivity of -50 pm/°C and the other with compensated temperature sensitivity of ± 17.5 pm in a range of 36°C. After realisation The devices were further optimised. The maximum termperature sensitivity was increased to -55 pm/°C and the temperature compensated device has only ± 12.5 pm over a temperature range of 17 to 45°C, which is an order of magnitude less than a conventional FBG. Furthermore, the reflectivity variation was as low as ±3.5% which is far more stable than the glycerol filled devices. The loss was as low as 1.29 dB and the maximum difference of Bragg wavelengths between two extreme polarisations is 17 pm across the operating temperature range.

These devices have the potential to significantly improve FBG laser stabilisation, potentially becoming an enabling technology for strain sensing with minimal temperature cross-sensitivity using existing sensor interrogation systems. Additionally, they are well-suited for applications where tightly controlled wavelength references are required.

The flexible design process allows the temperature sensitivity to be adjusted between +10 pm/°C and -55 pm/°C, with the centre of the temperature range customisable based on the properties of the infiltrated material. This adaptability meets the requirements of a wide range of optical devices and optical fibre sensing applications. Furthermore, this fabrication platform offers the potential for new classes of tunable optical devices.

8

Reinforcement for strain sensing

Contents

8.1 Introduction

This chapter introduces and compares methods of reinforcing the fibre for strain sensing. A bare fibre could undertake strain of approximately 0.01 [150]. But when the microchannels are introduced, the strain limit was measured to be well below this value. Thus a reinforcement should be included before the fibre is used as a strain sensor.

8.2 Treatments to improve mechanical strength

8.2.1 Re-coating

Although we used uncoated fibre, it is also possible to use coated fibre. Potentially it may be possible to write the main structures through the coating and only breach the coating for access channels, or alternatively, the stripped coating may be re-coated. If the fibre has a coating then the thermal expansion of the coating needs to be considered in addition, thus transforming Eq. (2.28) in section 2.5 of Chapter 2 into [151]:

$$\frac{\Delta\lambda_B}{\lambda_B} = (1 - P_e) + [(1 - P_e)\alpha_c + \xi]\Delta T \tag{8.1}$$

where α_c is the thermal expansion coefficient of the fibre coating and P_e is the photoelastic coefficient given by $P_e = (\frac{n_{eff}^2}{2})[P_{12} - \nu(P_{11} + P_{12})]$. In this case $(1 - P_e)\alpha_c$ may dominate over ξ. However, the temperature dependence can be compensated if the fibre can be modified such that ξ is made approximately equal to $-(1 - P_e)$.

The fabrication process is not only suitable for a specific type of fibre but also can be employed for a custom fibre if needed. The process is more viable in terms of manufacturing as the liquid is not easily spilled out because no additional splicing is required. Furthermore, as the shapes of the microchannels can be arbitrary, the etching process also allows tapering of the transition between the fibre with the microchannels to minimize mode loss.

This technique is not limited to the material used in these examples. Potentially a similar process can be used to fabricate fibre devices with active materials such as liquid crystal materials. There is also the possibility of having further microchannels within the fibre for incorporating electrodes to form electrically tunable devices.

Fibre re-coating would be used in future commercial devices. It offers significant benefits in terms of protection, performance, and cost-effectiveness, making it a valuable maintenance technique for ensuring the reliability and longevity of optical fibres in various applications.

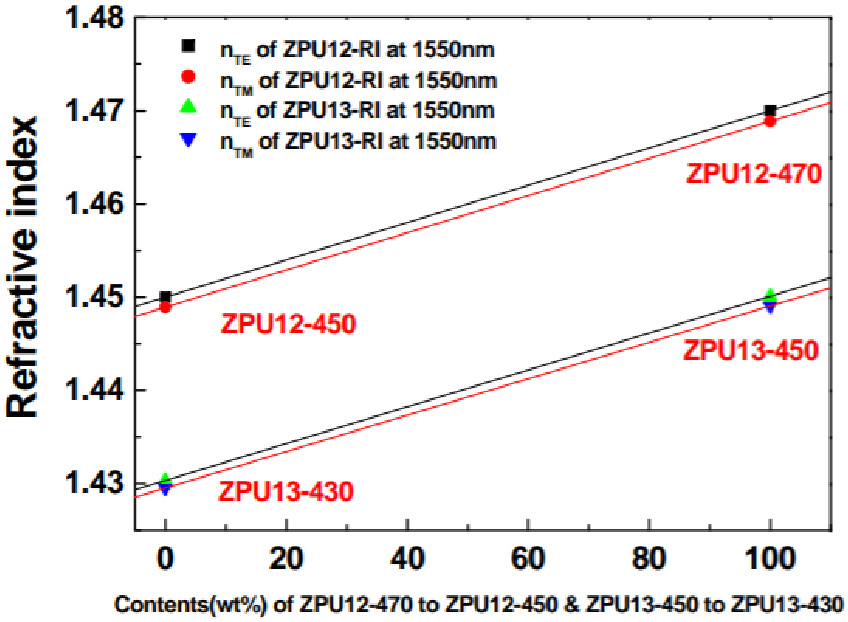

Figure 8.1: Refractive indices of the waveguide resin provided by ChemOptics at different proportion. © Copyright ChemOptics Co. Ltd. Reproduced with permission.

For the re-coating process a commercial fibre re-coater FSR116 from Fujikura was used. The principle of the re-coater is to surround the stripped fibre by polyacrylate which is polymerised under UV light for several seconds. The final thickness of the re-coated fibre will be 280 μm in diameter on top of the 125 μm diameter fibre cladding. An alternative approach is to recoat with polyimide which is only 12.5 μm thick, strong and gives good strain transfer. However, an issue with the current device is that before curing the polyacrylate will move into the microchannels, distorting the effective index of the waveguide.

8.2.2 UV-curable polymers

An improved method is to fill the microchannels with a liquid polymer resin. The resin can then be UV cured prior to recoating. A suitable polymer resin is ZPU13 found from ChemOptics. The refractive indices of this polymer can be tuned precisely by mixing two resins of the same series. The thermo-optic coefficient at room temperature is the same order of magnitude as glycerol and refractive index liquids. The guidance for tuning the refractive indices of ZPU13 is provided in Fig. 8.1.

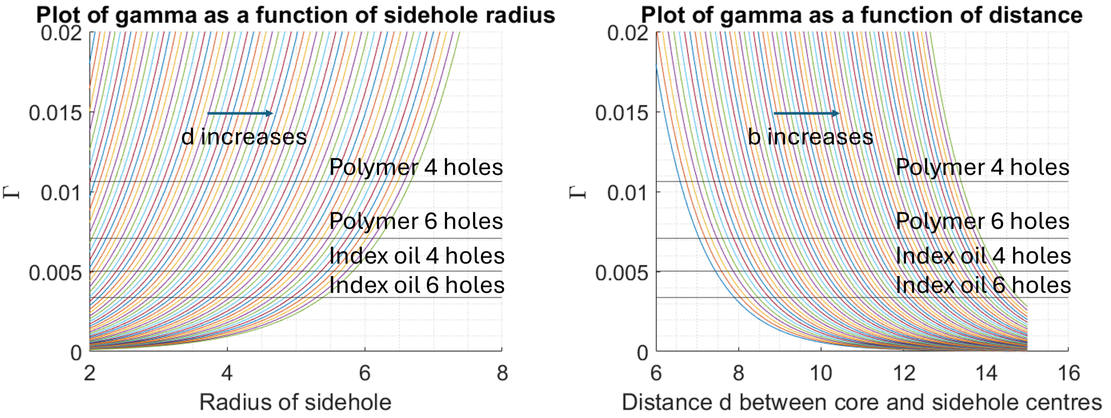

(a) Γ_c against the core radius b. **(b)** Γ_c against the centre to centre distance d

Figure 8.2: Plot of the filling factor Γ_c against several design parameters of a side hole fibre. The curve intersections with each black lines indicates a design of temperature compensated device. (a) Curves plotted against the hole radius b, for different values of separation, $d = 6$ to 15 μm in steps of 0.2 μm. (b) Curves plotted against separation d, for different values of hole radius $b = 2$ to 7 μm in steps of 0.1 μm with the labelled number of holes and material.

8.3 Custom Fibre

Instead of laser fabrication on a standard fibre, using a custom manufactured optical fibre, drawn with the channels already within it, maybe preferable. It may allow tighter control of channel dimensions and more scaleable manufacture. In this section there is an overview of the fabrication techiniques and simulation to give an optimal design for the custom fibre option.

8.3.1 Geometry parameter sweeping

Fibre with circular holes is preferred over other shapes for ease of fabrication. Putting in more side holes is equivalent to increasing the filling factor Γ_c in multiples. For example, a four-holes fibre filled with refractive index oil requires a filling factor of $\Gamma_c \approx 0.005$. Therefore, by sweeping the parameters b, the side hole radius and d, the distance from fibre core centre to the side holes centre, it is possible to predict a series of designs analytically. All the length units used in this subsection are in micrometres. The filling factors of side hole fibres with different parameters are plotted in Fig. 8.2, which has been calculated from Eq. (4.67) in section 4.7 of Chapter 4. Each intersection of a curve with a black line gives a specific design of d

and b. Since the filled material is defined to have the same refractive index as the cladding at the reference temperature, it is possible to conclude that for a given hole radius b there is only one core to hole distance d that gives a temperature compensated device for a given number of holes and type of filling material. It is convenient to use one parameter (for instance d) only to define the specific shape of the side hole fibre. Hence it is necessary to find the relationship between these two parameters. In Fig. 8.3 the hole radius b in μm is plotted against centre to centre distance d in μm for temperature compensated designs. The general trends also make sense that for a larger separation, d, the hole radius tends to be larger for a given material thermo-optic coefficient and number of holes. An immediate concern is that the holes do not overlap with each other or the core.

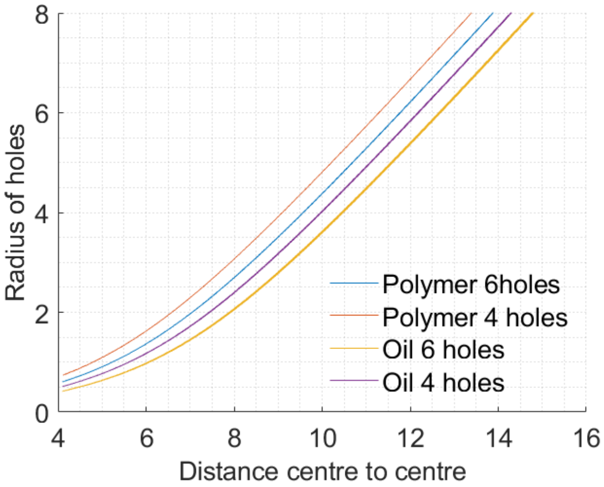

Figure 8.3: Hole radius b in μm plotted against centre to centre distance d in μm for temperature compensated designs with different number of holes and materials.

There are a large number of combinations of the parameters which give a temperature compensated device. The next step is to analyse the performance dependence on those parameters. A way of quantifying the performance is to determine the effective refractive index over a range of temperatures as in the previous designs. It is interesting to investigate how the filling factor varies according to the temperature to verify the above analysis. Designs with several different geometries of 6 holes filled with polymer material of $\frac{dn}{dT} = -180 \times 10^{-6}{}^\circ\mathrm{C}^{-1}$ have been simulated using FIMMWAVE and plotted in Fig. 8.4. By observing the

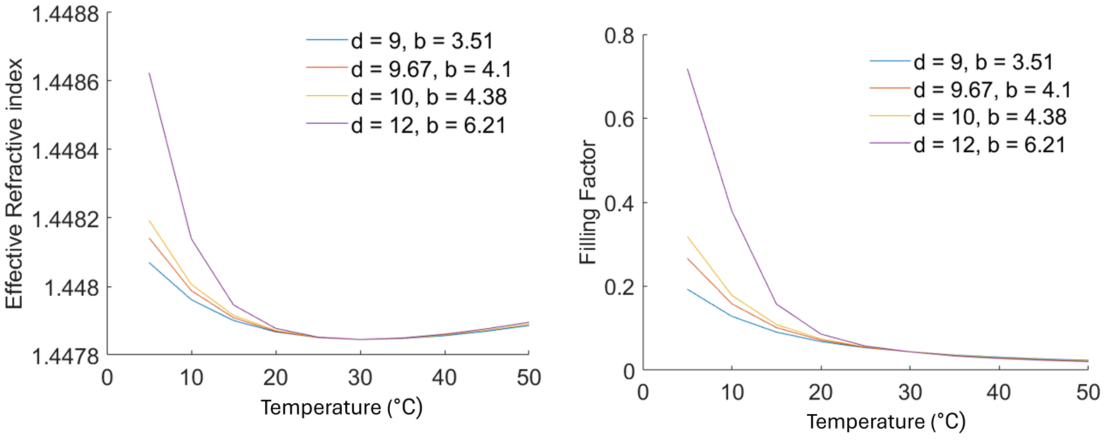

(a) **(b)**

Figure 8.4: (a) Simulated effective refractive index and (b) simulated filling factor plotted against temperature for various of core-hole distances d in μm for a 6 hole design.

effective index profile firstly all the designs have the same reference temperature, which is an evidence of the accuracy of the analysis. Meanwhile, at this reference temperature it is notable that the design with channels having smaller d and b give a more flattened n_{eff} dependence on temperature. For a temperature compensated device, it is therefore more preferable to have a smaller channel with closer distance.

It is also necessary to think about the limitations on the geometry parameters. For example, the holes should not be too large to overlap with each other, nor too close to the fibre core. An analysis has been carried to restrict the parameters. In Fig. 8.5 two different gap sizes are plotted against the centre to centre distance d. Principally, neither of those two gap sizes should drop below zero where an overlap has been observed. In the plot the centre to centre distance starts from 4.1 μm which is the radius of the core. In fact, the centre to centre distance d should be within two boundaries restricted by the two zero-intersection points. From the plot the range of acceptable d is 5.01μm$< d <$ 11.52μm.

8.3.2 Tolerance on polymer

Before reaching final design parameters, it is interesting to find out how sensitive to tolerances the design is. The most uncertain parameter is the thermo-optic coefficient

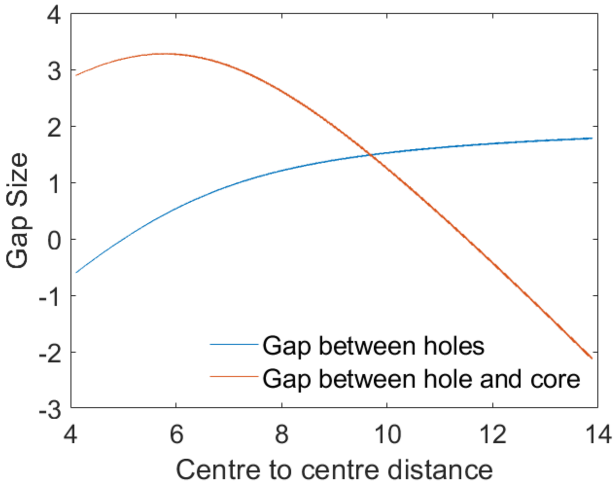

Figure 8.5: The gap between adjacent holes and the gap between the holes and the core plotted against the centre to centre distance d, all in μm for a 6 hole design.

of the polymer, $\frac{dn_3}{dT}$. According to the datasheet, the range of the polymer's thermo-optic coefficients lies between $-150 \times 10^{-6\circ}\mathrm{C}^{-1}$ and $-220 \times 10^{-6\circ}\mathrm{C}^{-1}$. The hole radius b is plotted against the centre to centre distance d for different thermo-optics values within the ranges in Fig. 8.6. The number of holes used in all the designs was 6. Looking at the plot, it is easy to see that a slightly modified design is required for a significant improvement. variation in $\frac{dn_3}{dT}$. Specifically, a larger magnitude thermo-optic coefficient requires a smaller radius of hole or a further distance from the core to compensate.

Another tolerance test was carried out with simulations using a single geometric layout, but filled with polymers of different thermo-optic coefficients. In these simulations a $-40 \times 10^{-6\circ}\mathrm{C}^{-1}$ difference in thermo-optic coefficients shifts the reference temperature by 5 °C. Furthermore, it is found that there is a general trade-off in terms of the design tolerance, given by:

$$\begin{split}\frac{dn_3}{dT} = -40 \times 10^{-6\circ}\mathrm{C}^{-1} \Leftrightarrow \Delta T = 5^\circ\mathrm{C} \Leftrightarrow \Delta n_{polymer} = -0.001 \\ \Leftrightarrow \Delta b = 0.2\mu m \Leftrightarrow \Delta d = -0.23\mu m\end{split} \tag{8.2}$$

The trade-off equation in Eq. (8.2) not only defines how the design parameters affect the final device performance, but also implies that one can use the polymer parameters to compensate the error in geometry designs. This is an important

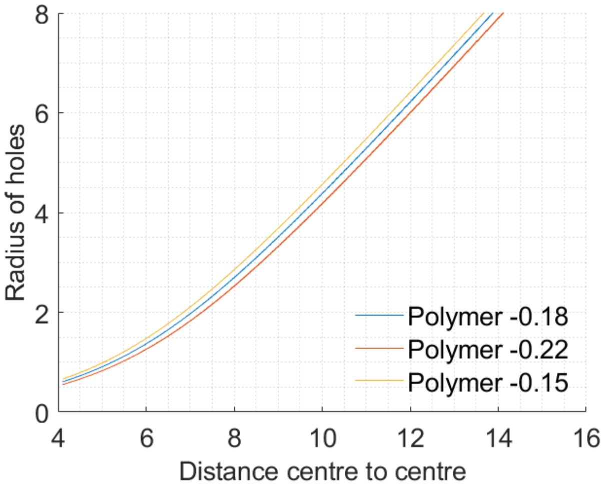

Figure 8.6: Hole radius b in μm plotted against centre to centre distance d in μm for temperature compensated designs with upper and lower boundary of the polymer's thermo-optic coefficients. All designs are with 6 sideholes.

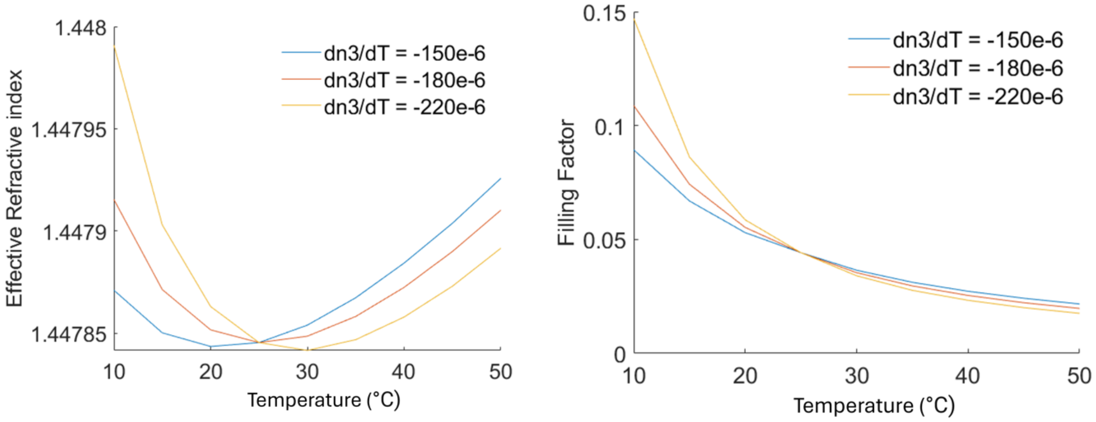

(a) **(b)**

Figure 8.7: (a) Effective index and (b) filling factor plotted against temperature with a design of 6 holes. b the hole radius is selected to be the same as the core radius 4.1 μm.

feature of the designs, making them robust to different manufacturing methods and materials.

8.3.3 An example of design

Based on the waveguide parameters and tolerance simulation here, an example design is presented in Fig. 8.8. In this design there are 6 side holes to reduce the effect of polarisation. The core and cladding parameters are the same as SMF 28e+ standard fibre. The channels have the same dimensions as the core, located

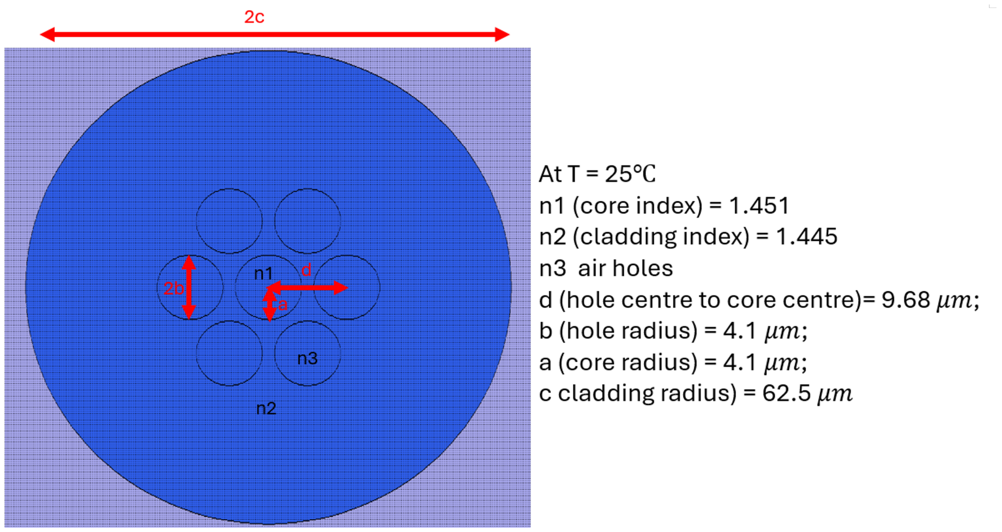

At T = 25°C
n1 (core index) = 1.451
n2 (cladding index) = 1.445
n3 air holes
d (hole centre to core centre)= 9.68 μm;
b (hole radius) = 4.1 μm;
a (core radius) = 4.1 μm;
c cladding radius) = 62.5 μm

Figure 8.8: An example of custom fibre design with six side holes (cladding not to scale).

symmetrically around the core. The hole centre to core centre distance is 9.68 μm. In this example, the geometries are well within the boundaries described in section 8.2. Whatever the variation is in the refractive index of the polymer of dimensional tolerances on the holes are, it is possible to tune the proportions of the resin components to compensate.

8.3.4 Fabrication techniques

Several methods exist for fabricating fibres with precisely controlled air holes such as photonic crystal fibres (PCF) or Hollow core fibres (HCF), including stack-and-draw, extrusion [152], sol-gel casting [153], injection molding [154], and drilling [155]. The stack-and-draw technique, pioneered by Knight et al. [155], is the most prevalent. This method is known for its speed, cleanliness, affordability, and versatility. During the stack-and-draw process, a preform is created by stacking and arranging multiple layers of different materials, typically glass rods or tubes, with precise control over their geometry and composition. The preform is then heated and drawn into a thin fibre while maintaining the desired structure and properties.

The custom fibres have not been fabricated. Figure 8.9 shows the cross-section of the fibre preform while Fig. 8.10 and Fig. 8.11 are microscope images of the actual drawn custom optical fibre.

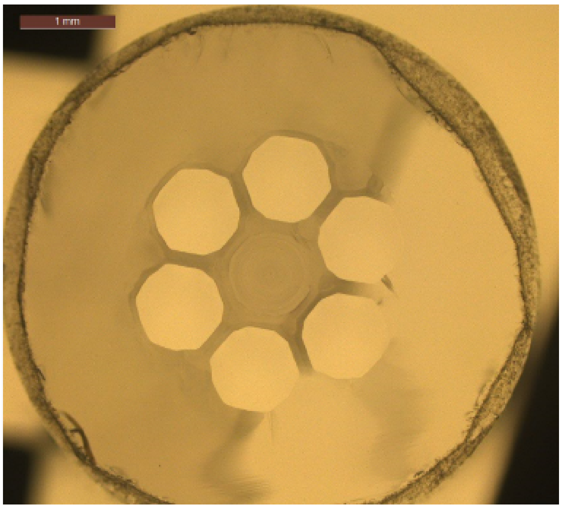

Figure 8.9: Custom fibre preform.

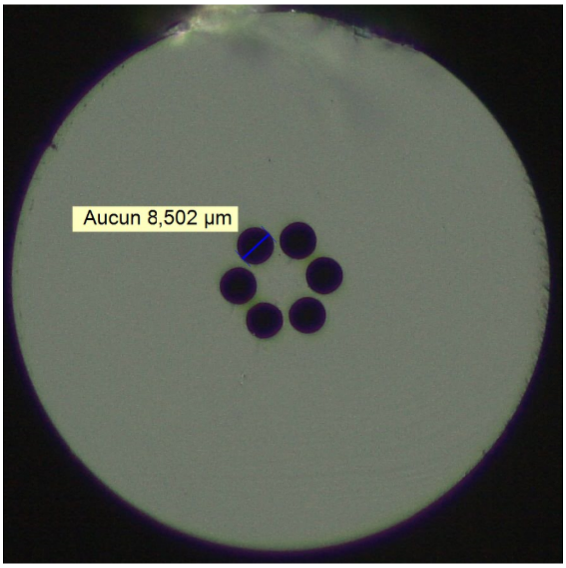

Figure 8.10: Microscope image of the actual drawn custom fibre.

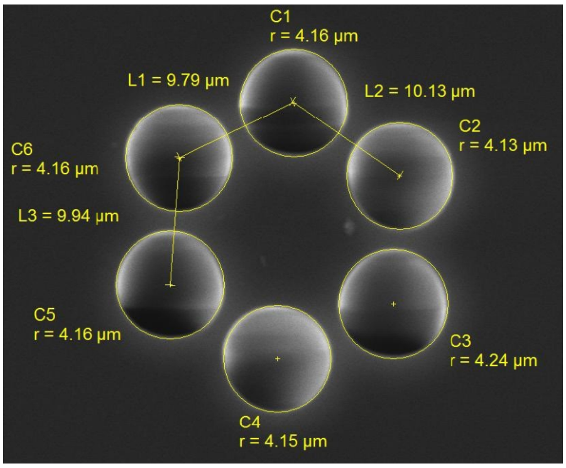

Figure 8.11: Microscope image of the actual drawn custom fibre.

8.4 Conclusion

In this chapter, there has been a discussion on how to improve the mechanical strength of the FBGs. Re-coating with polyacrylate or polyimide would potentially solve the problem. The microchannels can be filled with UV curable polymer resin of the coating material into the microchannels. The second section introduces how a custom fibre could be designed and fabricated. There is a full optimisation of the geometry parameters. The limitations of designing such devices in terms of microchannel overlapping are also discussed. A tolerance test determined that the design was robust to the values of refractive indices and the dimensions of the geometry. Based on the above information there is an example design of such a custom fibre with six microchannels. Finally, there is a brief literature review on the fabrication methods of similar fibres such as PCF or HCF and among them the stack-and-draw method appeared the be the most optimal one. The first designed custom fibre has now been successfully fabricated and is in test.

9

Conclusions and Future work

Contents

9.1 Conclusions

The primary objective of this thesis is to address the longstanding challenge of strain and temperature discrimination in FBG sensors, a problem that has persisted for over 45 years. This thesis extensively explores a novel approach known as liquid-filled waveguides and fibres, providing detailed insights into its implementation. It comprehensively covers all aspects related including design, fabrication, and experimental demonstration, providing a thorough examination of this innovative solution. A distinct technique of aberration correction was introduced to focus the laser beam into the optical fibres during the fabrication process. The significant achievements in micro-engineered FBG devices will effectively address the requirements of various optical devices and optical fibre sensing applications.

This chapter serves as a conclusion of the whole thesis and points out the future work to be accomplished.

Chapter 1 provides a concise introduction to the thesis, highlighting the issue of temperature and strain discrimination in FBG sensors. The chapter briefly discusses the origins and importance of this problem, along with a literature review summarizing previous attempts to address it. Additionally, the chapter outlines the structure of the entire thesis, offering a brief overview of the content covered in each subsequent chapter.

Chapter 2 aims to provide foundational knowledge for a general audience. The chapter starts with an exploration of optical waveguide theories using the ray approach. The waveguide theories serve as a basis for understanding optical fibres—a practical application of waveguides. Various types of optical fibres, classified by refractive index profile and mode number, are introduced, including the specialized Photonic Crystal Fibre (PCF). A comparison is drawn among these fibre types in relation to their behavior as fibre Bragg Gratings (FBGs) and FBG sensors. Additionally, special fabrication and signal processing techniques for FBGs were discussed. The chapter integrates this background knowledge to clarify the importance of temperature and strain discrimination in FBG sensors. Furthermore, an introduction to Liquid Crystals (LC) is provided, highlighting their unique properties such as temperature response, anisotropic characteristics, and sensitivity to external electric fields. Further demonstration of work on LC will be presented in the future plan section.

Chapter 3 compares various simulation techniques. The initial sections of the chapter introduced analytical simulation methods aimed at solving waveguide equations. Waveguide theories were analysed using scalar wave theory, covering simple forms such as step-index planar waveguides, step-index cylindrical waveguides, and double cladding waveguides. Additionally, FBG analysis was included, employing the solution of coupled wave equations to identify key features such as the Bragg wavelength and bandwidth. Meanwhile, various numerical simulation methods are discussed, utilising the commercial waveguide simulation software package FIMMWAVE. These methods, including the film mode matching (FMM) method, finite difference mode (FDM) method, finite element mode (FEM) method, and fibre solver (FS) methods, were compared, revealing the FEM method as the most optimal for 2D simulation. For 3D simulation, the EigenMode Expansion (EME) is recommended to be used together with the FEM. This chapter also included comparative analysis between analytical and numerical methods using two simple waveguides, the planar waveguide, and the cylindrical waveguide. The objective of this comparison was to validate the accuracy of the computer simulation software packages.

Chapter 4 stands as one of the pivotal sections of this thesis, offering crucial insights into the design of innovative FBG devices. The initial exploration into designing such devices primarily focused on achieving consistency among various waveguide geometries. A key concept introduced in this section was the utilization of microchannels within the evanescent field, with research conducted on the effects and quantities of these microchannels through both two-dimensional and three-dimensional simulations. Prior to designing these devices, it was important to establish the requirements. Several important parameters were outlined, including temperature sensitivity, operational temperature range, FBG spectrum, and design implementation. Various types of liquids were investigated and compared, with glycerol solution identified as the most accessible one and used for initial investigations. Refractive index oil was selected to produce high-performance temperature-sensitive products, while polymerisable waveguide resin were marked for future work, taking advantages of their high mechanical strength and electrical tunability, respectively.

In order to meet the device requirements, waveguide and FBG parameters are thoroughly investigated. It was determined that the focus of the design work would center on waveguide geometries, specifically either a double cladding waveguide or a bow-tie shaped waveguide. The former was useful for analytical calculations, whereas the latter was more suitable for fabrication. A design graph was constructed featuring both structures, and further comparison revealed that temperature sensitivity performance is independent of geometry. This notion was further demonstrated during the optimisation process of temperature-insensitive FBG devices. The conditions for achieving temperature-insensitive FBG devices were demonstrated analytically, with two specific shapes solved: FBGs with bow-tie shaped waveguides and FBGs with side hole waveguides.

Chapter 5 introduced the essential component for device fabrication: the Direct Laser Writing (DLW) system. The chapter begins by detailing the system setup, followed by an exploration of the fundamental principles governing light-matter interaction responsible for refractive index modification, nano-pore formation, and laser ablation. Of particular interest is the technique of femtosecond laser-assisted selective chemical etching, with discussions on etchant selection, parameter studies, and early stage trials on etching performance.

Previously, laser fabrication inside optical fibres relied on immersive oil objectives, with drawback that fabrication speed was slow. The latter part of the chapter introduced a novel method of aberration correction using air objectives, with the potential for much faster fabrication. The problem was outlined and supported by background knowledge. Subsequently, a semi-analytical calculation method was demonstrated, enabling precise focusing of a light beam within an arbitrary position within the fibre cross-section. The resulting equations were numerically solved, and phase errors at different positions were graphically presented. Wavefront information was further analysed through the decomposition of Zernike polynomials for experimental validation.

Chapter 6 served as an extensive guide detailing the fabrication process of the designed device. The fabrication process comprised three main steps: FBG formation, microchannel formation, and liquid filling. Each of these steps included full discussions such as material selection, fabrication procedures, and relevant parameter investigations. There were introductions of equipment for waveguide characterization, such as the waveguide testing rig, UV-Vis spectroscopy for thickness measurement, and refractive index measurement setup. Additionally, ancillary processes such as sample preparation and fibre testing preparation were covered.

Chapter 7 presented the experimental setup and key findings of the FBG devices featuring micro-engineered temperature coefficients. The apparatus for sensor characterization was discussed, including equipment for measuring transmission and reflection spectra, controlling temperature and polarization, and imposing strain.

The next section demonstrated FBG devices with micro-engineered thermal sensitivities. A device with a large thermal response has been fabricated and measured to have a near second order thermal response of up to -55 pm/°C near 4°C. It has an average temperature sensitivity of -33 pm/°C over the range of 4°C to 30°C with low variation in reflectivity. The device can be used to produce a large thermal sensitivity compared with a conventional silica FBG sensor to achieve strain and temperature discrimination. Another device has shown an exceptionally low thermal variation of ±12.5 pm over a temperature range of 17°C to 45°C. The device has only 1.29 dB loss and the reflectivity variation with temperature is only ±3.5%. This temperature sensitivity is over an order of magnitude less than conventional FBGs over this range. This device is set to become an enabling technology for strain sensing with low temperature cross sensitivity while using existing sensor interrogation systems. It may also potentially provide a large improvement in FBG laser stabilization. It also has applications where tightly controlled wavelength references are required. The flexible design process allows the temperature sensitivity to be adjusted between +10 pm/°C and -55 pm/°C and the centre of the temperature range to be adjusted within the limits of the infiltrated material. This enables the needs of a wide range of optical devices and optical fibre sensing applications to be met. Furthermore, there is the potential for new classes of tunable optical devices using this fabrication platform.

Chapter 8 explores methods for reinforcing devices for strain sensing. Treatments such as recoating with polyacrylate or polyimide and UV-curable polymers have shown significant potential in enhancing the mechanical strength of existing FBG devices. Alternative approaches, such as using custom fibres, are also considered. Simulations have been conducted to explore the parameter space of these custom fibre designs for a temperature-insensitive FBG device. Different fabrication techniques were compared, with the stack-and-draw method emerging as the most optimal. A full custom optical fibre with microchannels within it has been designed. This was fabricated by a commercial fibre manufacturer using the stack-and-draw technique. The fibre has the potential to enable a scaleable manifacturing process.

9.2 Future work

9.2.1 Strain measurement

The initial aspect of future work entails completing the strain measurement, which could be accomplished in the near future. As of the thesis submission, all equipment has been set up, and some samples are prepared for filling. Once filled and recoated, the devices will be ready for strain measurement on the set up that has been already built. Comprehensive measurements of the FBG spectra under varying levels of strain and temperatures will offer substantial evidence of temperature and strain discrimination.

9.2.2 Liquid Crystal

Another aspect of future work involves the utilization of LC materials, with significant potential for filling the microchannels. However, the primary challenge lies in achieving proper alignment. Some progress has been made in creating alignment within the microchannels, and potential future developments include laser polishing of the inner surface of etched microchannels to facilitate specific alignment. Alternatively, techniques such as photoalignment[156] could be employed to create LC alignment perpendicular to the channel surfaces. In addition to alignment, the electric tunability of LC could be experimentally tested, enabling the fabrication of electrically tunable FBG devices using the same methods.

Liquid crystals (LCs) are a fascinating state of matter that exhibits properties of both liquids and crystalline solids. In a nematic LC phase, the orientation of the molecules are ordered like in a crystalline solid, but their positions are relatively free to move like in a liquid. This unique combination allows LCs to be manipulated by external stimuli such as electric fields, temperature changes, or mechanical stress, resulting in alterations in their optical, electrical, or mechanical properties. In this thesis of liquid-filled fibre devices, LC could be a amazing candidate of the filled liquid for its unique properties.

Anisotropy is a very significant property of LC. An LC molecule is generally in a form of a long chain of carbon atoms, making the molecule absorb quite a large amount of electric field on one direction while less absorbing on the other direction. Take nematic LC for example, which is uniaxial and has positive anisotropy. The direction with a higher refractive index is denoted with a unit vector called the director $\hat{n}$. Light is incident with the optical axis perpendicular to the director and the dielectric tensor $\varepsilon_[ij]$ of this nematic LC is defined as:

$$\varepsilon = \begin{pmatrix} \varepsilon_\perp & 0 & 0 \\ 0 & \varepsilon_\perp & 0 \\ 0 & 0 & \varepsilon_\parallel \end{pmatrix} \tag{9.1}$$

where the z-direction is parallel to the optical axis. The Fresnel equation in Eq. (9.1) can be solved to be:

$$\begin{aligned} n_o &= \sqrt{\varepsilon_\perp} \\ n_e(\theta) &= \frac{n_o n_e}{\sqrt{n_e^2 \cos^2\theta + n_o^2 \sin^2\theta}} = \sqrt{\varepsilon_\parallel} \end{aligned} \tag{9.2}$$

Where the refractive indices n_o and n_e are defined by the incident light wave as follows [157]. When a linearly polarized wave travels perpendicular to the optic axis and its electric field aligns parallel to the optic axis, it experiences a refractive index denoted as n_e, and is termed as the extraordinary wave. Conversely, if the electric field vector is perpendicular to the optic axis, the wave encounters a refractive index denoted as n_o, distinguishing it as the ordinary wave. While when the electric field vector forms an angle θ with the optic axis, the wave undergoes a phenomenon known as birefringence, causing it to split into two waves travelling at different speeds. This optical anistorpic medium can be defined with the difference in refractive index Δn defined as:

$$\Delta n = n_\parallel - n_\perp \tag{9.3}$$

where $n_\parallel$ and $n_\perp$ are refractive indices in the orthonogal polarisations.

The director $\hat{n}$ can be controlled by a various of methods to align the molecules of LCs as they are critically determined by the surface treatments. One technique involves physical rubbing of alignment layers, typically composed of polyimide, to create unidirectional alignment through frictional forces [158]. Another approach utilizes photoalignment, where photoactive materials induce molecular orientation according to specific light patterns, offering precise control over alignment [159]. Mechanical shear can also be applied to induce alignment [160]. Recently, the development of LC aligned by nanoparticles has attracted attention from the relative fields [161]. In this work, it is useful to determine the suitable LC alignment methods when filled in microchannels.

An important feature of LCs is that they are sensitive to external electric field, due to their molecular structures. When an external electric field is applied, a nematic LC phase with positive anisotropy tends to align its director parallel to the electric field while one with negative anisotropy tends to align its director perpendicular to the electric field. This electrically induced tuning capability finds extensive applications in various fields, including LC displays, adaptive optics, optical switches, tunable filters, beam steering devices and many others. The ability to rapidly and reversibly modulate the optical properties of LC materials through electric fields underscores their significance in modern photonics and optoelectronics, enabling versatile and dynamic control over light propagation and manipulation. One of the aims for the future work of the liquid filled device is to make electrically tunable optical devices mentioned above in optical waveguides and fibres.

Use of liquid crystal (LC) would introduce another degree of freedom that enables the development of electrically controlled devices. Works with LC-filled fibre devices were reported including selectively LC-filled Photonic crystal Fibres [162], LC-filled D-shaped fibre sensors [163], and LC-filled hollow-filiment FBGs [164]. However, no alignment of LC has been reported in those micro-structures, which means the devices are not able to be significantly tuned electrically. Alignment of LC in silica bulk was reported in micro-capillaries [165] and in nanostructured indium tin oxide (ITO) [166], but it is still a huge challenge to achieve the same alignment in microchannels within optical fibres. The design and the experimental realisation of electrically tunable LC-filled device is an interesting task for the future.

Microchannels fabricated by chemical etching

Some microchannels were written in glass substrates to enable LC alignments. The channels were laser fabricated and etched with exactly the same parameters to obtain a similar structure as the microchannels inside the fibres. Then the microchannels were filled with LC and photos under two crossed polarisers were taken at different angles, as shown in Fig. 9.1a. It is noticed that the intensity in most of the regions are not angle dependent but there is a slight periodic variation in a certain region. This region was further magnified to 50× as shown in Fig. 9.1b. Both figures have shown that there might be some surface alignment when the channels are thin enough, indicating that there is a certain pattern of surface texture caused by etching. It was an interesting discovery but not quite sufficient for practical use.

Microcells fabricated by laser ablation

An alternative method is to create alignment directly by laser ablation. The following work was an emulation of previous work by Liao *et al.* in which some LC alignment micro-cells has been achieved [167].

Laser ablation requires higher pulse energy and hence lower repetition rate for a same output power. The Pharos femtosecond laser were tuned to be optimised for 120 kHz and 3 μJ. The laser focus starts from the inside of the glass bulk near the surface and gradually ’pushes’ the debris outside. Two different writing methods are used where one of them has the writing direction perpendicular to the laser polarisation and the other parallel.

The sample was filled with LC and observed under crossed polarisers, as shown in Fig. 9.2a and Fig. 9.2b. Despite of the fact that the cells were not well-filled due to the poor quality of fabrication, both of them have shown some surface texture that causes LC to align. The cell fabricated with perpendicular laser writing direction and laser polarisation direction tends to show more variation in intensity at different angles. This indicates that the surface structure caused by

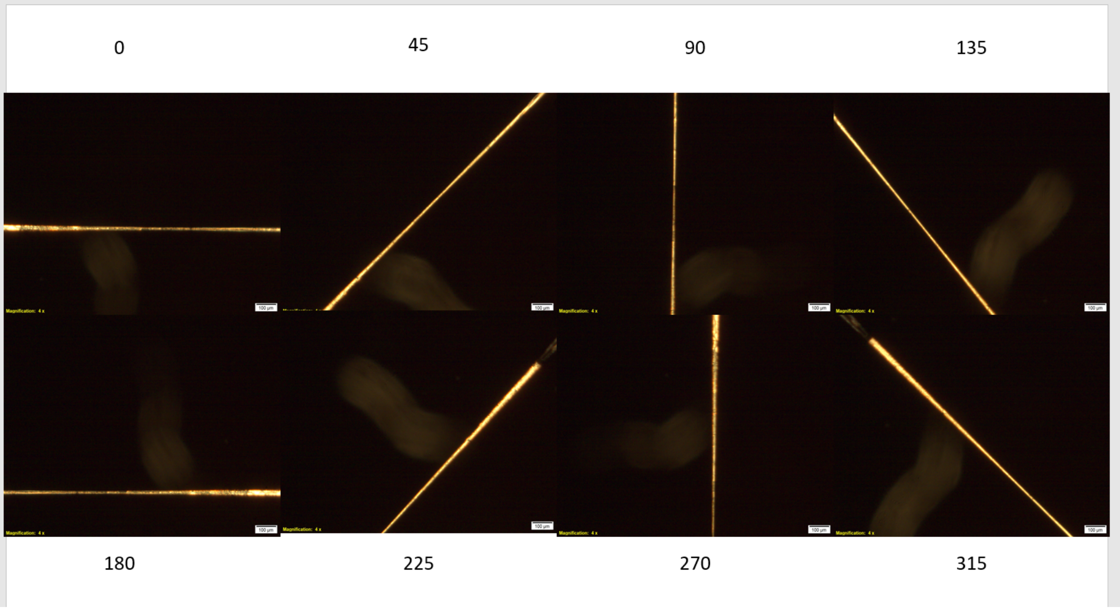

(a) Images taken under cross polarisation of a microchannel filled with LC at different angles under 4× objective.

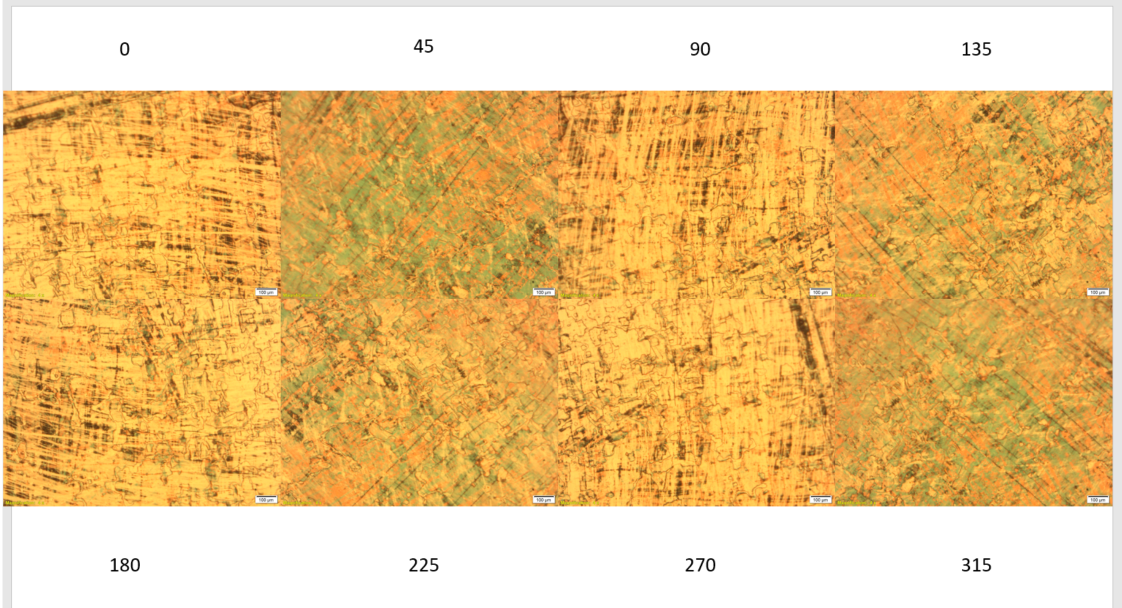

(b) Images taken under cross polarisation of a microchannel filled with LC at different angles under 50× objective.

Figure 9.1

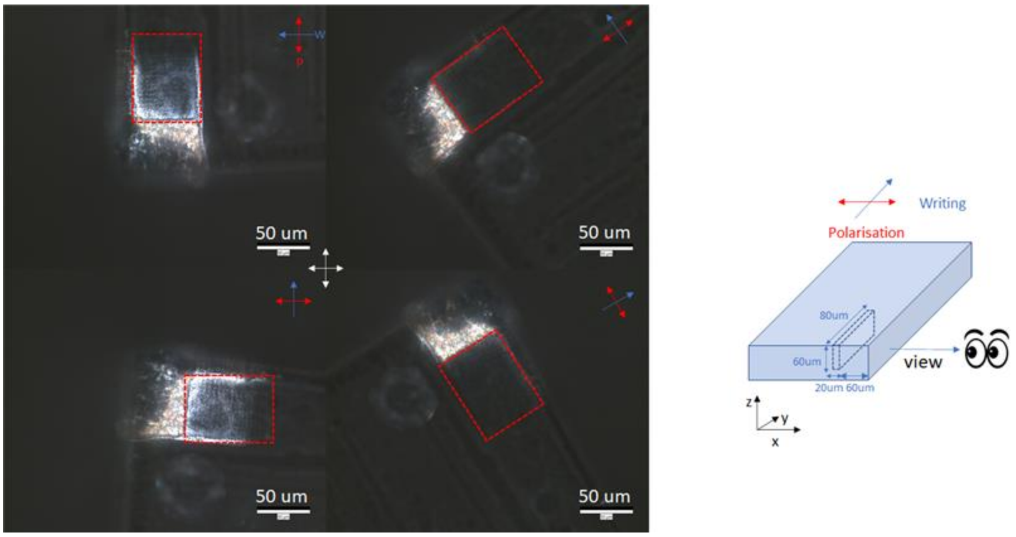

(a) Image of a microcell under crossed polarisation under microscope of 4× objective. The laser writing direction is perpendicular to the laser polarisation direction.

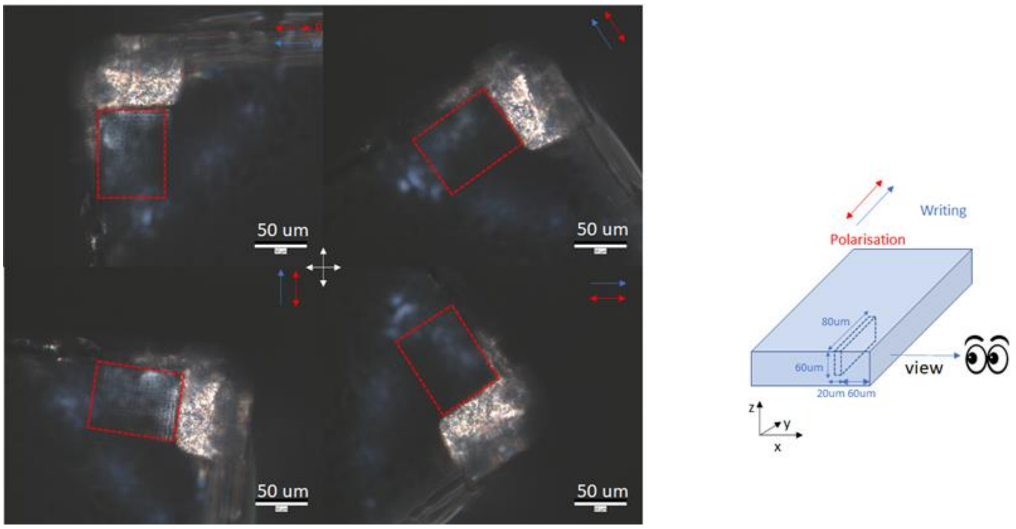

(b) Image of a microcell under crossed polarisation under microscope of 4× objective. The laser writing direction is parallel to the laser polarisation direction

Figure 9.2

the polarisation is constructive to the writing direction. While that for the other case shows worse alignment. These results have shown the potential for creating LC alignment surfaces within microchannels. However, the quality of LC alignment caused by laser fabrication is limited by the beam size. Which means that due to the diffraction limit, under diffraction limitation the separation between two adjacent tracks has to be larger than 1 μm. For a optimum design of the fibre devices this would be further improved.

References

[1] Stephen J Mihailov. “Fiber Bragg grating sensors for harsh environments”. In: *Sensors* 12.2 (2012), pp. 1898–1918.

[2] Joan R Casas and Paulo J S Cruz. “Fiber optic sensors for bridge monitoring”. In: *Journal of bridge engineering* 8.6 (2003), pp. 362–373.

[3] Roya Nazempour et al. “Emerging applications of optical fiber-based devices for brain research”. In: *Advanced Fiber Materials* (2022), pp. 1–19.

[4] Raffaella Di Sante. “Fibre optic sensors for structural health monitoring of aircraft composite structures: Recent advances and applications”. In: *Sensors* 15.8 (2015), pp. 18666–18713.

[5] George A Brown and Arthur Hartog. “Optical fiber sensors in upstream oil & gas”. In: *Journal of petroleum technology* 54.11 (2002), pp. 63–65.

[6] Rui Min et al. “Optical fiber sensing for marine environment and marine structural health monitoring: A review”. In: *Optics & Laser Technology* 140 (2021), p. 107082.

[7] Qingxu Yu and Xinlei Zhou. “Pressure sensor based on the fiber-optic extrinsic Fabry-Perot interferometer”. In: *Photonic Sensors* 1 (2011), pp. 72–83.

[8] Brian Culshaw. “Optical fiber sensor technologies: opportunities and-perhaps-pitfalls”. In: *Journal of lightwave technology* 22.1 (2004), p. 39.

[9] Arthur H Hartog. *An introduction to distributed optical fibre sensors.* CRC press, 2017.

[10] Xiaoyi Bao and Liang Chen. “Recent progress in distributed fiber optic sensors”. In: *sensors* 12.7 (2012), pp. 8601–8639.

[11] Mohammed Nasser Alahbabi, Y T Cho, and T P Newson. “Simultaneous temperature and strain measurement with combined spontaneous Raman and Brillouin scattering”. In: *Optics letters* 30.11 (2005), pp. 1276–1278.

[12] Andrzej W Domanski, Tomasz R Wolinski, and Wojtek J Bock. “Polarimetric fiber optic sensors: State of the art and future”. In: *Interferometry’94: Interferometric Fiber Sensing* 2341 (1994), pp. 21–28.

[13] Ralph C Jorgenson and Sinclair S Yee. “A fiber-optic chemical sensor based on surface plasmon resonance”. In: *Sensors and Actuators B: Chemical* 12.3 (1993), pp. 213–220.

[14] Mark Froggatt and Jason Moore. “High-spatial-resolution distributed strain measurement in optical fiber with Rayleigh scatter”. In: *Applied optics* 37.10 (1998), pp. 1735–1740.

[15] Kenneth O Hill and Gerald Meltz. “Fiber Bragg Grating Technology Fundamentals and Overview”. In: *JOURNAL OF LIGHTWAVE TECHNOLOGY* 15.8 (1997), p. 1263.

[16] Alan D Kersey et al. “Fiber grating sensors”. In: *Journal of lightwave technology* 15.8 (1997), pp. 1442–1463.

[17] Mousumi Majumder et al. “Fibre Bragg gratings in structural health monitoring—Present status and applications”. In: *Sensors and Actuators A: Physical* 147.1 (2008), pp. 150–164.

[18] Alberto Fernandez Fernandez et al. “Temperature monitoring of nuclear reactor cores with multiplexed fiber Bragg grating sensors”. In: *Optical Engineering* 41.6 (2002), pp. 1246–1254.

[19] Qiang Wang et al. “Dynamic strain measurement of hydraulic system pipeline using fibre Bragg grating sensors”. In: *Advances in Mechanical Engineering* 8.4 (2016), p. 1687814016645069.

[20] Shaohua Tian et al. “Damage detection based on static strain responses using FBG in a wind turbine blade”. In: *Sensors* 15.8 (2015), pp. 19992–20005.

[21] Daniela Lo Presti et al. “Fiber bragg gratings for medical applications and future challenges: A review”. In: *Ieee Access* 8 (2020), pp. 156863–156888.

[22] Alfredo Lamberti et al. “Dynamic strain measurements on automotive and aeronautic composite components by means of embedded fiber Bragg grating sensors”. In: *Sensors* 15.10 (2015), pp. 27174–27200.

[23] Ian C M Littler, Martin Rochette, and Benjamin J Eggleton. “Adjustable bandwidth dispersionless bandpass FBG optical filter”. In: *Optics Express* 13.9 (2005), pp. 3397–3407.

[24] Wardeh Saleh Al-Younis and Mohammed Hussein Bataineh. “Pulse compression using Fiber Bragg gratings”. In: *2017 4th International Conference on Electrical and Electronic Engineering (ICEEE)*. IEEE, 2017, pp. 240–245.

[25] A Yu Tkachenko et al. “Fibre loop mirror with FBGs for the scanning range stabilisation in a fibre self-sweeping laser”. In: *Quantum Electronics* 48.12 (2018), p. 1132.

[26] K O Hill et al. “Photosensitivity in optical fiber waveguides: Application to reflection filter fabrication”. In: *Applied physics letters* 32.10 (1978), pp. 647–649.

[27] Yonglin Huang et al. “Temperature compensation package for fiber Bragg gratings”. In: *Microwave and Optical Technology Letters* 39.1 (2003), pp. 70–72.

[28] M G Xu et al. “Discrimination between strain and temperature effects using dual-wavelength fibre grating sensors”. In: *Electronics letters* 30.13 (1994), pp. 1085–1087.

[29] Guanghui Chen et al. “Simultaneous strain and temperature measurements with fiber Bragg grating written in novel Hi-Bi optical fiber”. In: *IEEE Photonics Technology Letters* 16.1 (2004), pp. 221–223.

[30] A K Singh et al. “Simultaneous strain and temperature measurement using a single fiber Bragg grating embedded in a composite laminate”. In: *Smart Materials and Structures* 26.11 (2017), p. 115025.

[31] O Frazao et al. “Discrimination of strain and temperature using Bragg gratings in microstructured and standard optical fibres”. In: *Measurement Science and Technology* 16.10 (2005), p. 2109.

[32] Da-Peng Zhou et al. “Simultaneous measurement for strain and temperature using fiber Bragg gratings and multimode fibers”. In: *Applied optics* 47.10 (2008), pp. 1668–1672.

[33] Chiranjit Ghosh and Vishnu Priye. “Temperature compensated high-resolution interrogation of FBG strain sensor based on four wave mixing”. In: *IEEE Sensors Journal* 20.23 (2020), pp. 14181–14186.

[34] Wei-Chong Du, Xiao-Ming Tao, and Hwa-Yaw Tam. “Fiber Bragg grating cavity sensor for simultaneous measurement of strain and temperature”. In: *IEEE Photonics Technology Letters* 11.1 (1999), pp. 105–107.

[35] H J Patrick et al. “Hybrid fiber Bragg grating/long period fiber grating sensor for strain/temperature discrimination”. In: *IEEE Photonics Technology Letters* 8.9 (1996), pp. 1223–1225.

[36] Xuekai Gao et al. “A dual-parameter fiber sensor based on few-mode fiber and fiber Bragg grating for strain and temperature sensing”. In: *Optics Communications* 454 (2020), p. 124441.

[37] Chao Li et al. “Strain and temperature discrimination using a fiber Bragg grating and multimode interference effects”. In: *Optics Communications* 343 (2015), pp. 6–9.

[38] Jaehoon Jung et al. “Simultaneous measurement of strain and temperature by use of a single-fiber Bragg grating and an erbium-doped fiber amplifier”. In: *Applied Optics* 38.13 (1999), pp. 2749–2751.

[39] Sotiris E Kanellopoulos, Vincent A Handerek, and Alan J Rogers. “Simultaneous strain and temperature sensing with photogenerated in-fiber gratings”. In: *Optics Letters* 20.3 (1995), pp. 333–335.

[40] Sanjib Sarkar et al. “Discrimination between strain and temperature effects of a single fiber Bragg grating sensor using sidelobe power”. In: *Journal of Applied Physics* 127.11 (2020), p. 114503.

[41] Sanjib Sarkar et al. “Machine learning methods for discriminating strain and temperature effects on FBG-based sensors”. In: *IEEE Photonics Technology Letters* 33.16 (2021), pp. 876–879.

[42] S W James, M L Dockney, and R P Tatam. “Simultaneous independent temperature and strain measurement using in-fibre Bragg grating sensors”. In: *Electronics Letters* 32.12 (1996), pp. 1133–1134.

[43] Xiaohong Li et al. “Simultaneous independent temperature and strain measurement using one fiber Bragg grating based on the etching technique”. In: *Microwave and optical technology letters* 43.6 (2004), pp. 478–481.

[44] Hugo F Lima et al. “Simultaneous measurement of strain and temperature with a single fiber Bragg grating written in a tapered optical fiber”. In: *IEEE Sensors Journal* 10.2 (2009), pp. 269–273.

[45] Vivekanand Mishra, Mukesh Lohar, and Angela Amphawan. “Improvement in temperature sensitivity of FBG by coating of different materials”. In: *Optik* 127.2 (2016), pp. 825–828.

[46] Khurram Naeem and Youngjoo Chung. “Strain and temperature discrimination using PCF Bragg-gratings filled with different liquids”. In: *2014 OECC and Australian Conference on Optical Fibre Technology.* IEEE, 2014, pp. 795–796.

[47] Minh Châu Phan Huy et al. “Passive temperature-compensating technique for microstructured fiber Bragg gratings”. In: *IEEE Sensors Journal* 8.7 (2008), pp. 1073–1078.

[48] Wei Cheng et al. “Femtosecond-laser-inscribed Bragg grating in hollow-core fiber for highly sensitive optofluidic sensing”. In: *Optics Letters* 48.15 (2023), pp. 3941–3944.

[49] Nicolas Mothe et al. “Thermal wavelength stabilization of Bragg gratings photowritten in hole-filled microstructured optical fibers”. In: *Optics Express* 16.23 (2008), pp. 19018–19033.

[50] Wenqing Man et al. “Optimization design of temperature-insensitive Bragg gratings inscribed in ethanol-filled photonic crystal fibers”. In: *Optical Engineering* 58.11 (2019), p. 116101.

[51] Wenqing Man, Jinpeng Feng, and Jun Peng. “Optimization design of high-sensitivity temperature sensor based on Bragg grating in liquid-filled photonic crystal fibers”. In: *Optical Engineering* 51.8 (2012), p. 85004.

[52] Max Born and Emil Wolf. *Principles of optics: electromagnetic theory of propagation, interference and diffraction of light.* Elsevier, 2013.

[53] Frederique De Fornel. *Evanescent waves: from Newtonian optics to atomic optics.* Vol. 73. Springer Science & Business Media, 2001.

[54] Allan W Snyder. “Leaky-ray theory of optical waveguides of circular cross section”. In: *Applied physics* 4.4 (1974), pp. 273–298.

[55] K Charles Kao and George A Hockham. “Dielectric-fibre surface waveguides for optical frequencies”. In: *Proceedings of the Institution of Electrical Engineers.* Vol. 113. 7. IET, 1966, pp. 1151–1158.

[56] P L Francois et al. “Equivalent step-index profile for graded W-fibres: application to TE01 mode cut-off”. In: *Optical and Quantum Electronics* 14 (1982), pp. 483–499.

[57] Eli Yablonovitch. “Inhibited spontaneous emission in solid-state physics and electronics”. In: *Physical review letters* 58.20 (1987), p. 2059.

[58] Sajeev John. “Strong localization of photons in certain disordered dielectric superlattices”. In: *Physical review letters* 58.23 (1987), p. 2486.

[59] Philip St J Russell. “Photonic-crystal fibers”. In: *Journal of lightwave technology* 24.12 (2006), pp. 4729–4749.

[60] William W Morey, Gerald Meltz, and William H Glenn. “Fiber optic Bragg grating sensors”. In: *Fiber optic and laser sensors VII.* Vol. 1169. International Society for Optics and Photonics, 1990, pp. 98–107.

[61] Mohammad Moghimi, Hassan Ghafoori-Fard, and Ali Rostami. “Analysis and design of all-optical switching in apodized and chirped Bragg gratings”. In: *Progress In Electromagnetics Research B* 8 (2008), pp. 87–102.

[62] Julian A Fells and Richard Epworth. “Chirped Bragg grating reflectors and adjustable dispersion apparatus incorporating such gratings”. In: *U.S. Patent No. 6,519,390* (Feb. 2003).

[63] Siddharth Ramachandran et al. “Fiber-based tunable dispersion compensation”. In: *Fiber Based Dispersion Compensation* (2007), pp. 379–423.

[64] Jacques Albert, Li-Yang Shao, and Christophe Caucheteur. “Tilted fiber Bragg grating sensors”. In: *Laser & Photonics Reviews* 7.1 (2013), pp. 83–108.

[65] C Caucheteur et al. “Simultaneous bend and temperature sensor using tilted FBG”. In: *17th International Conference on Optical Fibre Sensors*. Vol. 5855. SPIE, 2005, pp. 707–710.

[66] Bao-Jin Peng et al. “Tilt sensor with FBG technology and matched FBG demodulating method”. In: *IEEE Sensors Journal* 6.1 (2006), pp. 63–66.

[67] Ming Li et al. “Continuously tunable photonic fractional temporal differentiator based on a tilted fiber Bragg grating”. In: *IEEE Photonics Technology Letters* 23.4 (2010), pp. 251–253.

[68] C C Ye, S W James, and R P Tatam. “Simultaneous temperature and bend sensing with long-period fiber gratings”. In: *Optics Letters* 25.14 (2000), pp. 1007–1009.

[69] Vikram Bhatia. “Applications of long-period gratings to single and multi-parameter sensing”. In: *Optics express* 4.11 (1999), pp. 457–466.

[70] Ashish M Vengsarkar et al. “Long-period fiber gratings as band-rejection filters”. In: *Journal of lightwave technology* 14.1 (1996), pp. 58–65.

[71] Ams Martinez et al. “Direct writing of fibre Bragg gratings by femtosecond laser”. In: *Electronics letters* 40.19 (2004), pp. 1170–1172.

[72] J Canning and M G Sceats. “Pi-phase-shifted periodic distributed structures in optical fibres by UV post-processing”. In: *Electronics Letters* 30.16 (1994), pp. 1344–1345.

[73] Hartmut Bartelt et al. “Single-pulse fiber Bragg gratings and specific coatings for use at elevated temperatures”. In: *Applied Optics* 46.17 (2007), pp. 3417–3424.

[74] Kaiming Zhou et al. “Line-by-line fiber Bragg grating made by femtosecond laser”. In: *IEEE Photonics Technology Letters* 22.16 (2010), pp. 1190–1192.

[75] Bai-Ou Guan et al. “Simultaneous strain and temperature measurement using a superstructure fiber Bragg grating”. In: *IEEE Photonics Technology Letters* 12.6 (2000), pp. 675–677.

[76] Yun Jiang Rao et al. “Combined spatial-and time-division-multiplexing scheme for fiber grating sensors with drift-compensated phase-sensitive detection”. In: *Optics letters* 20.20 (1995), pp. 2149–2151.

[77] Minho Song et al. “Simultaneous measurement of temperature and strain using two fiber Bragg gratings embedded in a glass tube”. In: *Optical Fiber Technology* 3.2 (1997), pp. 194–196.

[78] Allan W Snyder and John Love. *Optical waveguide theory.* Springer Science & Business Media, 1983.

[79] Julius Adams Stratton. *Electromagnetic theory.* Vol. 33. John Wiley & Sons, 2007.

[80] R B Adler. “Waves on inhomogeneous cylindrical structures”. In: *Proceedings of the IRE* 40.3 (1952), pp. 339–348.

[81] Leonard G Cohen, Dietrich Marcuse, and Wanda L Mammel. “Radiating leaky-mode losses in single-mode lightguides with depressed-index claddings”. In: *IEEE Transactions on Microwave Theory and Techniques* 30.10 (1982), pp. 1455–1460.

[82] S Kawakami and Shingeo Nishida. “Characteristics of a doubly clad optical fiber with a low-index inner cladding”. In: *IEEE Journal of Quantum Electronics* 10.12 (1974), pp. 879–887.

[83] Allan W Snyder and William R Young. “Modes of optical waveguides”. In: *JOSA* 68.3 (1978), pp. 297–309.

[84] F.T. AreccHI and R. Bonifacio. “Theory of Optical Maser Amplifiers”. In: *IEEE Journal of Quantum Electronics* (1965), pp. 169–178.

[85] I Bennion et al. “UV-written in-fibre Bragg gratings”. In: *Optical and Quantum Electronics* 28.2 (1996), pp. 93–135.

[86] Amnon. Yariv. *Optical electronics.* Saunders College Pub, 1991, p. 713.

[87] Philip L. Mason. “Fibre Bragg gratings and their applications”. PhD thesis. University of Bath, 1996.

[88] *fimmprop.*

[89] Valeria Maselli et al. “Femtosecond laser written optofluidic sensor: Bragg grating waveguide evanescent probing of microfluidic channel”. In: *Optics Express* 17.14 (2009), pp. 11719–11729.

[90] Jörg Rheims, Jan Köser, and Thomas Wriedt. “Refractive-index measurements in the near-IR using an Abbe refractometer”. In: *Measurement Science and Technology* 8.6 (1997), p. 601.

[91] Konstantinos Moutzouris et al. “Refractive, dispersive and thermo-optic properties of twelve organic solvents in the visible and near-infrared”. In: *Applied Physics B* 116 (2014), pp. 617–622.

[92] Nikolaos J Florous et al. “Thermooptical sensitivity analysis of highly birefringent polarimetric sensing photonic crystal fibers with elliptically elongated veins”. In: *IEEE photonics technology letters* 18.15 (2006), pp. 1663–1665.

[93] Koichi Takamura, Herbert Fischer, and Norman R Morrow. “Physical properties of aqueous glycerol solutions”. In: *Journal of Petroleum Science and Engineering* 98 (2012), pp. 50–60.

[94] Bogumil Zelent, Nathaniel V Nucci, and Jane M Vanderkooi. “Liquid and ice water and glycerol/water glasses compared by infrared spectroscopy from 295 to 12 K”. In: *The Journal of Physical Chemistry A* 108.50 (2004), pp. 11141–11150.

[95] Kwang Taek Kim et al. “A temperature-insensitive cladding-etched fiber Bragg grating using a liquid mixture with a negative thermo-optic coefficient”. In: *Sensors* 12.6 (2012), pp. 7886–7892.

[96] Cargille labs. *Refractive-Index-Liquid-Series-AA-n-1.4400-at-589.3-nm-and-25° C.* 2018. URL: `https://www.cargille.com/refractive-index-liquids`.

[97] Corning. *Corning ® SMF-28e+ ® Photonic Optical Fiber.* Tech. rep. 2010.

[98] Qiang Wu et al. "A comprehensive analysis verified by experiment of a refractometer based on an SMF28–small-core singlemode fiber (SCSMF)–SMF28 fiber structure". In: *Journal of Optics* 13.12 (2011), p. 125401.

[99] H M MacDonald. "The Addition-Theorem for the Bessel Functions". In: *Proceedings of the London Mathematical Society* 1.1 (1900), pp. 152–157.

[100] K Miura Davis et al. "Writing waveguides in glass with a femtosecond laser". In: *Optics letters* 21.21 (1996), pp. 1729–1731.

[101] Yasuhiko Shimotsuma et al. "Self-organized nanogratings in glass irradiated by ultrashort light pulses". In: *Physical review letters* 91.24 (2003), p. 247405.

[102] E N Glezer et al. "Three-dimensional optical storage inside transparent materials". In: *Optics letters* 21.24 (1996), pp. 2023–2025.

[103] Calum A Ross et al. "Optimisation of ultrafast laser assisted etching in fused silica". In: *Optics express* 26.19 (2018), pp. 24343–24356.

[104] Jia Qi et al. "Femtosecond laser induced selective etching in fused silica: optimization of the inscription conditions with a high-repetition-rate laser source". In: *Optics Express* 26.23 (Nov. 2018), p. 29669.

[105] Stefan Nolte et al. "Femtosecond waveguide writing: a new avenue to three-dimensional integrated optics". In: *Applied Physics A* 77.1 (2003), pp. 109–111.

[106] Bin-Bin Xu et al. "Fabrication and multifunction integration of microfluidic chips by femtosecond laser direct writing". In: *Lab on a Chip* 13.9 (2013), pp. 1677–1690.

[107] Chris B Schaffer, Andre Brodeur, and Eric Mazur. "Laser-induced breakdown and damage in bulk transparent materials induced by tightly focused femtosecond laser pulses". In: *Measurement Science and Technology* 12.11 (2001), p. 1784.

[108] Joseph Berkowitz. *Photoabsorption, photoionization, and photoelectron spectroscopy.* Academic Press, 2012.

[109] Roberto Osellame, Giulio Cerullo, and Roberta Ramponi. *Femtosecond laser micromachining: photonic and microfluidic devices in transparent materials.* Vol. 123. Springer Science & Business Media, 2012.

[110] Calum Alexander Ross. "Ultrafast laser assisted etching of fibre optic probes for optical biopsy instruments". PhD thesis. Heriot-Watt University, 2019.

[111] Lionel Sudrie et al. "Femtosecond laser-induced damage and filamentary propagation in fused silica". In: *Physical Review Letters* 89.18 (2002), p. 186601.

[112] Scott C Jones et al. "Recent progress on laser-induced modifications and intrinsic bulk damage of wide-gap optical materials". In: *Optical Engineering* 28.10 (1989), p. 281039.

[113] L V Keldysh. "Ionization in the field of a strong electromagnetic wave". In: *Sov. Phys. JETP* 20.5 (1965), pp. 1307–1314.

[114] Shingo Kanehira, Kiyotaka Miura, and Kazuyuki Hirao. “Ion exchange in glass using femtosecond laser irradiation”. In: *Applied Physics Letters* 93.2 (2008), p. 023112.

[115] Rafael R Gattass and Eric Mazur. “Femtosecond laser micromachining in transparent materials”. In: *Nature photonics* 2.4 (2008), pp. 219–225.

[116] Kazuyoshi Itoh et al. “Ultrafast processes for bulk modification of transparent materials”. In: *MRS bulletin* 31.8 (2006), pp. 620–625.

[117] Andrius Marcinkevičius et al. “Femtosecond laser-assisted three-dimensional microfabrication in silica”. In: *Optics Letters* 26.5 (2001), pp. 277–279.

[118] Saulius Juodkazis et al. “Laser-induced microexplosion confined in the bulk of a sapphire crystal: evidence of multimegabar pressures”. In: *Physical review letters* 96.16 (2006), p. 166101.

[119] T Hoshino and Y Nishioka. “Etching process of SiO 2 by HF molecules”. In: *The Journal of chemical physics* 111.5 (1999), pp. 2109–2114.

[120] D Martin Knotter. “Etching mechanism of vitreous silicon dioxide in HF-based solutions”. In: *Journal of the American Chemical Society* 122.18 (2000), pp. 4345–4351.

[121] Yves Bellouard et al. “Scanning thermal microscopy and Raman analysis of bulk fused silica exposed to low-energy femtosecond laser pulses”. In: *Optics Express* 16.24 (2008), pp. 19520–19534.

[122] Charles M Pépin et al. “Silicon formation in bulk silica through femtosecond laser engraving”. In: *arXiv preprint arXiv:1806.10802* (2018).

[123] H Camon and Z Moktadir. “Simulation of silicon etching with KOH”. In: *Microelectronics journal* 28.4 (1997), pp. 509–517.

[124] H Seidel et al. “Anisotropic etching of crystalline silicon in alkaline solutions: II. Influence of dopants”. In: *Journal of the Electrochemical Society* 137.11 (1990), p. 3626.

[125] C Hnatovsky et al. “Polarization-selective etching in femtosecond laser-assisted microfluidic channel fabrication in fused silica”. In: *OPTICS LETTERS* 230.14 (2005), p. 1867.

[126] Jens Gottmann et al. “Selective laser-induced etching of 3D precision quartz glass components for microfluidic applications—up-scaling of complexity and speed”. In: *Micromachines* 8.4 (2017), p. 110.

[127] Chris B Schaffer et al. “Micromachining bulk glass by use of femtosecond laser pulses with nanojoule energy”. In: *Optics letters* 26.2 (2001), pp. 93–95.

[128] Martin Hermans, Jens Gottmann, and Frank Riedel. “Selective, Laser-Induced Etching of Fused Silica at High Scan-Speeds Using KOH.” In: *Journal of Laser Micro/Nanoengineering* 9.2 (2014).

[129] Bangshan Sun, Patrick S Salter, and Martin J Booth. “Pulse front adaptive optics: a new method for control of ultrashort laser pulses”. In: *Optics express* 23.15 (2015), pp. 19348–19357.

[130] Y Lai et al. “Point-by-point inscription of first-order fiber Bragg grating for C-band applications”. In: *Optics express* 15.26 (2007), pp. 18318–18325.

[131] Robert J Williams et al. “Femtosecond direct-writing of low-loss fiber Bragg gratings using a continuous core-scanning technique”. In: *Optics letters* 38.11 (2013), pp. 1918–1920.

[132] Erden Ertorer et al. “Femtosecond laser filaments for rapid and flexible writing of fiber Bragg grating”. In: *Optics Express* 26.7 (2018), pp. 9323–9331.

[133] Graham D Marshall et al. “Point-by-point written fiber-Bragg gratings and their application in complex grating designs”. In: *Optics express* 18.19 (2010), pp. 19844–19859.

[134] Yijing Chen, Yicheng Lai, and Marcus Weng Onn Cheong. “Distortion-free femtosecond laser inscription in free-standing optical fiber”. In: *Applied Optics* 55.21 (2016), pp. 5575–5579.

[135] Ya Cheng et al. “Control of the cross-sectional shape of a hollow microchannel embedded in photostructurable glass by use of a femtosecond laser”. In: *Optics letters* 28.1 (2003), pp. 55–57.

[136] Martin Ams et al. “Slit beam shaping method for femtosecond laser direct-write fabrication of symmetric waveguides in bulk glasses”. In: *Optics express* 13.15 (2005), pp. 5676–5681.

[137] B Malo et al. “Point-by-point fabrication of micro-Bragg gratings in photosensitive fibre using single excimer pulse refractive index modification techniques”. In: *Electronics Letters* 18.29 (1993), pp. 1668–1669.

[138] Patrick S Salter et al. “Femtosecond fiber Bragg grating fabrication with adaptive optics aberration compensation”. In: *Optics letters* 43.24 (2018), pp. 5993–5996.

[139] Hongzhi Jia and Yulin Li. “First-and second-order diffraction characteristics of fiber Bragg gratings”. In: *Optics communications* 178.4-6 (2000), pp. 339–343.

[140] Mutlu Özcan, Arezo Allahbeickaraghi, and Mine Dündar. “Possible hazardous effects of hydrofluoric acid and recommendations for treatment approach: a review”. In: *Clinical oral investigations* 16 (2012), pp. 15–23.

[141] Nathaniel Groothoff et al. “Transition and self-healing process between chaotic and self-organized patterns observed during femtosecond laser writing”. In: *Optics Express* 23.13 (2015), pp. 16993–17007.

[142] Ayokunle Olanrewaju et al. “Capillary microfluidics in microchannels: from microfluidic networks to capillaric circuits”. In: *Lab on a Chip* 18.16 (2018), pp. 2323–2347.

[143] Jan C T Eijkel and Albert Van Den Berg. “Young 4ever-the use of capillarity for passive flow handling in lab on a chip devices”. In: *Lab on a Chip* 6.2/11 (2006), pp. 1405–1408.

[144] Hamdi Orun, Mircea V Udrea, and Ali Alacakir. “Polishing of optical fibers using a CO2 laser”. In: *SIOEL’99: Sixth Symposium on Optoelectronics*. Vol. 4068. SPIE, 2000, pp. 570–575.

[145] M Ratuszek et al. “Process optimisation of the arc fusion splicing different types of single mode telecommunication fibers”. In: *Optoelectronics Review* 2 (2000), pp. 161–170.

[146] Krzysztof Borzycki and Kay Schuster. *Arc fusion splicing of photonic crystal fibres*. InTech, 2012.

[147] Zipei Song et al. “Fiber Bragg grating sensors with ultrahigh or ultralow temperature sensitivity”. In: *Optical Fiber Sensors*. Optica Publishing Group, 2023, pp. 2–2.

[148] L F Hoyt. “New table of the refractive index of pure glycerol at 20 C”. In: *Industrial & Engineering Chemistry* 26.3 (1934), pp. 329–332.

[149] Mohan Wang et al. “Single-mode sapphire fiber Bragg grating”. In: *Optics Express* 30.9 (2022), pp. 15482–15494.

[150] S H Lee and Anthony M Waas. “Compressive response and failure of fiber reinforced unidirectional composites”. In: *International Journal of Fracture* 100 (1999), pp. 275–306.

[151] D Sengupta et al. “An improved low temperature sensing using PMMA coated FBG”. In: *Asia Communications and Photonics Conference and Exhibition*. Optica Publishing Group, 2011, p. 831103.

[152] V V Ravi Kanth Kumar et al. “Extruded soft glass photonic crystal fiber for ultrabroad supercontinuum generation”. In: *Optics Express* 10.25 (2002), pp. 1520–1525.

[153] Hicham El Hamzaoui et al. “From molecular precursors in solution to microstructured optical fiber: a Sol-gel polymeric route”. In: *Optical Materials Express* 1.2 (2011), pp. 234–242.

[154] Desmond M Chow, S R Sandoghchi, and F R Mahamd Adikan. “Fabrication of photonic crystal fibers”. In: *2012 Ieee 3rd international conference on photonics*. IEEE, 2012, pp. 227–230.

[155] J C Knight et al. “All-silica single-mode optical fiber with photonic crystal cladding”. In: *Optics letters* 21.19 (1996), pp. 1547–1549.

[156] Sarik R Nersisyan et al. “Study of azo dye surface command photoalignment material for photonics applications”. In: *Applied optics* 49.10 (2010), pp. 1720–1727.

[157] A Marino. “Optical studies of liquid crystals”. In: *Nuovo Cimento C Geophysics Space Physics C* 39.2 (2016), p. 278.

[158] Shoichi Ishihara et al. “The effect of rubbed polymer films on the liquid crystal alignment”. In: *Liquid Crystals* 4.6 (1989), pp. 669–675.

[159] Kunihiro Ichimura. “Photoalignment of liquid-crystal systems”. In: *Chemical reviews* 100.5 (2000), pp. 1847–1874.

[160] David J Alt et al. “Oscillatory shear alignment of a liquid crystalline polymer”. In: *Macromolecules* 28.5 (1995), pp. 1575–1579.

[161] Jai Prakash, Akash Kumar, and Shikha Chauhan. “Aligning liquid crystal materials through nanoparticles: A review of recent progress”. In: *Liquids* 2.2 (2022), pp. 50–71.

[162] Bing Sun et al. “Unique temperature dependence of selectively liquid-crystal-filled photonic crystal fibers”. In: *IEEE Photonics Technology Letters* 28.12 (2016), pp. 1282–1285.

[163] Ying Guo et al. "Amphibious sensor of temperature and refractive index based on D-shaped photonic crystal fibre filled with liquid crystal". In: *Liquid Crystals* 47.6 (2020), pp. 882–894.

[164] Abdullah Rahnama et al. "In-Fiber Switchable Polarization Filter Based on Liquid Crystal Filled Hollow-Filament Bragg Gratings". In: *Advanced Optical Materials* (2021), p. 2100054.

[165] Sławomir Ertman et al. "Patterned alignment of liquid crystal molecules in silica micro-capillaries". In: *Liquid Crystals* 40.1 (2013), pp. 1–6.

[166] A Solodar et al. "Ultrafast laser induced nanostructured ITO for liquid crystal alignment and higher transparency electrodes". In: *Applied Physics Letters* 113.8 (2018).

[167] Yang Liao et al. "Alignment of liquid crystal molecules in a micro-cell fabricated by femtosecond laser". In: *Chemical Physics Letters* 498.1-3 (2010), pp. 188–191.